X-ray Absorption Spectra of Kesterite-based Materials Studied from First Principles

Dissertation

zur Erlangung des akademischen Grades

doctor rerum naturalium (Dr. rer. nat.)

im Fach: Physik

Spezialisierung: Theoretische Physik

eingereicht an der

Mathematisch-Naturwissenschaftlichen Fakultät

der Humboldt-Universität zu Berlin

von

M.Sc. Archana Manoharan

Präsidentin der Humboldt-Universität zu Berlin

Prof. Dr. Sabine Kunst

Dekan der Mathematisch-Naturwissenschaftlichen Fakultät

Prof. Dr. Elmar Kulke

Gutachter/innen:	1.	Prof. Dr. Dr. hc Claudia Draxl
	2.	Prof. Dr. Clas Persson
	3.	Prof. Dr. John J. Rehr
Tag der mündlichen Prüfung:		18.11.2021

Ich erkläre, dass ich die Dissertation selbständig und nur unter Verwendung der von mir gemäß §7 Abs. 3 der Promotionsordnung der Mathematisch-Naturwissenschaftlichen Fakultät, veröffentlicht im Amtlichen Mitteilungsblatt der Humboldt-Universität zu Berlin Nr. 42/2018 am 11.07.2018 angegebenen Hilfsmittel angefertigt habe.

Berlin, den 18. *November* 2021

X-ray Absorption Spectra of Kesterite-based Materials Studied from First Principles

Ph.D. Thesis

Archana Manoharan

Supervisor: Prof. Dr. Claudia Draxl

To

My Mom

Summary

Solar energy is a reliable energy source to meet the fast-growing energy demand of today's world. An absorber layer is the core of the solar cell device which absorbs sunlight and transports the resulting charge carriers to the electrical contacts. The kesterite Cu_2ZnSnS_4 (CZTS) is a promising candidate which consists of earth abundant and non-toxic elements. CZTS has attracted much interest due to its high absorption coefficient of about $\sim 1 \times 10^{-4}\text{cm}^{-1}$ and optimal bandgap of 1.4 eV. It is challenging to however, understand the electronic properties of this complex quaternary structure.

The aim of this work is to understand the electronic properties of CZTS. X-ray absorption near edge structure (XANES) is a powerful tool for this purpose. Interpreting XANES of complex materials is nontrivial and thus requires theoretical modeling. Here, all the calculations are performed using an all-electron full-potential augmented plane-wave method as implemented in the `exciting` code. The accurate description of the core level excitations are performed by a two-step procedure. First, the electronic structure is calculated by solving the Kohn-Sham (KS) equation of density-functional theory (DFT). The absorption spectra including elecron-hole (*e-h*) is described by the solution of the Bethe-Salpeter equation (BSE) of many-body perturbation theory (MBPT) using the KS states as starting point.

Hereby, the excitations from the sulfur 1*s* and 2*p* core states in CZTS and their related by-products like secondary phases (ZnS and SnS_2) and defect complexes (V_{Cu}+Zn_{Cu} and Cu_{Zn}+Zn_{Cu}) are studied. First, the spectral signatures of the single-phase CZTS are obtained. The character of the individual atomic contributions is studied to analyze the obtained spectra. There were however, significant differences between the spectral features of pristine CZTS and experiments. In comparison with the absorption spectra of binary phases, it can be understood that the lowest spectral features of CZTS resemble SnS_2 and the features at higher energy resemble ZnS. The discrepancies between the calculated and measured spectra in CZTS however, remain an open question. For this purpose, we demonstrate the influence of defect complexes on the excited state properties of CZTS. First, the core level shifts upon the defect formation is understood as they are sensitive to chemical environment. The spectral signatures are obtained for the selected inequivalent sulfur sites. A detailed analysis of the impact of the local chemical environment is performed. From the insight gained from this analysis, the nature of the defects dominating the measured spectra are determined.

Zusammenfassung

Solarenergie ist eine verlässliche Energiequelle, die zur Deckung des schnell wachsenden Energiebedarfs der heutigen Welt beiträgt. Das Kernelement einer Solarzelle ist die Absorptionsschicht, welche das Licht absorbiert und die dabei entstehenden Ladungsträger zu den elektrischen Kontakten transportiert. Der Kesterit Cu_2ZnSnS_4 ist ein vielversprechender Kandidat, bestehend aus häufig auf der Erde vorkommenden, nicht toxischen Elementen. CZTS hat aufgrund seines hohen Absorptionskoeffizienten von rund $\sim 1 \times 10^{-4} \mathrm{cm}^{-1}$ und der optimalen Bandlücke von 1.4 eV viel Beachtung gefunden. Es ist indes eine Herausforderung, die elektronischen Eigenschaften von dieser komplexen quaternären Struktur zu verstehen.

Das Ziel dieser Arbeit ist, die elektronischen Eigenschaften von CZTS zu verstehen. Ein leistungsfähiges Werkzeug zu diesem Zweck ist die Röntgen-Nahkanten-Absorptions-Spektroskopie (XANES). Die Interpretation von XANES-Spektren komplexer Materialien ist nicht trivial und erfordert daher theoretische Modellierung. Alle Rechnungen in dieser Arbeit wurden mittels der im `exciting` Code implementierten Linearized-Augmented-Plane-Wave-Methode, welche alle Elektronen gleichberechtigt behandelt, durchgeführt. Die genaue Beschreibung der Anregungen von Kernzuständen wird durch ein zweistufiges Verfahren erreicht. Zunächst wird die elektronische Struktur berechnet, indem die Kohn-Sham-Gleichungen (KS) der Dichtefunktionaltheorie (DFT) gelöst werden. Die Absorptionsspektren unter Berücksichtigung der Elektron-Loch-Wechselwirkung (*e-h*) werden durch die Lösung der Bethe-Salpeter Gleichung (BSE) der Vielteilchen-Störungstheorie (MBPT) unter Einsatz der KS-Zustönde als Ausgangspunkt beschrieben.

Auf diese Weise werden die Anregungen der Schwefel 1*s* und 2*s* Kernzustände in CZTS und ihre verwandten Nebenprodukte wie Sekundärphasen (ZnS und SnS_2) sowie Defektkomplexe (V_{Cu}+Zn_{Cu} und Cu_{Zn}+ZnCu) untersucht. Zuerst werden die spektralen Signaturen des ungestörten CZTS berechnet. Um die erlangten Spektren zu analysieren, wird der Charakter der individuellen atomaren Beiträge untersucht. Es gibt jedoch erhebliche Unterschiede zwischen den Spektralmerkmalen des reinen CZTS und den experimentellen Ergebnissen. Der Vergleich mit den Absorptionsspektren der Binärphasen offenbart, dass die niedrigsten spektralen Charakteristika von CZTS denen von SnS_2 ähneln, wohingegen die Merkmale bei einer höheren Energie denen von ZnS ähneln. Die Frage nach der Herkunft der Abweichungen zwischen den berechneten und den gemessenen Spektren in CZTS bleibt dagegen offen. Zu diesem Zweck zeigen wir den Einfluss von Defektkomplexen auf die Eigenschaften des angeregten Zustands von

CZTS. Zunächst werden die Verschiebungen der Kernniveaus bei der Defektbildung untersucht, die empfindlich auf die chemische Umgebung reagieren. Die Anregungsspektren der symmetrisch inäquivalenten Schwefelatome werden berechnet und die Auswirkung der lokalen chemischen Umgebung wird im Detail untersucht. Aus den so gewonnenen Erkenntnissen können Rückschlüsse über die Art der Defekte gezogen werden, die gemessenen Spektren dominieren.

Contents

1 Introduction

Solar energy is a source of renewable energy with the potential to meet the global energy challenges faced in today's world. With increasing attention on carbon-neutral energy production, solar energy provides a safe and clean alternative unlike, conventional fossil fuels like coal and gas for power production that causes air, water, and land pollution. The International Energy Agency (IEA) has estimated that for reaching the level of Sustainable Development Scenario (SDS) by 2030, the energy production has to be increased by 16% annually. To increase solar-cell deployment cost-effectively, research and development have focused on lowering manufacturing costs and improving the efficiency of photovoltaic technologies. Crystalline silicon-based solar cells dominate above 90% of the present world market [1]. Despite their high efficiency, the production costs and the necessity of a thick Si crystalline layer lead to high prices compared to the power production. As a result, the search for new materials and technology is essential for large-scale solar electricity deployment to keep up with the increasing energy demand.

Thin-film technology has been proven to be the most cost-effective alternative to silicon-based solar cells. Thin-film technology uses multinary semiconductors made of II-VI or I-III-VI_2 compounds as optical absorbers. An absorber layer with 1μm thickness is sufficient to absorb all the photons in the solar wavelength spectrum. As of now, thin-film technologies based on copper indium gallium selenide (CIGS) and cadmium telluride (CdTe), are the widely commercialized solar absorbers. CIGS and CdTe exhibit promising conversion efficiency of about 22.3 and 22.1%, respectively [2]. Despite their efficiency, the limited supply of In and Ga makes CIGS costly, and the toxicity of Cd in CdTe is an obstacle for their large-scale production. In recent years, solar cells based on perovskites attracted much attention because of the rapid improvement in efficiency from 3.8% to 25.2% [3]. Though the perovskite solar cells achieved high efficiencies in laboratory-scale over the other thin-film absorber materials, they have stability issues lowering their commercial potential [4]. Ideally, solar cell technologies should consider the use of environmentally friendly and earth-abundant materials without compromising on efficiency and lifetime.

In this respect, kesterite Cu_2ZnSnS_4 (CZTS) has attracted much interest as an absorber layer for thin-film solar cells. CZTS is composed of earth-abundant, non-toxic, and eco-friendly elements. Over the years of extensive research, CZTS compounds have proven to be promising materials as absorber layers for solar cells. CZTS is a p-type semiconductor, with a direct band gap of 1.45 eV, and absorption coefficients exceeding 10^4 cm^{-1} in the visible range

[5, 6, 7]. The maximum conversion efficiency recorded is 11.0% [8] which falls far below the predicted efficiency from the Shockley-Queisser limit. For CZTS to be a viable absorber material and for production on the industrial scale, it requires further extensive research.

One factor limiting the performance of the solar cell is the electronic properties, which mainly depend on the chemical composition of the absorber material. Thus, it is necessary to grow samples of good quality to be incorporated into the devices. CZTS being a quaternary compound can manifest imperfections like secondary phases and defects. These imperfections lead to, for instance, bandgap fluctuations. It is essential to study the chemical composition and electronic characteristics of the material including imperfections, to optimize the performance of the CZTS compound. X-ray absorption near edge structure (XANES) represents a powerful tool for this purpose. It is an element-specific and local geometry sensitive spectroscopic analysis that sheds light on the electronic characteristics of the material. Interpretation of XANES is nontrivial and thus requires theoretical modeling.

An accurate description and analysis of such excitations can be obtained by *ab-initio* techniques. density-functional theory (DFT) permits obtaining the ground-state properties of materials. To describe the electronic excitations, it is necessary to go beyond DFT. This is realized in the framework of Many-body pertubation theory (MBPT) [9]. Within this framework, one can calculate single-particle excitations (i.e. electron addition and removal energies) using the *GW* approximation [10] and absorption spectra including elecron-hole (*e-h*) interactions are well described by the solution of Bethe-Salpeter equation (BSE) [11, 12]. To successfully interpret experimental data it is important to include *e-h* interactions. The BSE approach has been performed successfully to study excitaions from valence bands and core levels from different edges in several materials [13, 14, 15, 16, 17].

In this work, we adopt the BSE of MBPT to calculate XANES using a fully relativistic treatment of the core region [18, 14] as implemented in the `exciting` code [19, 18]. By using the linearized augmented planewaves (LAPW) basis set, all electrons can be treated in the same manner, and thus also reliably describe excitations from the core region [20]. There have been several studies reported on the electronic structure of CZTS, but precise knowledge to quantify the defects is still missing. The focus of this work is to compute XANES from sulfur K and $L_{2,3}$ edges in Cu_2ZnSnS_4 and related secondary phases and defect structures. The latter is studied for comparison to the single-phase CZTS, as we can learn about the origin of specific spectral features and their effect on the absorption properties.

2.1. Historical overview

Cu_2ZnSnS_4 (CZTS) naturally occurs as kesterite mineral $Cu_2(Fe, Zn)SnS_4$ with some iron content. CZTS was first fabricated in 1967 by Nitsche *et al.* [21] using chemical vapor deposition. The photovoltaic effect was first characterized on thin-film synthesized by atom-beam sputtering on a stainless steel substrate by Ito and Nakazawa in 1988 [22]. Early progress of CZTS-based solar cells was reported by Katagiri *et al.* [23] with a conversion efficiency of 0.66%. There have been steady improvements in conversion efficiency, reaching 6.7% in 2007. Since then, research on CZTS-based solar cells has attracted much attention. A wide variety of techniques are used to develop CZTS solar cells. Currently, the highest efficiency is about 11.0 % [24] is reported. Alongside the improvement in the conversion efficiency, the quaternary structure of CZTS is often compounded with other elements. Most commonly, Se is mixed to form $Cu_2ZnSn(S_xSe_{1-x})_4$ (CZTSSe) or $Cu_2ZnSnSe_4$ (CZTSe). The intermixing of S and Se forming CZTSSe was first introduced by IBM reporting conversion efficiency of 9.7% [25]. In 2013, they reported the world's highest recorded efficiency of 12.6% [26]. Despite these improvements, studies on the fundamental characteristics of the material itself are limited.

2.2. CZTS as solar cell absorber

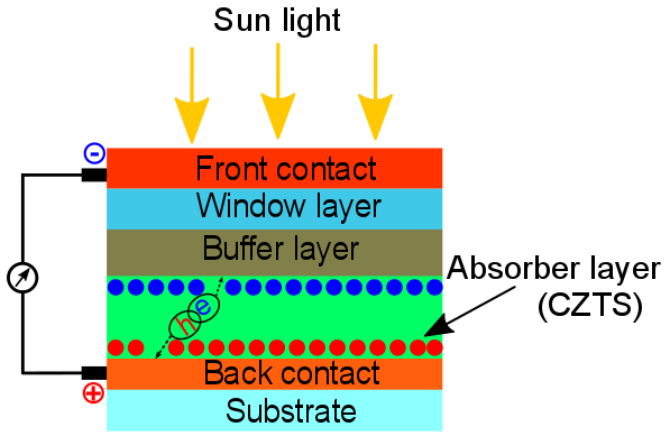

Figure 2.1.: The heterojunction thin-film solar cell structure.

An essential component of a solar cell device is the absorber layer, where most of the incident photons are absorbed. A typical heterojunction photovoltaic device structure is depicted in Fig. 2.1. In the absorber layer, elecron-hole (*e-h*) pairs are created by the absorbed sunlight, and the charge carriers (electrons and holes) are transported to the electrical contacts to produce electricity. The development of CZTS for its use as a photovoltaic absorber initially started as a replacement for $CuIn_xGa_{(1-x)}Se_2$ (CIGS) absorbers. CIGS has the disadvantage of containing expensive and rare elements, In and Ga. By replacing In and Ga with Zn and Sn, CZTS has attracted much interest as an alternate absorber layer. CZTS also have similar optoelectronic properties as CIGS. CZTS is a p-type semiconductor with a direct bandgap of 1.45 eV and has a high absorption coefficient of $\sim 10^4$ cm^{-1} [27, 6, 5, 7]. Owing to the similar optoelectronic properties like CIGS, the development of CZTS-based solar cells uses a similar device architecture and growth methods as in CIGS solar cells [28]. CZTS absorber layer is fabricated using both vacuum-based methods like evaporation and sputtering of CZTS precursors and non-vacuum based methods like electrochemical deposition and hot-injection methods. As mentioned before, the highest efficiency acheiced so far is 11.0 %. The performances are still far away from the Shockley-Queisser limit [29]. For CZTS to become a viable absorber material for production on an industrial scale, it is important to improve the device performance.

2.3. Current challenges

As mentioned in the previous section CZTS adopts the CIGS-based solar cell architecture. Though this device structure helped in the rapid development of CZTS based solar cells, the efficiency falls below that of CIGS solar cells [30]. The record efficiency of the device is increased steadily until a stagnation point a few years ago. The key factor for this fall is the open-circuit (V_{oc}) deficit, which is a long-lasting challenge. The major factor contributing to this deficit is the poor phase purity. An efficient CZTS photovoltaic device requires a single-phase CZTS absorber layer. The complex nature of the quaternary compound, however, opens up the possibilities of lattice defects.

Possible intrinsic defects include vacancies (V_{Cu}, V_{Zn}, V_{Sn}, V_S), anti-sites (Cu_{Zn}, Cu_{Sn}, Zn_{Cu}, Zn_{Sn} Sn_{Cu}, Sn_{Zn}) and interstitials (Cu_i, Zn_i). From all the point defects, it has been reported that Cu_{Zn}, Cu_{Sn}, Zn_{Sn}, V_{Cu}, and V_{Zn} have a formation energy lower than 1.0 eV. The existence of V_{Cu} is reported to be beneficial that enhances *p*-type conductivity. Cu_{Zn} reduces

the bandgap. Charge-neutral defect complexes are formed when the point defects with opposite charges are in close spatial proximity, e.g. V_{Cu}+Cu_{Zn} and Cu_{Zn}+Zn_{Cu}. These defect complexes can be detrimental as they reduce the bandgap [31].

Because of the narrow single-phase CZTS region, the formation of secondary phases is another potential problem. Secondary phases like ZnS, SnS_2, and CuS are reported to be formed during the synthesis of CZTS [32]. The highest efficiency reported so far on CZTS based solar cells are under Cu-poor, and Zn-rich condition [24]. Under this condition, several theoretical studies reported that defect pairs like V_{Cu}+Zn_{Cu} and Cu_{Zn}+Zn_{Cu} and secondary phases (ZnS and SnS_2) have lower formation energy than the other phases [33, 34, 31]. As the binary phases and defect complexes influence the optoelectronic properties and lower the device performance, it is necessary to identify and understand the influence of these phases.

The crystal structures of CZTS and ZnS exhibit similar lattice parameters. Thus their X-ray and neutron diffraction peaks overlap. Synchrotron-based high resolution X-ray absorption near edge structure (XANES) is a powerful tool to address this challenge. The measured spectra can be used as a fingerprint for structural characterization and for identifying the byproducts formed during the synthesis. The interpretation of XANES of complex materials is nontrivial and therefore requires theoretical modeling. *Ab-initio* calculations helps to interpret such experimental data. Many-body pertubation theory (MBPT) offers a state-of-the-art formalism to calculate such neutral excitations. In this work, the XANES are calculated from MBPT by treating elecron-hole (*e-h*) interaction through the solution of Bethe-Salpeter equation (BSE) as implemented in the `exciting` code [19, 18]. The theoretical concepts required to calculate XANES are introduced in the next Chapter.

3.1. X-ray absorption fine structure

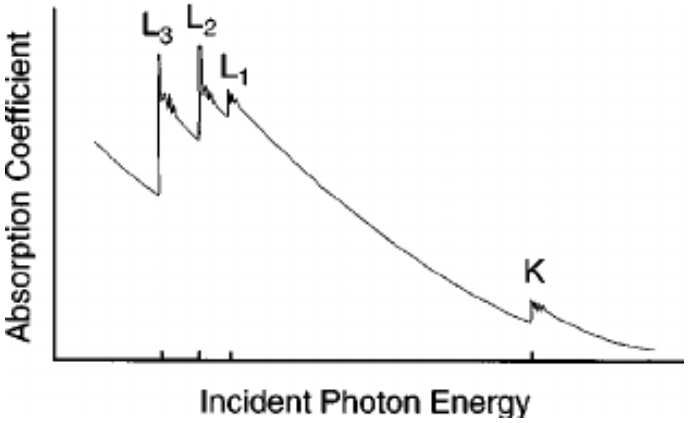

Figure 3.1.: Schematic view of the X-ray absorption spectrum over a broad energy range. Figure taken from [35].

The X-ray absorption spectroscopy measures the absorption coefficient $\mu(E)$, which gives the probability of X-rays that will be absorbed. According to Beer's Law, $\mu(E)$ is expressed as

$$I_t(d) = I_0 e^{-\mu(E)d} \tag{3.1}$$

where I_0 is the intensity of the incoming X-ray beam, d is the sample thickness, and I_t is the transmitted intensity.

A schematic view of the X-ray absorption coefficient $\mu(E)$ as a function of incident photon energy E is shown in Fig. 3.1. It can be observed that there is a decrease in $\mu(E)$ with the increase in energy which is due to the well-known background absorption of the atoms [35]. The sharp rise in the spectrum is called absorption edge, which is followed by a small oscillatory structure. The absorption edge is a unique feature related to a specific atom present in the material, which is formed due to the excitation of inner-shell electrons to unoccupied states. The absorption edges are named according to the initial atomic states in the transition, as listed in Table 3.1. The series of oscillations above the absorption edge is known as X-ray absorption fine structure (XAFS). The XAFS is divided into two distinct regions: X-ray absorption near edge structure (XANES), typically within 40 eV of the absorption edge, and the extended x-ray absorption fine structure (EXAFS) which is a few hundred eV beyond the absorption edge. The EXAFS is used to identify the local geometrical structure of samples

Absorption edge	Initial atomic state
K	$1s_{1/2}$
L_1	$2s_{1/2}$
L_2	$2p_{1/2}$
L_3	$2p_{3/2}$

Table 3.1.: Notation of three absorption edges.

[35]. XANES is an element-specific spectroscopic analysis that determines the electronic structure of the absorbing atom. Theoretical spectroscopy in combination with experiments unfolds the local geometric and electronic structure of the CZTS. The First-principles approach represents an accurate tool for this purpose. density-functional theory (DFT) yields high-quality results limited to ground-state properties. The theoretical description of XANES spectra requires describing the quasi-electron and quasi-hole also their interaction simultaneously. A description of such excitations can be described by the effective two-particle Green's function formalism known as Bethe-Salpeter equation (BSE). Such a theoretical model is comparable to measured spectra.

3.2. Density-functional theory

density-functional theory (DFT) provides a viable theoretical framework to address the complexity of the many-body problem. DFT allows us to map the many-body problem onto a fictitious single-body problem. This section provides an overview of DFT. A detail description can be found in [36, 37]. The conceptual structure of DFT can be summarized by the following sequence:

$$n(r) \Rightarrow \psi(r_1, ..., r_N) \Rightarrow v(r), \tag{3.2}$$

i.e., the electron density n(r) denotes the wavefunction ψ and the potential v(r). The formal justification for this is given by Hohenberg and Kohn in 1964 [38]. A year later, a practical foundation was proposed by Kohn and Sham to obtain an effective single-particle Schrödinger equation based on DFT.

According to the Kohn-Sham (KS) approach, the original many-body problem is replaced by a fictitious system of non-interacting particles with the same density as the real system [37], thus, reducing the problem of solving N interacting electrons to the problem of a single-particle Schrödinger equation. The groundstate density can be obtained by solving the set of following single-particle equations:

$$\left[-\frac{1}{2}\nabla^2 + v_{eff}(r)\right]\psi_i = \epsilon_i\psi_i, \tag{3.3}$$

the density is obtained as:

$$n(r) = \sum_{i=1}^{N} |\psi_i(r)|^2. \tag{3.4}$$

Here ψ_i(r) are the wavefunctions and eigenenergies of the KS system. The KS potential is given by the sum of the external potential v_{ext}(r), the Hatree potential v_H(r), and the exchange-correlation potential v_{xc}(r)

$$v_{eff}(r) = v_{ext} + v_H(r) + v_{xc}(r). \tag{3.5}$$

The exchange-correlation potential is given as the functional derivative of the exchange correlation energy E_{xc} with respect to density

$$v_{xc}(r) = \frac{\delta E_{xc}[n]}{\delta n(r)}. \tag{3.6}$$

The equations 3.3 and 3.4 are known as the Kohn-Sham (KS) equations. As the v_{eff} (3.5) depends on the density the KS equations has to be solved self-consistently.

In practice, the KS equations are exact, provided v_{xc} is known. The exact expression for the exchange-correlation energy E_{xc}[n] is not known, and has to be approximated. The accuracy of DFT in the KS approach depends on finding the most accurate approximation for E_{xc}[n]. There are different types of functionals developed to approximate E_{xc} with improved accuracy, classified as Jacob's ladder [39] were each rung represents the approximation which work better than the previous one. The approximation at the bottom of the ladder depends only on the density whereas the next step includes the modulus of the density gradient and in the higher rung, they include unoccupied KS orbitals [40]. The first and simplest approximation

E_{xc}[n] is the local-density approximation (LDA) [41]. In this framework, the exchange-correlation energy E_{xc}^{LDA}[n] is he integral over all space, assuming that e_{xc}(n(**r**)) is the exchange-correlation energy per particle of a homogeneous electron gas of density n(r).

$$E_{xc}^{LDA}[n(\mathbf{r})] = \int e_{xc}(n(\mathbf{r}))n(\mathbf{r})d^3r, \tag{3.7}$$

Although, LDA has been very successful in the application to atomic and condensed systems, it has limitations when it comes to atomization energies and the nature of the chemical bonds.

An improvement to LDA is done in the generalized gradient approximation (GGA) by including the density gradient ∇n. The GGA exchange-correlation functional is expressed as:

$$E_{xc}^{GGA}[n(\mathbf{r})] = \int f(n(\mathbf{r}), |\nabla n(\mathbf{r})|)n(\mathbf{r})d^3r, \tag{3.8}$$

where, f is a function of $n(\mathbf{r})$ and the density gradient ∇n. Several forms of the functions f have been proposed in the literature. Among all the most widely used, including in this work, functional developed by Perdew, Burke, and Ernzerhof parametrization (PBE) [42] is used.

3.3. Basis-set expansion

In this work we use the **exciting** code which uses the linearized augmented planewaves (LAPW) method for solving the KS equations. For more details see [19].

In practice, to solve the KS equation (Eq. 3.3) the wavefunctions are expanded in a basis set $\phi_{i\mathbf{k}}$ as:

$$\psi_{\mathbf{k}}(r) = \sum_i c_{i\mathbf{k}}\phi_{i\mathbf{k}}(r). \tag{3.9}$$

This gives a matrix equation

$$[H(\mathbf{k}) - \epsilon_i S(\mathbf{k})]\tilde{c}(\mathbf{k}) = 0 \tag{3.10}$$

which has to be solved for every **k**-point in the first BZ. The Hamiltonian

matrix $H(\mathbf{k})$ is expressed as:

$$H_{ij}(\mathbf{k}) = \int_{\Omega} (\phi_{i\mathbf{k}}(\mathbf{r}))^* \left[-\frac{1}{2}\nabla^2 + v_{eff}(\mathbf{r}) \right] \phi_{j\mathbf{k}}(\mathbf{r}) d^3r, \tag{3.11}$$

the overlap matrix $S(\mathbf{k})$ with the elements

$$S^{ij}(\mathbf{k}) = \int_{\Omega} (\phi_{i\mathbf{k}}(\mathbf{r}))^* \phi_{j\mathbf{k}}(\mathbf{r}) d^3r. \tag{3.12}$$

The Hamiltonian and overlap matrices have the size $M \times M$. M is the number of basis functions, and $\tilde{c}(\mathbf{k})$ has the length of the basis functions for a given k-point. Ω represents the volume of the unit cell. The eigenvalues are obtained by diagonalizing the matrix in Eq. 3.10. The choice of the basis set is important as the in computational cost and accuracy depends on it. In the LAPW+LO basis set, the unit cell is separated into two regions: (1) the muffin-tin spheres around the nuclei and (2) the interstitial region between the spheres (see Fig. 3.2). Atomic-like functions are employed to describe the wavefunctions inside the muffin-tin spheres. In the interstitial region, planewaves are employed. The basis functions in the APW are expressed as:

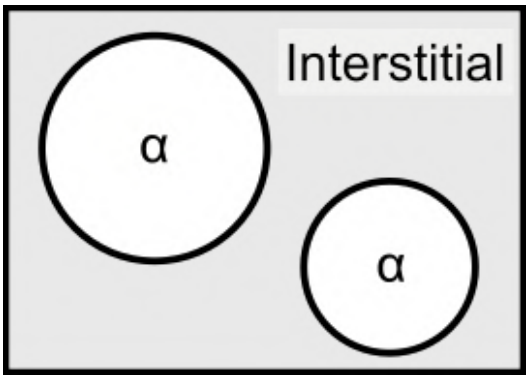

Figure 3.2.: Partition into interstitial (I) and *muffin-tin (MT) region of the unit cell.*

$$\phi_{\mathbf{G}+\mathbf{k}(\mathbf{r})} = \begin{cases} \sum_{lm} A_{lm\alpha}^{\mathbf{G}+\mathbf{k}} u_{l\alpha}(r_\alpha; \epsilon) Y_{lm}(\hat{\mathbf{r}}_\alpha) & for \quad r_\alpha \leq R_{MT} \\ \frac{1}{\sqrt{\Omega}} e^{i(\mathbf{G}+\mathbf{k})\mathbf{r}} & for \quad \mathbf{r} \in I \end{cases} \tag{3.13}$$

where R_{MT}^{α} is the muffin-tin radius of the atoms α positioned at $\mathbf{R}_\alpha$. The coefficient $A_{lm\alpha}^{\mathbf{G}+\mathbf{k}}$ ensure the continuity of the basis functions at the boundary between the interstitial and muffin-tin regions. The basis functions within the muffin-tin spheres are formed by the radial functions $u_{l\alpha}(r_\alpha)$ which depends on the energy ϵ. This leads to the non-linear eigenvalue problem. In order to linearize this, the LAPW method is introduced. In the LAPW

method, the radial function $u_{l\alpha}(r_\alpha)$ is expanded to first order around the linearization energy ϵ_l as:

$$u_{l\alpha}(r_\alpha;\epsilon) \approx u_{l\alpha}(r_\alpha;\epsilon_{l\alpha}) + (\epsilon_{l\alpha} - \epsilon)\dot{u}_{l\alpha}(r;\epsilon_{l\alpha}). \tag{3.14}$$

The resulting LAPW basis in the muffin-tin sphere are given by:

$$\phi_{\mathbf{G}+\mathbf{k}}(r) = \sum_{lm}\left[A_{lm\alpha}^{\mathbf{G}+\mathbf{k}}u_{l\alpha}(r_\alpha;\epsilon_{l\alpha}) + B_{lm\alpha}^{\mathbf{G}+\mathbf{k}}\dot{u}_{l\alpha}(r_\alpha;\epsilon_{l\alpha})\right]Y_{lm}(\hat{r}_\alpha), \tag{3.15}$$

where the coefficients $A_{lm\alpha}^{\mathbf{G}+\mathbf{k}}$ and $B_{lm\alpha}^{\mathbf{G}+\mathbf{k}}$ are obtained by the continuity of the basis functions and their first derivatives at the boundaries between the interstitial and muffin-tin regions.

An alternate approach to the linearization is given by the APW+LO approach [43] which is defined as:

$$\phi_{\mathbf{G}+\mathbf{k}}(r) = \sum_{lm} A_{lm\alpha}^{\mathbf{G}+\mathbf{k}}u_{l\alpha}(r_\alpha;\epsilon_{l\alpha})Y_{lm}(\hat{r}_\alpha). \tag{3.16}$$

By introducing the additional basis functions the linearization error is reduced. The additional basis functions are called local orbitals (LO), ϕ_μ expressed as:

$$\phi_\mu(\mathbf{r}) = \begin{cases} \delta_{\alpha\alpha_\mu}\delta_{ll_\mu}\delta_{mm_\mu}\left[a_\mu u_l\alpha(r_\alpha;\epsilon_{l\alpha}) + b_\mu\dot{u}_{l\alpha}(r_\alpha;\epsilon_{l\alpha})\right]Y_{lm}(\hat{r}_\alpha) & for \quad r_\alpha \leq R_{MT} \\ 0 & for \quad r \in I \end{cases} \tag{3.17}$$

where the coefficients a_α and b_α are defined by the continuity condition of $\phi_\mu(r)$ and its normalization to one.

3.4. Many-body perturbation theory

The introduced formalism in the previous sections allow to compute the properties of the system in the groundstate. However, to compute the excited states as in the absorption experiment one has to go beyond DFT. To understand the absorption experiments it requires to describe the creation of quasi-electron and quasi-hole also their interaction simultaneously. Therefore, in this section the concepts of MBPT capable to describe the

neutral excitations is introduced. A more detail description of MBPT and its applications can be found in [44, 45, 46].

3.4.1. Dielectric response

The general form of the dielectric tensor ϵ is given by linearly connecting the electric displacement D to the electric field E

$$D_i(\mathbf{r},\omega) = \int \epsilon_{ij}(\mathbf{r},\mathbf{r}',\omega)E_j(\mathbf{r},\omega)d^3r'. \tag{3.18}$$

The dielectric tensor ϵ can be reformulated in terms of the polarization P:

$$\epsilon^{-1}(\mathbf{r},\mathbf{r}',\omega) = \delta(\mathbf{r},\mathbf{r}') + \int v(\mathbf{r},\mathbf{r}'')P(\mathbf{r},\mathbf{r}'',\omega)d^3r'', \tag{3.19}$$

where $v(r,r')$ is a bare Coulomb potential and the complete polarization P is defined as the variation of the density with respect to the external potential. The dielectric tensor for the materials with translational symmetries can be Fourier transformed into reciprocal space and is expressed as:

$$\epsilon(\mathbf{r},\mathbf{r}',\omega) = \frac{1}{\Omega}\sum_{\mathbf{q}}\sum_{\mathbf{G},\mathbf{G}'} e^{-i(\mathbf{q}+\mathbf{G})\mathbf{r}}\epsilon(\mathbf{q}+\mathbf{G},\mathbf{q}+\mathbf{G}',\omega)e^{-i(\mathbf{q}+\mathbf{G}')\mathbf{r}'}. \tag{3.20}$$

Here $\mathbf{q}$ is a vector from the first Brilloiun zone (BZ). $\mathbf{G}$ and $\mathbf{G}'$ represent reciprocal lattice vectors and Ω is the volume of the crystal. While discussing optical spectroscopy, the interest is in the average response of the system to the incoming light rather than the variation of the response on an atomic scale. The average response is given by the macroscopic dielectric function $\epsilon(\mathbf{q},\omega)$, which is obtained via the $G = G' = 0$ component of the inverse microscopic tensor, expressed as $\epsilon^{-1}(\mathbf{q},\mathbf{q},\omega)$:

$$\epsilon(\mathbf{q},\omega) = \frac{1}{\epsilon^{-1}(\mathbf{q},\mathbf{q},\omega)}. \tag{3.21}$$

From Eq. 3.19 the inverse microscopic dielectric function can be obtained by calculating the complete polarization P.

3.4.2. Bethe-Salpeter equation

The key quantity in the calculation of two-particle excited states is the polarization P. The polarization P is connected to the two particle correlation

function $L(1,1,2,2)$:

$$P(1,2) = -iL(1,1,2,2). \tag{3.22}$$

The two-particle correlation function L is expressed as:

$$L(1,1',2,2') = G_2(1,1',2,2') - G(1',2')G(1,2), \tag{3.23}$$

where L is the part of two-particle Green's function G_2 (describing the propagation of electron and hole) which excludes the disconnected term consisting of two single-particle Green's functions $G(1',2')G(1,2)$. Note that the function L_0 is introduced describing independent motion of two one-particle Green's functions as

$$L_0(1,1',2,2') = G(1',2')G(1,2), \tag{3.24}$$

The notation of (1) represents the particle is in position $\mathbf{r}1$ at time $\mathbf{t}1$ $(\mathbf{r}1,\mathbf{t}1)$ and similarly (2) represents the particle is in position $\mathbf{r}2$ at time $\mathbf{t}2$ $(\mathbf{r}2,\mathbf{t}2)$. The Bethe-Salpeter equation (BSE) assumes the form of a Dyson's-like equation for the function L:

$$L(1,1',2,2') = L_0(1,1',2,2') + \int d(3,3',4,4')L_0(1,1',3,3')\Xi(3,3',4,4')L(4,4',2,2'). \tag{3.25}$$

and the kernel Ξ contains the effective two-particle interactions. It is given by the derivative of the Hartree potential V_H and the self-energy $\sum$:

$$\Xi(3,3',4,4') = \frac{\partial[V_H(4,4') + \sum(4,4')]}{\partial G(3,3')}. \tag{3.26}$$

The Hartree potential V_H is expressed in terms of the one-particle Green's function:

$$V_H(4,4') = -i\delta(4,4')\int G(5,5^+)v(5,4)d(5). \tag{3.27}$$

In practice the exact form of the kernal Ξ is unknown. To calculate Ξ it is necessary to approximate the self-energy. The standard approximation is to use the self-energy in the GW-approximation [10]:

$$\sum(1,2) = iG(1,2)W(1,2), \tag{3.28}$$

where $W(1,2)$ is the dynamically screened Coulomb interaction which is expressed as

$$W(1,2) = \int \epsilon^{-1}(1,3)v(3,2)d(3), \tag{3.29}$$

with the dielectric matrix ϵ expressed in the random-phase approximation (RPA):

$$\epsilon(1,2) = \delta(1,2) + i\int v(1,3)G(2,3)G(3,2)d(3). \tag{3.30}$$

The interaction kernal Ξ can be obtained by inserting Eq. 3.29 and Eq. 3.30 into Eq. 3.26:

$$\begin{aligned}\Xi(3,3',4,4') = -i\delta(3,3')\delta(4,4')v(3,4) + i\delta(3,4')\delta(3',4')W(3,3') \\ +iG(4,4')\frac{\partial W(4,4')}{\partial G(3,3')}.\end{aligned} \tag{3.31}$$

The first term contains the repulsive and unscreened exchange interaction and the second term describes the electron-hole attraction given by screened interaction W defined in Eq. 3.29. The contribution of the last term is small in comparison with the other two terms. Therefore, the latter term can be neglected in the numerical evaluation of the BSE. Thus, the interaction kernal Ξ can be expressed as:

$$\Xi(3,3',4,4') = -i\delta(3,3')\delta(4,4')v(3,4) + i\delta(3,4')\delta(3',4')W(3,3'). \tag{3.32}$$

3.4.3. Reformulation of the BSE

To simplify the numerical evalution of BSE (Eq. 3.25), this section shows how the BSE can be reformulated from an integral equation into an eigenvalue problem. A detailed treatment can be found in [45, 47].

The four-point functions L, L_0, and Ξ must obey the transnational symmetry of the crystal for a given lattice vector $\mathbf{R}$

$$L(\mathbf{r}_1 + \mathbf{R}, \mathbf{r}_1' + \mathbf{R}, \mathbf{r}_2 + \mathbf{R}, \mathbf{r}_2' + \mathbf{R}) = L(\mathbf{r}_1, \mathbf{r}_1', \mathbf{r}_2, \mathbf{r}_2'). \tag{3.33}$$

Therefore, the four-point functions can be expressed as a sum over functions $L_\mathbf{q}$, where $\mathbf{q}$ is a vector from the first BZ expressed as:

$$L(\mathbf{r}_1, \mathbf{r}_1', \mathbf{r}_2, \mathbf{r}_2') = \sum_\mathbf{q} L_\mathbf{q}(\mathbf{r}_1, \mathbf{r}_1', \mathbf{r}_2, \mathbf{r}_2'). \tag{3.34}$$

The vector $\mathbf{q}$ can be identified as the momentum of the external perturbation.

The interest of this work lies in the optical limit of X-ray spectroscopy, $\mathbf{q}\to 0$. Thus, only the L_0 contribution is considered, and it is indicated as $L(1,1',2,2')$. Therefore, this functions can be expanded in the basis of the quasi-particle wavefunctions which can be approximated by the KS orbitals $\psi_{n\mathbf{k}}$:

$$L(\mathbf{r}_1,\mathbf{r}_1',\mathbf{r}_2,\mathbf{r}_2') = \sum_{i_1,i_2,i_3,i_4} \psi_{i_1}^*(\mathbf{r}_1)\psi_{i_2}^*(\mathbf{r}_1')\psi_{i_3}^*(\mathbf{r}_2)\psi_{i_4}^*(\mathbf{r}_2')L_{(i_1i_2)(i_3i_4)}. \tag{3.35}$$

With this the correlation function can be expressed as the matrix equation:

$$L_{(i_1i_2)(i_3i_4)} = \sum_{j_3j_4}\left[1 - L^0(\omega)\Xi\right]^{-1}_{(i_1i_2)(j_3j_4)} L^0_{(j_3j_4)(i_1i_2)}. \tag{3.36}$$

As mentioned before (Eq. 3.24) the independent-particle correlation function L_0 is the product of two-single particle Green's functions describing the independent motion of an electron and the hole. Therefore, the function L^0 can be expressed as

$$L^0_{(i_1i_2),(i_3i_4)} = -i\frac{(f_{i_2} - f_{i_1})\delta_{(i_1i_3),(i_2i_4)}}{\epsilon_{i_2} - \epsilon_{i_1} - \omega - i\delta}, \tag{3.37}$$

where f represents the Fermi-distribution, and ϵ are the single particle energies. The excitonic Hamiltonian is introduced to the matrix equation using this basis representation which is expressed as:

$$H^e_{(j_1j_2)(j_3j_4)} = (\epsilon_{j_2} - \epsilon_{j_1})\delta_{(j_1j_3)}\delta_{(j_2j_4)} - i(f_{j_2} - f_{j_1})\Xi_{(j_1j_2)(j_3j_4)}, \tag{3.38}$$

and L can be expressed as

$$L_{(i_1i_2)(i_3i_4)}(\omega) = i\left[H^e - \omega\right]^{-1}_{(i_1i_2)(i_3i_4)}(f_{i_4} - f_{i_3}). \tag{3.39}$$

Now, the two-particle correlation function L is obtained by an inversion of the excitonic Hamiltonian for each frequency ω.

Due to the various orbital-index combinations the structure of the *e-h* Hamiltonian (Eq. 3.39) is complicated. However for core spectroscopy Eq. 3.39 can be simplified as all excitations occur from occupied core states c (f_c=1) to unoccupied states u (f_u=0). A detailed analysis of H_e is given in [46], the reduced block structure H_e is:

$$H_e = \begin{pmatrix} H^e_{c_1u_1\mathbf{k}_1,c_2u_2\mathbf{k}_2} & H^e_{c_1u_1\mathbf{k}_1,u_2c_2\mathbf{k}_2} \\ H^e_{u_1c_1\mathbf{k}_1,c_2u_2\mathbf{k}_2} & H^e_{u_1c_1\mathbf{k}_1,u_2c_2\mathbf{k}_2} \end{pmatrix}, \tag{3.40}$$

with

$$H^{e}_{c_1u_1\mathbf{k}_1,c_2u_2\mathbf{k}_2} = (\epsilon_{u_1\mathbf{k}_1} - \epsilon_{c_1})\delta_{c_1c_2}\delta_{u_1u_2} + \Xi_{c_1u_1\mathbf{k}_1,c_2u_2\mathbf{k}_2} \tag{3.41}$$

$$H^{e}_{c_1u_1\mathbf{k}_1,u_2c_2\mathbf{k}_2} = i\Xi_{c_1u_1\mathbf{k}_1,u_2c_2\mathbf{k}_2} \tag{3.42}$$

$$H^{e}_{u_1c_1\mathbf{k}_1,c_2u_2\mathbf{k}_2} = -\left[H^{e}_{c_1u_1\mathbf{k}_1,u_2c_2\mathbf{k}_2}\right]^{*} \tag{3.43}$$

$$H^{e}_{u_1c_1\mathbf{k}_1,u_2c_2\mathbf{k}_2} = -\left[H^{e}_{c_1u_1\mathbf{k}_1,c_2u_2\mathbf{k}_2}\right]^{*}. \tag{3.44}$$

By the Tamm-Dancoff approximation (TDA) [48], the matrix size can be further reduced by neglecting the off-diagonal blocks (Eqs: 3.42 and 3.43). This approximation is justified in the optical limit only if the binding energies are small compared to the band gap [48]. In this study, X-ray absorption spectroscopy is considered in the optical limit where the binding energies are in the range of few eV thus, the TDA is considered. Now, the Hamiltonian H_e takes block-diagonal form, and the eigenvalues and eigenvectors of Eq. 3.42 uniquely define the eigenvalues and eigenvectors of Eq. 3.44. The eigenvalue problem is expressed as:

$$\sum_{c'u'\mathbf{k}'} H^{BSE}_{cu\mathbf{k},c'u'\mathbf{k}'} A^{\lambda}_{c'u'\mathbf{k}'} = E^{\lambda} A^{\lambda}_{cu\mathbf{k}}. \tag{3.45}$$

The eigenvectors $A^{\lambda}_{cu\mathbf{k}}$ are the expansion coefficients of the excitonic wavefunction $\Phi^{\lambda}(\mathbf{r}, \mathbf{r}')$ with transition energy E^{λ} in the single-particle wavefunction of an electron and the hole:

$$\Phi^{\lambda}(\mathbf{r}_e, \mathbf{r}_h) = \sum_{cu\mathbf{k}} A^{\lambda}_{cu\mathbf{k}} \psi_{u\mathbf{k}}(\mathbf{r}_e)\psi_{c\mathbf{k}}(\mathbf{r}_h)^{*}. \tag{3.46}$$

where, $\mathbf{r}_e$ and $\mathbf{r}_h$ are the positions of the excited electron and the hole, respectively. With the solution to the eigenvalue problem and using the spectral theorem, the correlation function L can be expressed in terms of eigenvalues and eigenfunctions as:

$$L_{c_1u_1\mathbf{k}_1,c_2u_2\mathbf{k}_2} = -i\sum_{\lambda} \frac{A^{\lambda}_{c_1u_1\mathbf{k}_1}\left[A^{\lambda}_{c_2u_2\mathbf{k}_2}\right]^{*}}{E^{\lambda} - \omega}. \tag{3.47}$$

The transistion coefficient t^{λ} can be obtained as:

$$t_{\lambda} = \sum_{cu\mathbf{k}} A^{\lambda}_{cu\mathbf{k}} \frac{\langle c\mathbf{k}|\hat{\mathbf{p}}|u\mathbf{k}\rangle}{\epsilon_{u\mathbf{k}} - \epsilon_c}, \tag{3.48}$$

where, $\langle c\mathbf{k}|\hat{\mathbf{p}}|u\mathbf{k}\rangle$ is the momentum matrix element. $\epsilon_{u\mathbf{k}}$ and ϵ_c are the single-particle energies of the conduction and core state respectively. In

all-electron calculation the core states are accurately treated by considering the relativistic effects. The relativistic corrections including the spin-orbit splitting can be obtained if the electron energies and wavefunctions are determined Dirac equation. The conduction states are treated in the zero-order regular approximation (ZORA) to the Dirac equation without the spin-orbit coupling term, thereby taking into account relativistic effects within the muffin-tin spheres. A detailed description of the core and the conduction states can be found in [20].

Using Eq. 3.48, the imaginary part of the dielectric tensor can be obtained as:

$$Im\epsilon_M(\omega) = \frac{8\pi^2}{\Omega}|t_\lambda|^2\delta(\omega - E_\lambda). \tag{3.49}$$

3.5. The effective electron-hole Hamiltonian

The effective Hamiltonian H^{BSE} can be obtained by using Eq. 3.41:

$$H^e_{cu\mathbf{k},c'u'\mathbf{k}'} = (\epsilon_{u\mathbf{k}-\epsilon_c})\delta_{cc'}\delta_{uu'} + i\Xi_{cu\mathbf{k},c'u'\mathbf{k}'}, \tag{3.50}$$

where the interaction kernel is defined by Eq.3.35:

$$\Xi_{(i_1i_2),(i_3i_4)} = \int d^3r_1 d^3r_1' d^3r_2 d^3r_2' \psi_{i_1}(\mathbf{r}_1)\psi^*_{i_2}(\mathbf{r}_1')\psi^*_{i_3}(\mathbf{r}_2)\psi_{i_4}(\mathbf{r}_2')\Xi(\mathbf{r}_1,\mathbf{r}_1',\mathbf{r}_2,\mathbf{r}_2'). \tag{3.51}$$

As discussed in previous section, the two-particle correlation function are expanded in single-particle wavefunctions $\psi_{i_1}(\mathbf{r})$, where the spin characters of these single-particle states are neglected as the spinorial states are used to include the spin-orbit coupling of the core states. To treat the spin-orbit coupling of the core states, the spin index ($\sigma = 1, 2$) for spin-up and spin-down state is introduced in the following.

The effective Hamiltonian has three terms

$$H^{BSE} = H^{diag} + H^x + H^c. \tag{3.52}$$

given by

$$H^{diag}_{cu\mathbf{k},c'u'\mathbf{k}'} = (\epsilon_{u\mathbf{k}} - \epsilon_c)\delta_{cc'}\delta_{uu'}\delta_{\mathbf{k}\mathbf{k}'}, \tag{3.53}$$

$$H^x_{cu\mathbf{k},c'u'\mathbf{k}'} = \int d^3r d^3r' \sum_\sigma \psi_{c\mathbf{k}\sigma}(\mathbf{r})\psi^*_{u\mathbf{k}\sigma}(\mathbf{r})\bar{v}(\mathbf{r},\mathbf{r}')\sum_{\sigma'}\psi^*_{c'\mathbf{k}'\sigma'}(\mathbf{r}')\psi_{u'\mathbf{k}'\sigma'}(\mathbf{r}'), \tag{3.54}$$

$$H^{c}_{cu\mathbf{k},c'u'\mathbf{k}'} = -\int d^3r d^3r' \sum_{\sigma} \psi_{c\mathbf{k}\sigma}(\mathbf{r})\psi^{*}_{c'\mathbf{k}'\sigma}(\mathbf{r})W(\mathbf{r},\mathbf{r}') \sum_{\sigma'} \psi^{*}_{u\mathbf{k}\sigma'}(\mathbf{r}')\psi_{u'\mathbf{k}'\sigma'}(\mathbf{r}'). \tag{3.55}$$

The diagonal term H^{diag} contains the differences between the quasi-particle energies of the electron and the hole which gives the independant particle approximation (IPA) spectrum. The exchange term H^{x} contains the repulsive exchange part of the *e-h* pairs given by the short-range part of the bare Coulomb potential $\bar{v}$. The third term H^{c} contains the attractive part of the *e-h* interaction and contains the screened Coulomb interaction W.

In X-ray absorption spectroscopy, the BSE Hamiltonian can be separated into individual atomic contributions [20]. Therefore, the imaginary part of macroscopic dielectric function can also be expressed as a sum of the different atomic contributions

$$Im\epsilon_M = \sum_{\alpha} Im\epsilon^{\alpha}_M. \tag{3.56}$$

In this work, the individual atomic contributions is calculated for all calculations. For more details see [20].

The accurate description of the core electrons in **exciting** code is obtained by a fully relativistic treatment with spinor wavefunctions. Using the **exciting** code, the core level excitations can be computed preciously by the following procedure:

1. The electronic structure is calculated by solving the Kohn-Sham (KS) equation of density-functional theory (DFT).

2. The solution of BSE is obtained using step 1 as starting point. Note that the calculated absorption onset is underestimated. Therefore, a scissors operator is applied to the calculated spectra to compare with measured spectra.

The XANES of CZTS is calculated using a supercell with 32 atoms in 2 x 2 x 1 kesterite unit cell. The supercell is fully relaxed until the residual forces are smaller than 0.06 eV/Å. As a starting point for the BSE , the KS electronic structure is calculated within the GGA with PBEsol parametrization **cite**. For ground-state calculation of CZTS a **k**-point mesh of 6 x 6 x 6 is used to sample the Brilloiun zone (BZ). For the basis function, a plane-wave cut-off $R_{MT}G_{max}$ = 7 bohr is applied. Muffin-tin (R_{MT}) spheres of radii 2.28 bohr are used for Cu, Zn and Sn and 1.87 bohr are considered for S. The core spectra are calculated using a 4 x 4 x 4 **k**-grid. To solve the BSE equation, 250 unoccupied bands are considered for screening and diagonalization of the BSE Hamiltonian.

The XANES of defect complexes Cu_{Zn}+Zn_{Cu} and V_{Cu}+Zn_{Cu} in CZTS are calculated using a supercell with 32 atoms. The defect complexes are introduced in 2 x 2 x 1 and 2 x 1 x 2 supercells were the point donor Zn_{Cu} and the acceptor V_{Cu} and Cu_{Zn} are placed closely to each other. Starting from the lattice parameters [49] the geometry is relaxed until residual forces per atom are smaller than 0.05 eV/Å. For the groundstate and excited state calculation the parameters used to obtain the absorption spectra of single-phase CZTS are used.

As a starting point for the BSE the KS electronic structure is computed within the GGA with PBEsol parametrization **cite**. For ground-state calculation a **k**-point mesh of 10 x 10 x 6 and 10 x 10 x 10 is used to sample the BZ for SnS_2 and ZnS respectively. A plane-wave cutoff of $R_{MT}G_{max}$ = 7 is applied for both the materials. Muffin-tin (R_{MT}) spheres of radii 2.0 bohr are considered for Zn and Sn and 1.45 bohr are considered for S. The BSE spectra from the K and $L_{2,3}$ edges are calculated using **k**-mesh of 10 x 10 x 6 is used for SnS_2

and 10 x 10 x 10 for ZnS. 65 conduction bands for screening and 45 empty bands are used in BSE Hamiltonian for both ZnS and SnS_2.

Part Results

The quaternary semiconductor Cu_2ZnSnS_4 (CZTS) is formed in two types of tetragonal crystal structures: the one is kesterite-type with the space group $I\bar{4}$ and the stannite-type structure with space group $I\bar{4}2m$. It has been reported that the kesterite structure has the lowest total energy and is more stable than the stannite-type [50, 51, 52]. In this work, the focus lies on the kesterite-type CZTS. The crystal structure of CZTS is shown in Fig. 5.1. In kesterite structure, Cu, Zn, Sn and S occupy 2*a*, 2*c*, 2*b*, and 8*g* Wyckoff positions, respectively. The cations Cu, Zn, and Sn are tetrahedrally bonded to the S anions. Likewise, each S ion coordinates with two Cu, one Zn, and one Sn ions.

Starting from the experimental lattice parameters and atomic positions [53] structure optimization were performed within the KS DFT framework as implemented in the `exciting` code [19]. The structure optimization yields the lattice parameters $a = b = 5.46$ Å and $c = 10.92$ Å which is in good agreement with experiment [6].

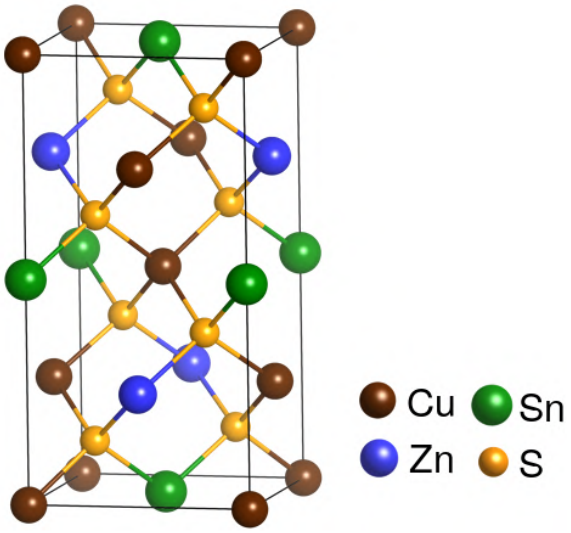

Figure 5.1.: Conventional unit cell of the body-centered kesterite structure Cu_2ZnSnS_4 (CZTS) having two copper (brown), two zinc (blue), two tin (green), and eight sulfur (orange) atoms per unit cell.

5.1. Electronic Structure

In this section, the analysis of the electronic structure is discussed. The quantum-mechanical selection rules determine the dipole allowed transitions from the core to conduction states to generate the spectral features. Therefore, the analysis of electronic properties is of key importance to understand the x-ray absorption spectra. Starting from the optimized structure, the electronic structure is calculated by solving the KS equation of DFT (see Chapter 3). All the electronic structure calculations were performed on the GGA-PBE level. For more computational details, see Chapter 4.

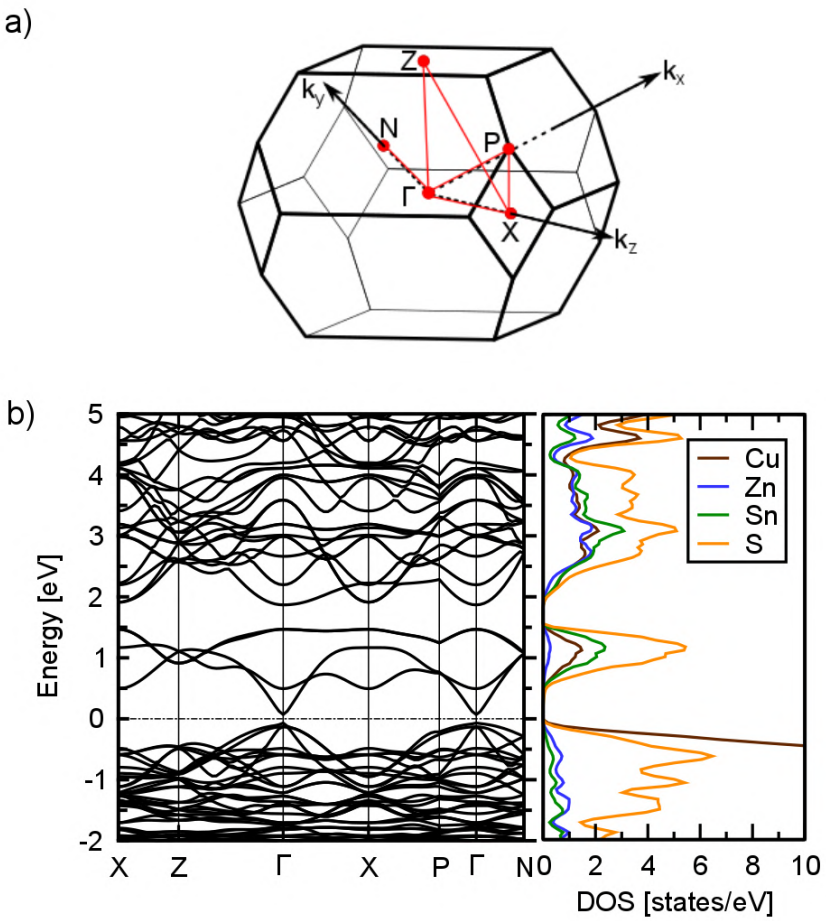

Figure 5.2.: a) The Brilloiun zone (BZ) of CZTS showing the locations of the high-symmetry points. c) Band structure of CZTS and projected density of states for the energy region between -2 and 5 eV.

In Fig. 5.2(a), the Brilloiun zone (BZ) of the body-centered tetragonal structure and the location of the high-symmetry points used to calculate the band structure is shown. The band structure and the partial density of states

(PDOS) calculated on the GGA-PBE level is shown for the energy region between -2 and 5 eV in Fig. 5.2(b). CZTS crystals have a direct bandgap at the Γ-point. The computed KS gap is 0.43 eV. The bands around the bandgap (-0.8 to 1.45 eV) are strongly dispersive. The bands at energies above 2 eV are less dispersive. From the PDOS (right-panel), one can see that the major contributions to the valance bands are from Cu and S states. The low-lying conduction bands are dominated by contributions from Sn and S. Zn states do not influence the bandgap region as they are located deeper in energy. These results are in good agreement with previously reported calculations of the electronic structure [54, 55, 56].

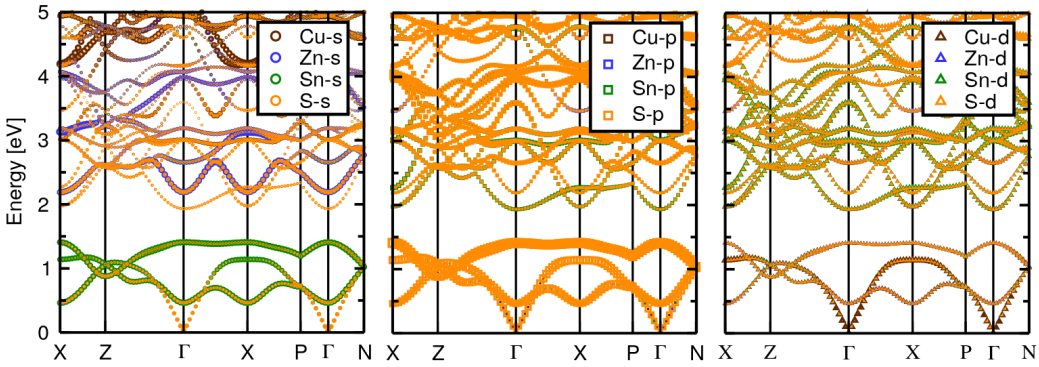

Figure 5.3.: Atomic *s* (left), *p* (middle) and *d* (right) characters projected on the band structure of CZTS in the conduction band region. The color code indicates contributions from Cu (brown), Zn (blue), Sn (green), S (orange). The size of the symbols quantifies the weight of *s*, *p* and *d* characters.

To understand the final states of the x-ray absorption spectra, the focus of this section lies in the unoccupied region of the band structure. Figure 5.3 displays the atomic-orbital characters projected on the conduction band structure. The majority of contributions to the low-lying conduction bands up to 1.45 eV are from Sn-5*s* and S-3*p* states with minor contributions from Cu-3*d* states. The bands in the energy range between 2.2 to 4 eV are dominated by contributions from Zn-4*s*, S-3*p*, and Sn-4*d* states. Also, there are notable contributions from Sn-4*p* states. At higher energies, one can see contributions from Cu-4*s* states.

5.2. Sulfur K edge

The imaginary part of the macroscopic dielectric function of CZTS calculated with (brown solid line) and without (black solid line) *e-h* interactions by solving the BSE (see Section 3.4.2) is shown in Fig. 5.4. The transitions

from the 1*s* core state (K-edge) are dipole-allowed to *p*-states and *f*-states (if available). The IPA is proportional to the DOS, weighted by the momentum matrix elements between the core and conduction bands that reflect the *p*-character. The IPA spectra is characterized by a peak at 2471.90 eV which is followed by a broad peak at 2473.85 eV.

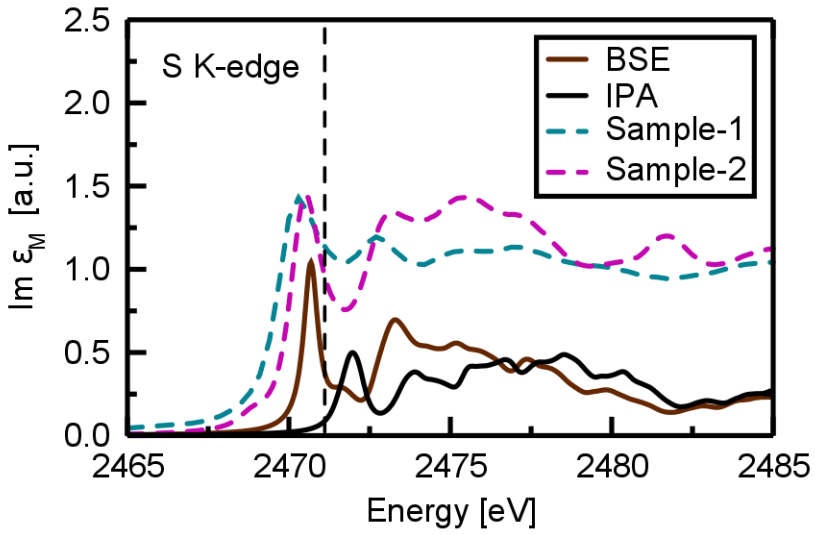

Figure 5.4.: Core-level absorption spectra from the sulfur K edge in Cu_2ZnSnS_4 in comparison with experiments. The brown line indicates the BSE result and the black line the IPA spectrum. The dashed lines indicate the experimental data, sample-1 (cyan) [57] and sample-2 (magenta) [58]. The dashed line represents the independent-particle onset. The calculated spectrum is shifted by 70.8 eV for comparison with experiments.

While the inclusion of *e-h* interaction red-shifts the absorption onset and redistributes the spectral weight with respect to the IPA, the main peaks are already visible in the IPA spectrum. Excitonic effects enhance the peak intensities at lower energies. The absorption onset at 2470.68 eV is attributed to a bound *e-h* pair with intense oscillator strength with a binding energy of 0.41 eV. Excitons with weak oscillator strength occur at 2473.45 eV, and the oscillator strengths decrease with increasing energies. Above 2476.45 eV, the IPA and BSE spectra exhibit similar features due to the weak *e-h* interaction.

The spectral features at 2470.68 and 2473.3 eV can be further analyzed by looking into the character of excitons that constitute the peaks. Figure 5.5 displays the excitonic weights (see Eq. 3.48) projected on top of the KS band structure together with the real-space representation of the excitons for the fixed hole position (see Eq. 3.46). From the band contributions, it can be observed that the onset peak at 2470.68 eV arises from excitations to the conduction bands up to 1.4 eV (Fig. 5.5(a)). Though the excitonic weights are distributed over the entire BZ most of the contributions come from the

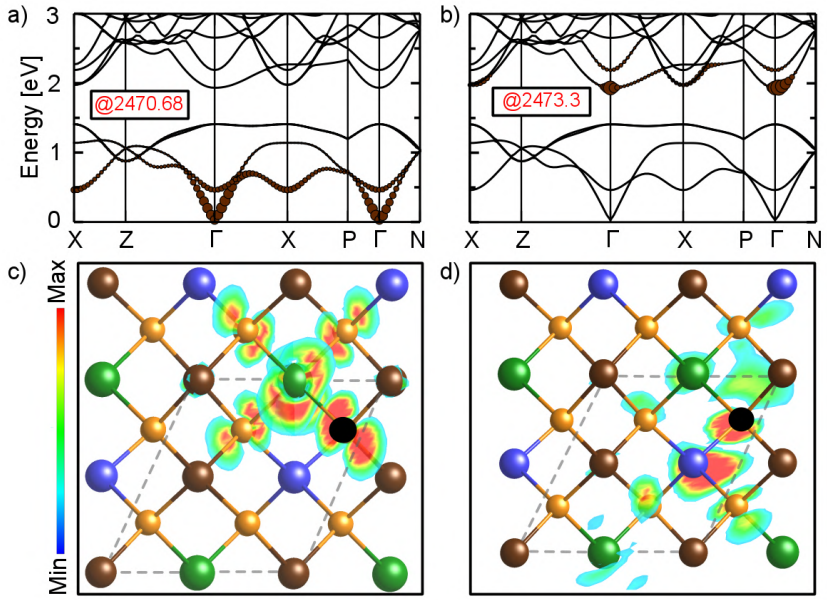

Figure 5.5.: Contribution of individual bands to the lowest-energy excitations (peaks at 2470.68 and 2473.3 eV). The size of the brown-colored circles quantifies the weight of the respective electronic state in the excitonic eigenstate. The bottom panel shows the real-space representation of the electron distribution. The position of the hole is marked by a black circle. Cu atoms are displayed in brown, Zn atoms in blue, Sn atoms in green, S atoms in orange.

Γ-point. The spectral feature at 2473.3 eV is formed by transitions to the conduction bands at 2 eV (Fig. 5.5(b)). As observed in the previous case, the excitonic weights are distributed over the entire BZ, and the dominant contributions come from the Γ point. The energy bands taking part in these excitations are dominated by contributions from S *p*-states (Fig. 5.3). The distribution of the excitonic weights in the reciprocal space reflects the localized character of the *e-h* wavefunction in real-space.

To further complement this analysis of the excitons, the distribution of the *e-h* wavefunctions in real-space for a fixed hole position (see Eq. 3.46) is displayed in Figs. 5.5(c) and (d). The exciton wavefunction corresponding to peak at 2470.68 eV (Fig. 5.5(c)) is not completely localized at the excited S atom but significantly reaches out to the neighboring Sn atoms and the S atoms surrounding it. The electron distribution corresponding to peak at 2473.3 eV (Fig. 5.5(d)) is found mainly between the S and Zn atom and spreads out to the nearest and the second-nearest S and Sn atoms.

For comparison with experimental data, the calculated spectra are shifted to 70.8 eV (Fig. 5.4). The IPA spectrum does not reproduce the spectral shape of the experimental data. The BSE spectrum exhibits the essential features in comparison with experiments, confirming the importance of including

e-h to describe the absorption spectra. Though the spectral features of the calculated and measured spectra are similar, they are far from satisfactory. However, there are also differences observed between the two measured spectra. These discrepancies will be discussed in Chapter 7.

5.3. Sulfur $L_{2,3}$ edge

In this section, a detailed description of excitations from the S $L_{2,3}$ edge is presented jointly with an in-depth analysis of the origin of the spectral features. The $L_{2,3}$ spectral lines illustrates transitions from $2p$ states to d and s states. For an accurate description, it is necessary to include spin-orbit splitting between the L_2 and L_3 edge. The S $2p_{3/2}$ (L_3 edge) and $2p_{1/2}$ (L_2 edge) core-states are separated by spin-orbit splitting of about 1.2 eV. Because of the small splitting, the transitions from S $2p_{3/2}$ and $2p_{1/2}$ initial states have to be considered simultaneously. The employed approach in this work allows us to treat spin-orbit coupling precisely (see Chapter 3).

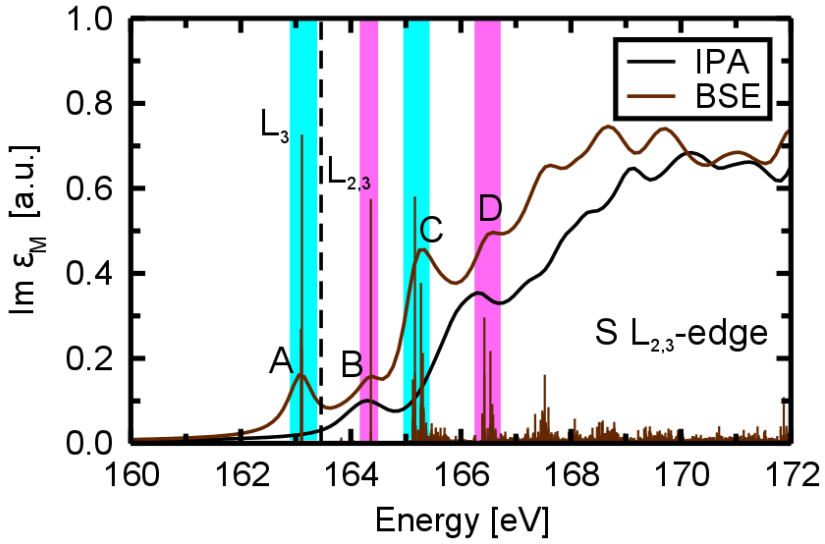

Figure 5.6.: Core-level absorption spectra from the S $L_{2,3}$ edge in Cu_2ZnSnS_4 (CZTS). The solid brown line shows the BSE result, and the solid black line shows the IPA spectrum. The oscillator strengths of the individual transitions are shown by the vertical bars, as obtained from the BSE calculations. The dashed line represents the IPA onset. The cyan vertical bars represent excitations from the L_3 edge, and the magenta vertical bars represent mixed transitions from the L_2 and L_3 channels.

The XANES from the S $L_{2,3}$-edge of CZTS is shown in Fig. 5.6 with (BSE) and without (IPA) *e-h* interaction. The IPA spectrum is characterized by a peak at 164.3 eV followed by another peak at 166.32 eV and a broad

spectral feature at 169.1 eV. The IPA spectral shape reflects the unoccupied S 3*d* states as well as their hybridization with Sn-5*s* and Cu 3*d*-states. The inclusion of *e-h* interaction in the BSE formalism red-shifts the absorption onset and redistributes the spectral weight with respect to the IPA. In BSE, the spectrum starts at 163.1 eV followed by a shoulder at 164.3 eV and a broad peak at 165.3 eV. The absorption onset is attributed to a bound exciton with binding energy of 0.34 eV.

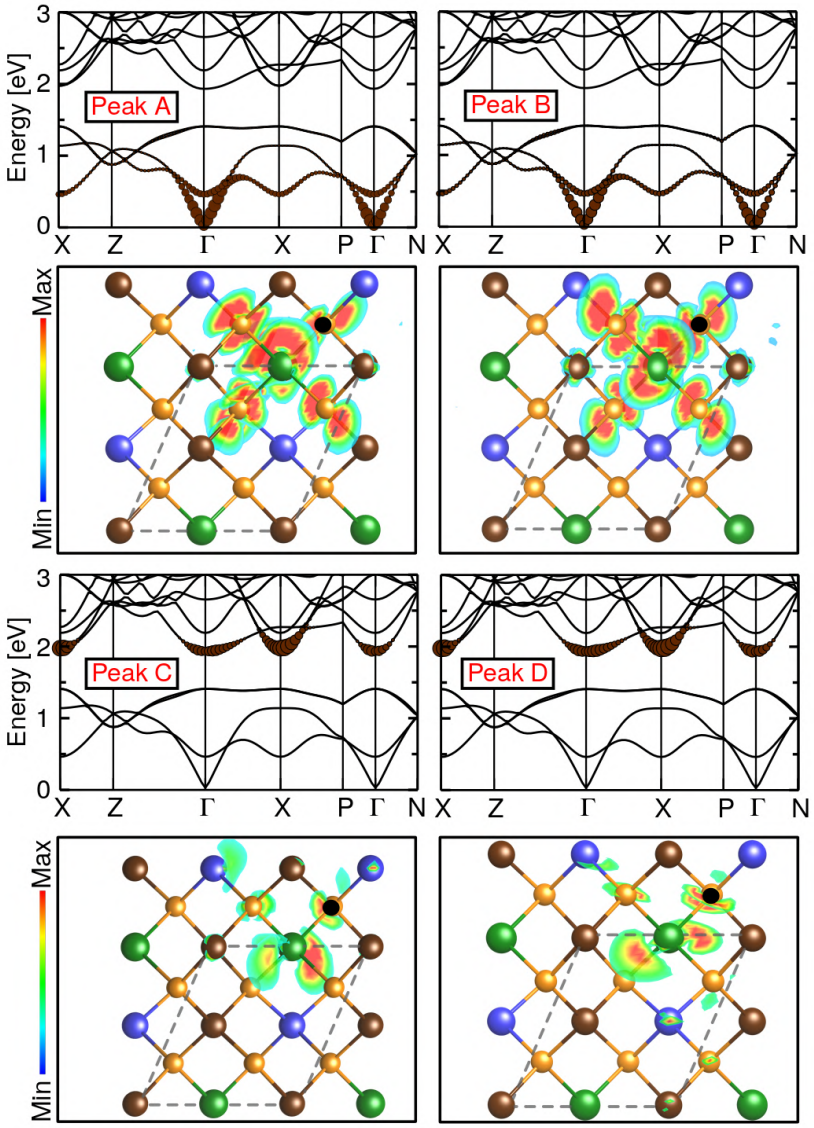

Figure 5.7.: Contribution of individual bands to the excitation of peaks A, B, C, and D marked in Fig. 5.6. The size of the brown-colored circles quantifies the weight of the respective electronic state in the excitonic eigenstate. Their respective bottom-panel shows the real-space representation of the electron distribution. In all cases, the position of the hole is marked by a black circle. Cu atoms are displayed in brown, Zn atoms in blue, Sn atoms in green, S atoms in orange.

The height of the brown vertical bars shows the oscillator strength of the excitons contributing to the corresponding peaks. The spectral features can be separated depending on the transitions that originate from L_2 and L_3 absorption edges, as well as by their mixing. The first peak is formed by excitations from the $2p_{3/2}$ level (L_3 edge). The second feature at 164.3 eV is formed by mixed transitions from the L_2 and L_3 channels. The peak at 165.3 eV originates again from excitations from the $2p_{3/2}$ core-state. Above 167 eV, a continuum of excitations with low intensity characterizes the spectrum.

To analyze the excitonic character corresponding to peaks A, B, C, and D marked in Fig. 5.6, the band contributions to these excitons are shown by projecting the excitonic weights onto the KS band structure in Fig. 5.7. The peaks A and B stem from transitions to the conduction bands up to 1.4 eV. Though the excitonic weights are distributed over the entire BZ, dominant contributions come from the region around the conduction band minimum. The peaks C and D arise from excitations to the conduction bands at 2 eV. As observed in the previous case, the excitonic weights are distributed over the entire BZ, and here the dominant contributions come from the $\Gamma - X$ path.

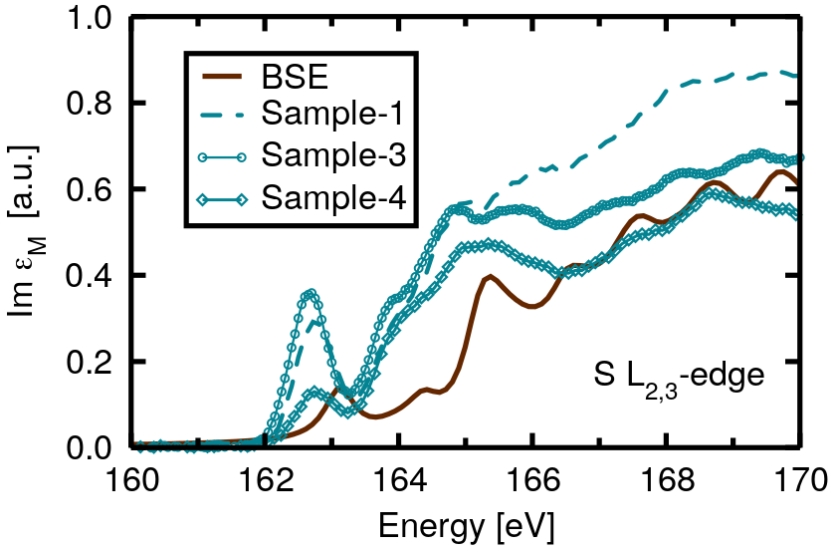

Figure 5.8.: S $L_{2,3}$-edge spectra of CZTS in comparison with experiment. The calculated spectra is shifted by 12.8 eV and a Lorentzian broadening of 150 meV is applied. The cyan lines indicates measured data of three samples (sample-1 [57], sample-3 [59], and sample-4 [57]).

To complement this analysis, Fig. 5.7 also displays the distribution of the *e-h* wavefunction in real-space (see Eq. 3.46). The exciton wavefunctions corresponding to peaks A and B are similar. They are not fully localized at the excited S atom but extend to the neighboring Sn atom and the surrounding S atoms. Likewise, the exciton wavefunctions corresponding to peak

C and D are similar to each other. They are not localized at the S atom but also spread out to the nearest Sn and Zn atoms and second-nearest S and Zn atoms.

In Fig. 5.8, comparison of the calculated BSE spectra with experimental spectra is shown. The calculated spectrum is shifted by 12.8 eV. The absorption onset of all three measured samples appears at 162.7 eV followed by a shoulder at 163.8 eV and a peak at 164.9 eV. Like in the case of the S K-edge (Fig. 5.4), the comparison of the calculated and measured spectra reveals some discrepancies. The origin of these discrepancies will be discussed in detail in Chapter 7.

5.4. Summary

In this chapter, a detailed analysis of the electronic structure and excitations from the S K and the $L_{2,3}$ edge in CZTS has been presented. The inclusion of the attractive Coulomb interaction red-shifts the absorption onset leading to the formation of bound excitons with binding energies of 0.41 eV and 0.34 eV for K-edge and $L_{2,3}$-edge, respectively. The lowest spectral features are formed from excitations into the low-lying conduction bands in both S edges. However, the excitation from the K-edge probes the *p* like states whereas the $L_{2,3}$ edge probe *s* and *d* like states. The more intense spectral features of the K-edge spectra in comparison with $L_{2,3}$ edge reflects the dominant *p* character to the conduction states. Detailed analysis of the character of the first and second feature reveals that the exciton distribution for the first peak is along the Sn-S bond. In the second peak, the excitons are distributed along the Zn-S bond in both edges. For both edges, there are discrepancies between the calculated and the measured spectra. In the upcoming chapter, a comparison with the binary phases ZnS and SnS_2 will be presented to understand whether these discrepancies can be related to binary phases that may be present in the measured material.

The focus of this chapter is to present XANES of the sulfur K- and $L_{2,3}$-edge in the binary phases ZnS and SnS_2 to understand the discrepancies between the calculated and the measured CZTS spectra discussed in the previous chapter.

6.1. SnS_2

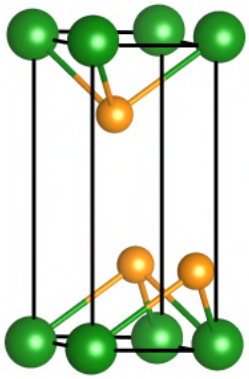

Figure 6.1.: Conventional unit cell of SnS_2. Sn atoms are in blue, and S atoms in orange.

SnS_2 naturally occurs as a mineral berndtite. SnS_2 crystallizes in the hexagonal closely-packed structure with space group $P3m1$ symmetry. The crystal structure of SnS_2 is displayed in Fig. 6.1. The crystal has a layered structure, where each Sn atom is octahedrally surrounded by six S atoms. The structure optimization yields the lattice parameter $a = 3.75$ Å which is in good agreement with experiment [60].

6.1.1. Electronic Structure

The analysis of the electronic properties is important as the x-ray absorption spectra strongly depend on the local electronic structure of the absorbing atom. The electronic structure calculations were performed starting from the optimized structure on the GGA-PBE level. For more computational details, see Chapter 4. The BZ of the hexagonal close-packed lattice structure and the location of the high symmetry points used to calculate the band structure is displayed in Fig. 6.2 (top-panel). The calculated bandstructure and the PDOS are shown for the energy region between -4 to 8 eV in Fig.

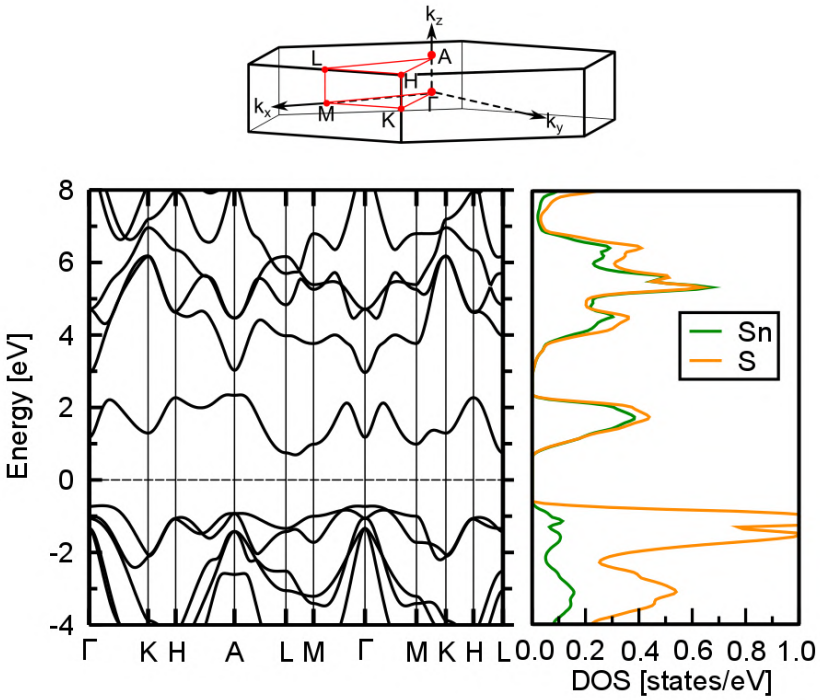

Figure 6.2.: a) Brilloiun zone (BZ) of SnS_2 showing the location of the high-symmetry points. b) Band structure and partial density of states (PDOS) of SnS_2 for the energy region between -4 and 8 eV.

6.2 (bottom-panel). SnS_2 crystals have a indirect bandgap. The VBM is at the Γ-point and the CBM is between *L* and *M* points. This shows that SnS_2 has an indirect bandgap. The computed KS band gap is 1.91 eV. From the PDOS (right-panel), one can see that the major contributions to the valence bands are from S states, whereas conduction bands are dominated by contributions from both Sn and S states. These results are in good agreement with previously reported calculations of the electronic structure [61].

To understand the final states of the absorption spectra, the focus of this section lies on the conduction band region of the band structure. Figure 6.3 displays the atomic characters projected on the conduction band structure. The majority of the contributions to the first conduction bands up to 2.3 eV are from Sn-5*s* and S-3*p* states. The bands in the energy range between 3 to 7 eV are dominated by contributions from Sn-5*p* and S-3*p* states with minor contribution from S-3*d* states. At higher energies, there are contributions from Sn-4*d* and S-3*d* states.

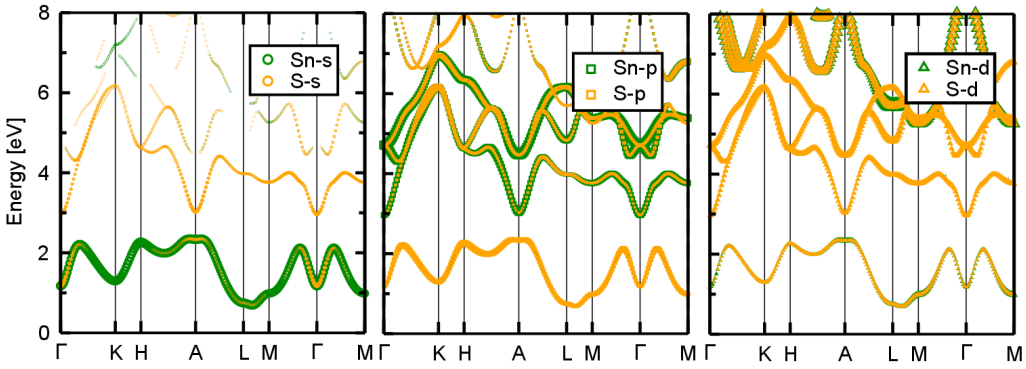

Figure 6.3.: Atomic *s* (left), *p* (middle), and *d* (right) characters projected on the bandstructure of SnS_2 in the conduction band region. The color code indicates contributions from Sn (green) and S (orange). The size of the symbols quantifies the weight of *s*, *p*, and *d* characters displayed in the three panels.

6.1.2. Sulfur K edge

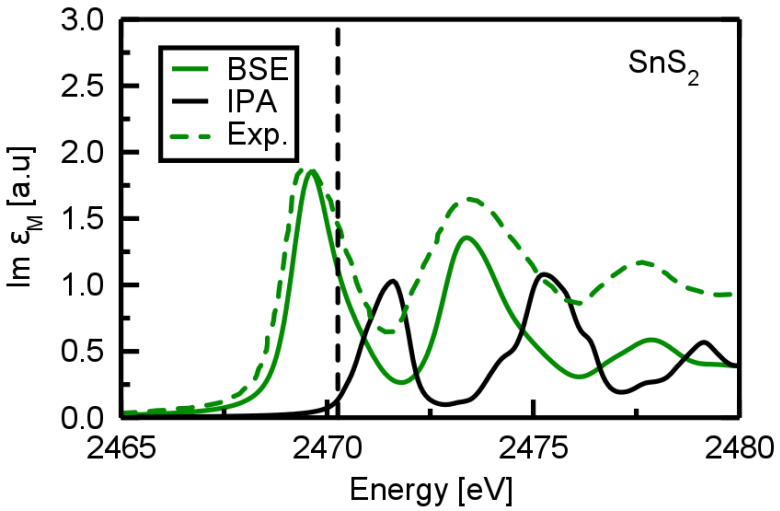

Figure 6.4.: Core-level absorption spectra of the sulfur K-edge in SnS_2. The green-solid line indicates the BSE result of SnS_2 and the black-solid line indicates independent-particle (IPA) spectrum. The dashed green line indicate the experimental data [58]. The dashed vertical line represents the independent-particle onset. The calculated spectrum is shifted by 74.9 eV for comparison with experiments.

The imaginary part of the microscopic dielectric function of SnS_2 calculated with (green-solid line) and without (black-solid line) *e-h* interaction by solving the BSE is shown in Fig. 6.4. The IPA is proportional to the DOS, weighed by the momentum matrix elements between the core and conduction bands that reflects *p*-character. The IPA spectrum is characterized by two sharp peaks at 2471.63 and 2475.31 eV, followed by another peak at 2479.22 eV. The inclusion of *e-h* interaction red-shifts the absorption onset

and redistributes the spectral weight with respect to IPA. Excitonic effects enhance the peak intensities at lower energies. In BSE (solid green line), the absorption onset at 2470.65 eV is attributed to a bound *e-h* pair with intense oscillator strength with a binding energy of 0.89 eV. Excitons with weak oscillator strength occur at 2473.44 eV, and the oscillator strengths decrease with increasing energies. The calculated spectra is in excellent agreement with the experimental data [58].

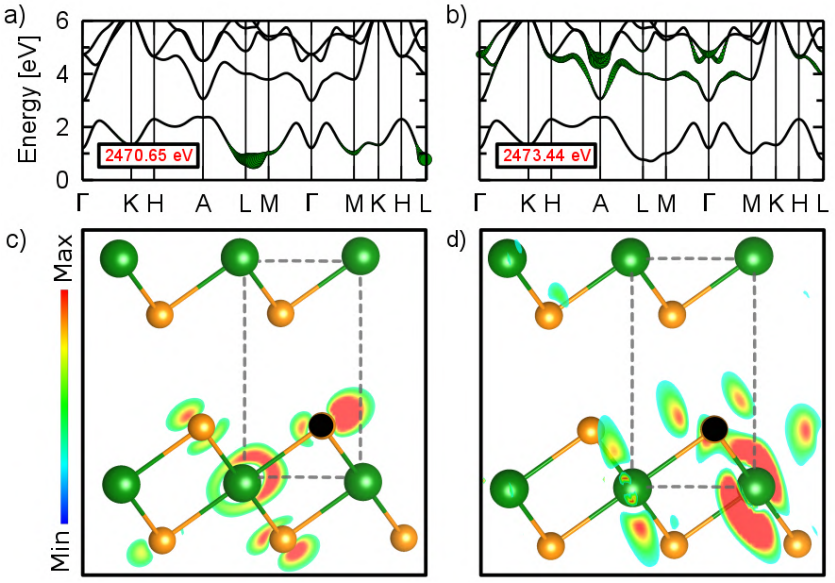

Figure 6.5.: Contribution of individual bands to the lowest-energy excitations at 2470.65 and 2473.44 eV (Fig. 6.4). The size of the green-colored circles quantifies the weight of the respective electronic state in the excitonic eigenstate. The bottom panel displays the real-space representation of the electron distribution. The fixed hole position is marked by a black circle. Sn atoms are displayed in green and S atoms in orange.

The spectral features at 2470.65 and 2473.44 eV can be further analyzed by looking into the character of the excitons that make up the peaks. The excitonic weights (see Eq. 3.48) projected on top of the KS band structure together with the real-space representation of the excitons for the fixed hole position (see Eq. 3.46) is shown in Fig. 6.5. From the band contributions, it can be observed that the onset peak at 2470.65 eV arises from excitations to the conduction band up to 1.4 eV (Fig. 6.5(a)). Though the excitonic weights are distributed over the entire BZ, most of the contributions come from L and M points. The spectral feature at 2473.44 eV is formed by transitions to the conduction bands between 3 to 5 eV (Fig. 6.5(b)). As observed in the previous case, the excitonic weights are distributed over the entire BZ, and the dominant contributions come from the A-point. The energy bands taking part in these excitations are dominated by contributions from S *p*- and Sn *p*-states (Fig. 6.3). The distribution of the excitonic weights in reciprocal space reflects the localized character of the e-h wavefunction in

real-space.

To further complement this analysis, the distribution of the *e-h* wavefunction in real-space for a fixed hole position is displayed in Figs. 6.5(c) and (d). The exciton wavefunction corresponding to peak at 2470.65 eV (Fig. 6.5(c)) is not completely localized at the excited S atom but significantly reaches out to the neighboring Sn atoms and the S atoms surrounding it. The electron distribution corresponding to peak at 2473.44 eV (Fig. 6.5(d)) is found mainly between the excited S atom and the neighboring Sn atoms.

6.1.3. Sulfur $L_{2,3}$ edge

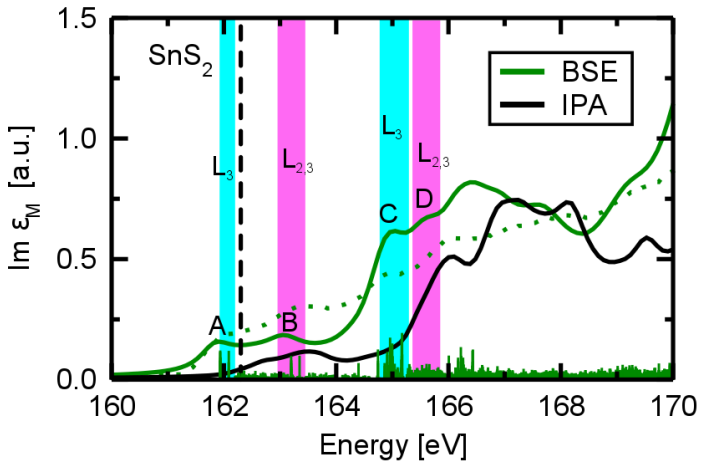

Figure 6.6.: Core-level absorption spectra from the S $L_{2,3}$ edge in SnS_2. The green-solid line shows the BSE result, and the black-solid line shows the IPA spectrum. The dashed green line indicate experimental data [59]. The calculated spectrum is shifted by 12.0 eV for comparison with experiments. The oscillator strength of the individual transitions is shown by the vertical bars, as obtained from the BSE calculations. The dashed line represents the IPA onset. The cyan vertical bar represent excitations from the L_3 edge, and the magenta vertical bars represent mixed transitions from the L_2 and L_3 channels.

The XANES from the S $L_{2,3}$-edge of SnS_2 is shown in Fig. 6.6 with (BSE) and without (IPA) *e-h* interaction. The IPA spectrum is characterized by a broad peak at 161.8 eV followed by the peak at 163.1 eV and another peak at 164.9 eV. The IPA spectral shape reflects the unoccupied S -3*d* and Sn-5*s* states. The inclusion of *e-h* interaction in the BSE formalism red-shifts the absorption onset and redsitributes the spectral weight with respect to the IPA. In BSE, the spectrum starts at 161.8 eV followed by another peak at 163.1 eV and a broad peak at 164.9 eV. The absorption onsent is attributed to a bound exciton with a binding energy of 0.24 eV.

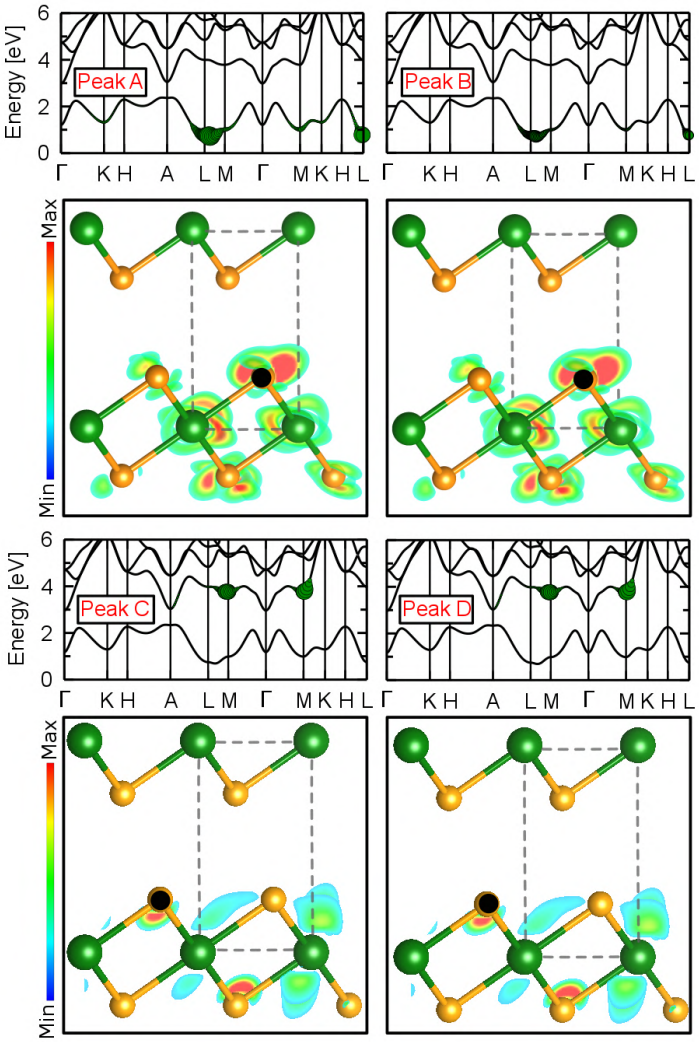

Figure 6.7.: Contributions of individual bands to the peaks at A, B, C, and D marked in Fig. 6.6. The size of the green- colored circles quantifies the weight of the respective electronic state in the excitonic eigenstate. Their respective bottom panel displays the real-space representation of the electron distribution. In all cases, the position of the hole is marked by a black circle. Sn atoms are displayed in green and S in orange.

The green vertical bars show the oscillator strength of the excitons contributing to the corresponding peaks. The spectral features can be separated depending on the transition from L_2 and L_3 absorption edges, as well as by their mixing their mixing. The first peak is formed by transitions from the $2p_{3/2}$ state (L_3 edge). The feature at 163.1 eV is formed by mixed transitions from the L_2 and L_3 channels. The peak at 164.9 eV again originates from excitations from the $2p_{3/2}$ core-state. Above 166 eV, a continuum of excitations with low intensity characterizes the spectrum. The calculated spectra is in good agreement with the experimental data [59].

To analyze the excitonic character corresponding to peaks A, B, C, and D marked in Fig. 6.6, the band contributions to these excitons are shown in Fig. 6.7 by projecting the excitonic weights onto the KS band structure. The peaks A and B arise from excitations to the conduction band up to 1.4 eV. The dominant contributions of the excitonic weights come from the region around the conduction band minimum. The peaks C and D stem from excitations to the conduction bands at 3 eV. The dominant contributions of the excitonic weights come from M point.

To complement this analysis, Fig. 6.7 also displays the distribution of the *e-h* wavefunction in real-space for a fixed hole position. The exciton wavefunctions corresponding to peaks A and B are similar. The exciton wavefunctions are not fully localized at the excited S atom but extend to the neighboring Sn atoms and S atoms surrounding it. Likewise, the exciton wavefunctions corresponding to peaks C and D are similar to each other. They are not localized at the excited S atom but also spread out to the nearest Sn and S atoms.

6.2. ZnS

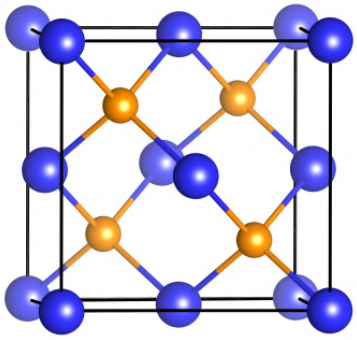

Figure 6.8.: Conventional unit cell of ZnS. Zn atoms are in blue, and S atoms in orange.

ZnS occurs in two types of crystal structures, zincblende or sphalerite and wurtzite. Zincblende has a face-centered cubic lattice with space group $F\bar{4}3m$, whereas wurtzite has a hexagonal closet packed lattice with space group $P6_3mc$ symmetry. In this work, the focus lies on zincblende ZnS. The crystal structure of ZnS is shown in Fig. 6.8, where the sulfur anions occupy the face-centered cubic lattice sites, and zinc cations are present in the tetrahedral voids. As a first step to obtaining absorption spectra starting from the experimental lattice parameters, structure optimization is performed. The structures optimization yields the lattice parameter $a = 5.36$ Å which in good agreement with experiment [62].

6.2.1. Electronic structure

In Fig. 6.9(a), the BZ of the face-centered cubic lattice structure and the location of the high-symmetry points used to calculate the band structure is displayed. The band structure and the partial density of states (PDOS) calculated on the GGA-PBE level is shown for the energy region between -4 and 8 eV in Fig. 1.2(b). The bands around the bandgap are strongly dispersive. ZnS has a direct bandgap at the Γ-point. The computed KS gap is 2.23 eV. The bands at higher energies above 4 eV are strongly dispersive. From the PDOS (right-panel), one can see that the major contributions to bands between the energy range -4 to 4 eV are from Zn and S. The conduction bands at higher energy between 4 to 7 eV are dominated by contributions from Zn states.

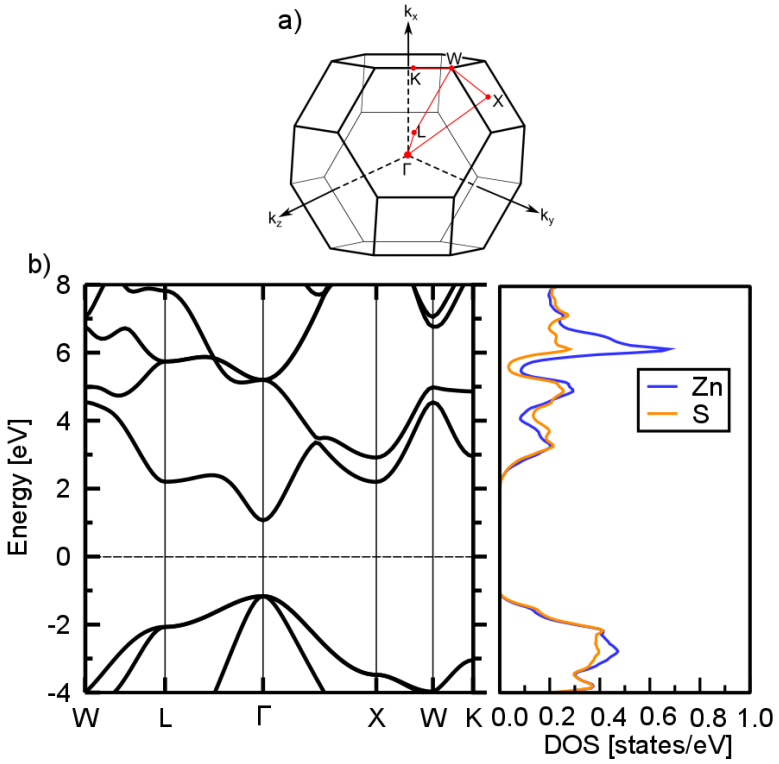

Figure 6.9.: a) Brilloiun zone (BZ) of ZnS showing the locations of the high-symmetry points. c) Band structure of ZnS and projected density of states for the energy region between -4 and 8 eV.

The atomic characters projected on the conduction band structure of ZnS are shown in Fig. 6.9. The conduction bands in the energy range 1.0 to 4.5 eV are dominated by contributions from Zn-4*s*, S-3*s*, and Zn-3*d* states. At higher energies above 5.2 eV are dominated by contributions from S-3*p* and Zn-3*p* states. Also, there are notable contributions from Zn-3*d* states.

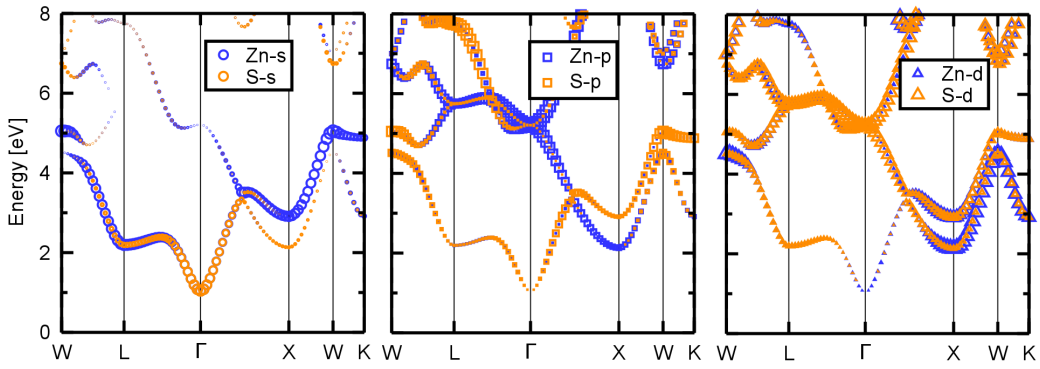

Figure 6.10.: Atomic *s* (left), *p* (middle), and *d* (right) characters projected on the bandstructure of ZnS in the conduction band region. The color code indicates contributions from Zn (blue) and S (orange). The size of the symbols quantifies the weight of *s*, *p*, and *d* characters displayed in the three panels.

6.2.2. Sulfur K edge

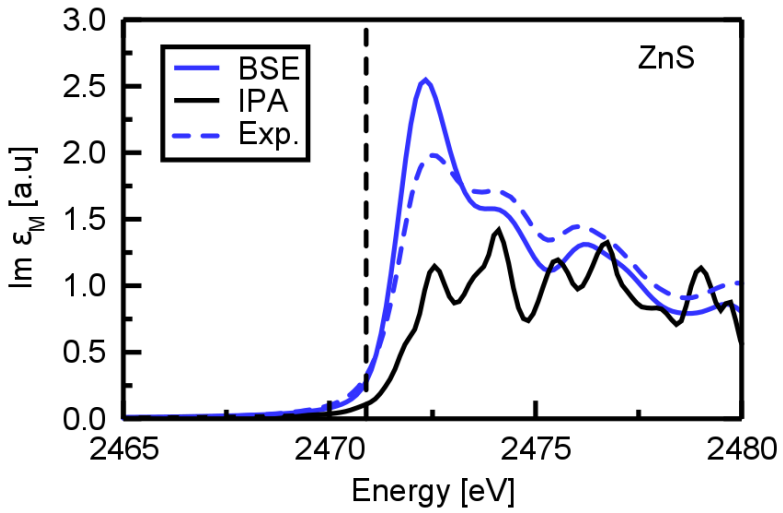

Figure 6.11.: Core-level absorption spectra of the sulfur K edge in ZnS. The blue-solid line indicates the BSE result of ZnS and the black-solid line indicates independent-particle (IPA) spectrum. The dashed blue line indicate the experimental data [58]. The dashed vertical line represents the independent-particle onset. The calculated spectrum is shifted by 75.2 eV for comparison with experiments.

The imaginary part of the microscopic dielectric function of ZnS calculated with (blue solid line) and without (black solid line) *e-h* interaction by solving the BSE is shown in Fig. 6.11. The IPA spectra are characterized by a double peak at 2472.54 eV and 2474.13 eV followed by another double peak feature at 2475.58 eV and 2476.72 eV. The inclusion of *e-h* interaction red-shifts the absorption onset and redistributes the spectral weight with respect to IPA.

In BSE (blue solid line), the absorption onset is at 2474.34 eV with intense oscillator strength followed by a broad peak at 2476.25 eV.

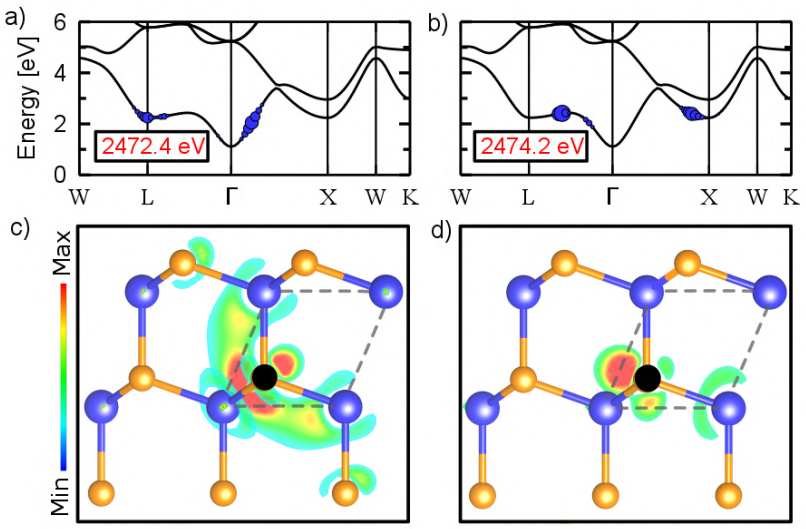

Figure 6.12.: Contribution of individual bands to the lowest-energy excitation peaks at 2472.4 and 2474.2 eV in Fig. 6.11. The size of the blue-colored circles quantifies the weight of the respective electronic state in the excitonic eigenstate. The bottom panel displays the real-space representation of the electron distribution. The position of the hole is marked by a black circle. Zn atoms are displayed in blue, and S atoms in orange.

The spectral features at 2472.4 and 2474.2 eV can be further analyzed by looking into the character of excitons that constitute the peaks. Figure 6.12 displays the excitonic weights projected on top of the KS band structure, together with the real-space representation of the excitons. From the band contributions, it can be observed that the peak at 2472.4 eV stems from transitions to the conduction band up to 4.5 eV (Fig. 6.12(a)). Most of the exciton weights are observed close to the points L and Γ. Like in the previous case, the spectral features at 2474.2 eV also arise from excitations to the conduction band up to 4.5 eV (Fig. 6.12(b)). The majority of the exciton weights is observed between the L and Γ points and close to the X point. The bands taking part in these excitations are dominated by contributions from S *p* states.

To complement this analysis, the distribution of the *e-h* wavefunction in real-space is displayed in Fig. 6.12(c) and (d). The exciton wavefunction corresponding to peak at 2472.4 eV (Fig. 6.12(c)) is not completely localized at the excited S atom but also reaches out to the Zn atoms surrounding it. The electron distribution corresponding to peak at 2474.2 eV (Fig. 6.12(d)) is found mainly between the excited S and Zn atom.

6.2.3. Sulfur $L_{2,3}$ edge

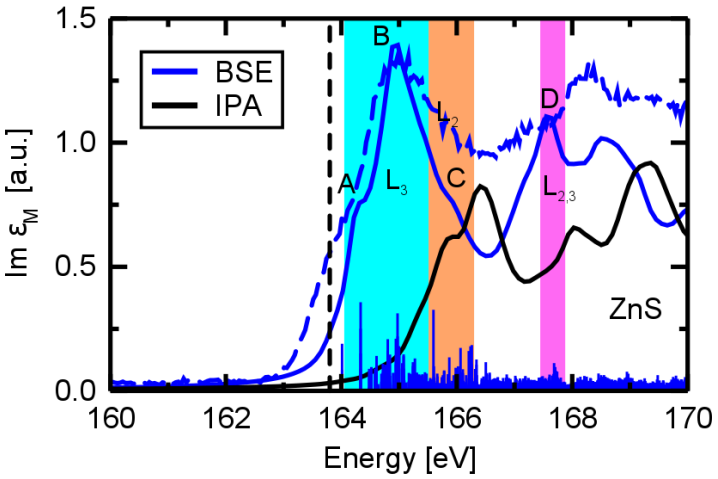

Figure 6.13.: Core-level absorption spectra from the S $L_{2,3}$ edge in ZnS. The solid blue line shows the BSE result, and the solid black line shows the IPA spectrum. The dashed green line indicate experimental data [59]. The calculated spectrum is shifted by 12.8 eV for the comparison with experiments. The oscillator strength of the individual transitions is shown by the vertical bars, as obtained from the BSE calculations. The dashed line represent the IPA onset. The cyan vertical bars represent the excitations from the L_3 edge, the orange vertical bars represent excitations from the L_2 edge, and the magenta vertical bars represent mixed transitions from the L_2 and L_3 channels.

The XANES from the S $L_{2,3}$-edge of ZnS is shown in Fig. 6.13 with (BSE) and without (IPA) *e-h* interaction. In the IPA spectrum, peak starts at 164.9 eV, followed by a second peak at 167.6 eV. The inclusion of *e-h* red-shifts the absorption onset and redistributes the spectral weight. The BSE spectrum is characterized by a shoulder peak at 164.2 eV, followed by a peak at 164.9 eV and again a shoulder at 165.52 eV.

The height of the blue vertical bars shows the oscillator strength of the excitons contributing to the corresponding peaks. The spectral features can be separated depending on the transitions from L_2 and L_3 absorption edges and their mixing. The first shoulder and the peak is formed by transitions from $2p_{3/2}$ level (L_3 edge). The second shoulder (165.52 eV) is formed by excitations from the $2p_{1/2}$ level (L_2 edge). The peak at 165.99 eV is formed by mixed transitions from the L_2 and L_3 channels. Above 166 eV, a continuum of excitations with low intensity characterizes the spectrum.

To analyze the excitonic character corresponding to peak A, B, C, and D the band contributions to these excitons are shown in Fig. 6.14 by projecting the excitonic weights onto the KS band structure. From the band contribution, it can be observed that the spectral features arise from transitions to the first

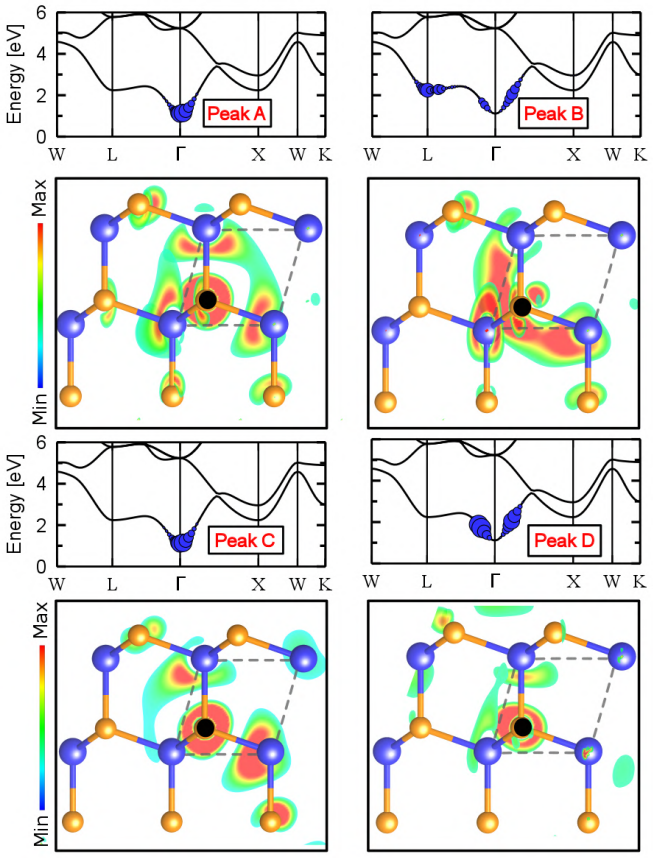

Figure 6.14.: Contribution of individual bands to the excitations of peaks A, B, C, and D marked in Fig. 6.13. The size of the blue-colored circles quantifies the weight of the respective electronic state in the excitonic eigenstate. Their respective bottom panel shows the real-space representation of the electron distribution. In all cases, the position of the hole is marked by a black circle. Zn atoms are displayed in blue and S atoms in orange.

conduction band. For peaks A and C, the dominant contributions come from the Γ point. In case of peaks B and D, the dominant contributions come between the points L, γ, and X. To complement this analysis, Fig. 6.14 also displays the distribution of *e-h* wavefunction in real-space. The exciton wavefunctions corresponding to all the peaks are similar. In all cases, they are not fully localized at the excited S atom but also extend to the surrounding Zn atoms and second-nearest S atoms.

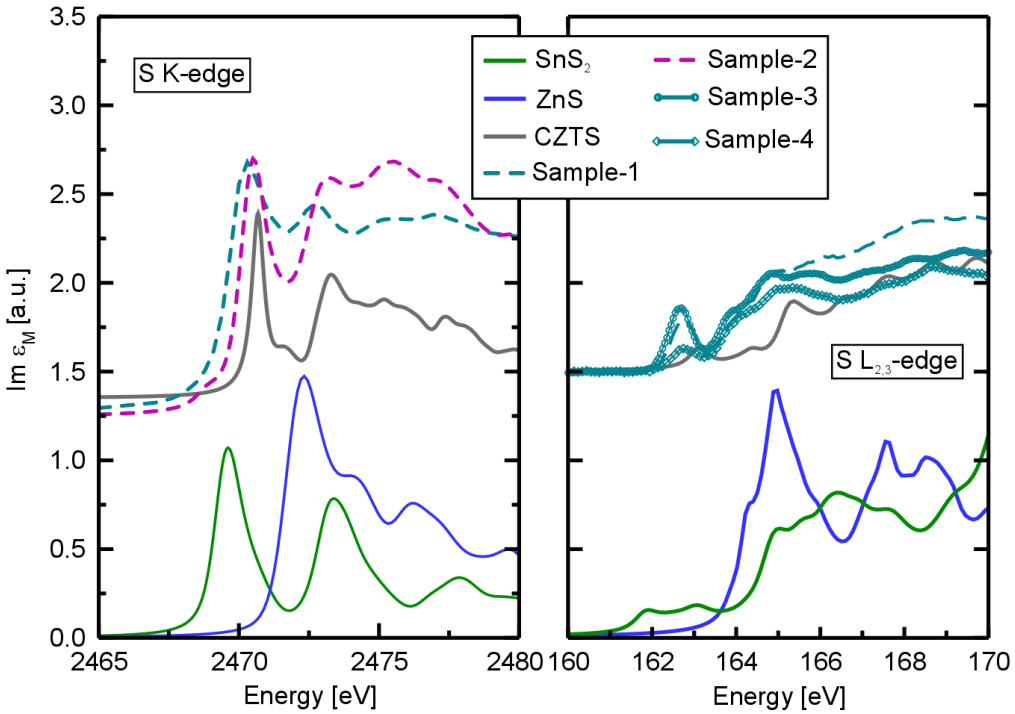

Figure 6.15.: Core-level absorption spectra of the sulfur K (left panel) and $L_{2,3}$ (right panel) edge in the binary phases SnS_2 (green solid lines) and ZnS (blue solid lines). For comparison, the calculated and measured spectra of core-level spectra of CZTS (see Chapter 5) ares shown.

6.3. Comparison of CZTS and their binary phases with experiment

In this section, the discrepancies between the calculated and measured spectra of CZTS discussed in Chapter 5 are addressed in comparison with the binary phases ZnS and SnS_2. In Fig. 6.15, the calculated sulfur K (left) and $L_{2,3}$ (right) edge spectra of SnS_2 and ZnS as described in Sections. **??** and **??** are shown together with the calculated and measured spectra of CZTS. For a detailed description of the latter, see Chapter 5. Like in CZTS, a bound exciton is observed in both the edges in SnS_2 but not in ZnS. The peak structure in the K edge in CZTS from 2468.5 to 2471.98 eV resembles SnS_2 whereas, above 2472 eV, the spectral features resemble ZnS. The spectral features may be the same, while the positions are not. This is attributed to the difference in the bandgap of the three materials. It is also clear from the analysis of the character of excitons constituting the former peak reveals that the probability of excitation is strong in the excited S atom and extends to neighboring Sn atom (see Fig. 5.5 (c)). Likewise, for the latter peak, the

probability of excitation is between S and Zn atom (see Fig. 5.5 (d)).

The right panel of Fig. 6.15 displays the calculated S $L_{2,3}$ edge of SnS_2 and ZnS together with CZTS. As mentioned before, the K and $L_{2,3}$ edge differ due to their different selection rules. The transitions from $L_{2,3}$ reflect *s* and *d* character. In comparison with CZTS, it can be observed that the peak structures from 162.6 to 164.5 eV resemble those of SnS_2. Above 165.5 eV, the spectral features are similar to ZnS. As observed in K edge, from the analysis of the character of excitons constituting the peaks between 162.6 and 164.5 eV reveals that the probability of excitation is strong in the excited S atom and extends to neighboring Sn atom (see Fig. 5.7 (top panel)). Similarly, for the latter peak, the probability of excitation is between S and Zn atom (see Fig. 5.7 (bottom panel)).

Overall in both edges, though the spectral features of the calculated and measured spectra are similar, this does not solve the discrepancies observed between the calculated and measured spectra of CZTS.

6.4. Summary

In this chapter, a detailed analysis of the electronic structure and excitations from the S K and $L_{2,3}$ edge in the binary phases SnS_2 and ZnS has been presented. The inclusion of the attractive Coulomb interaction red-shifts the absorption onset, and the spectral weights are significantly redistributed in both SnS_2 and ZnS. A bound excitonic state is observed in SnS_2 but not in ZnS. The more intense spectral features of the K-edge spectra in comparison with $L_{2,3}$ edge reflects the dominant *p* character to the conduction states. The calculated and measured spectra are in excellent agreement in both edges. In comparison with CZTS, the lowest spectral features resemble those of SnS_2, and the spectral features at higher energy resemble those of ZnS.

Though the origin of the spectral features can be understood, the discrepancies between the calculated and measured spectra in CZTS remain an open issue. To understand the origin of these differences, the studies are extended to defect complexes, which will be discussed in the next chapter.

As mentioned before, the nature of the CZTS compound point defects are formed, affecting the physical properties of the material. Defect complexes are formed when point defects with opposite charges are close to each other. Among the possible reported defect complexes, pairs like Cu_{Zn}+Zn_{Cu} and V_{Cu}+Cu_{Zn} have lower formation energy (see Section 2.3). In this chapter, a detailed analysis of the defect complexes Cu_{Zn}+Zn_{Cu} and V_{Cu}+Zn_{Cu} is presented by examining core excitations from the sulfur K- and $L_{2,3}$-edges.

7.1. Cu_{Zn}+Zn_{Cu} in CZTS

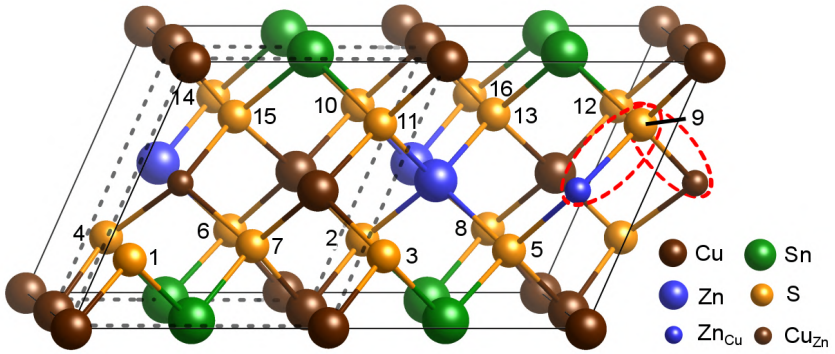

Figure 7.1.: Atomic configuration of the defect complex Cu_{Zn}+Zn_{Cu} in CZTS. The acceptor (Cu_{Zn}) and donor (Zn_{Cu}) defects are placed closely to each other to form a complex (red oval lines). The inequivalent sulfur sites are labeled with their index n_S. The unit cell of single-phase CZTS is highlighted with the dashed line.

The atomic configuration of the defect complex Cu_{Zn}+Zn_{Cu} is shown in Fig. 7.1 as described by a $2 \times 2 \times 1$ supercell with 32 atoms. The point defects Cu_{Zn} and Zn_{Cu} are placed close to each other to form a defect complex marked by a dashed red oval lines. The low symmetry makes the sulfur atoms inequivalent which is marked with their index n_S. Starting from the experimental lattice parameters of pristine CZTS, the atomic coordinates are relaxed until residual forces per atom are smaller than 0.05 eV/Å. For ease of discussion, the acronym Cu_{Zn}+Zn_{Cu} is used to denote the material.

7.1.1. Electronic Structure

In Fig. 7.2(a) the BZ of the triclinic lattice structure and the location of the high-symmetry points used to calculate the band structure are shown.

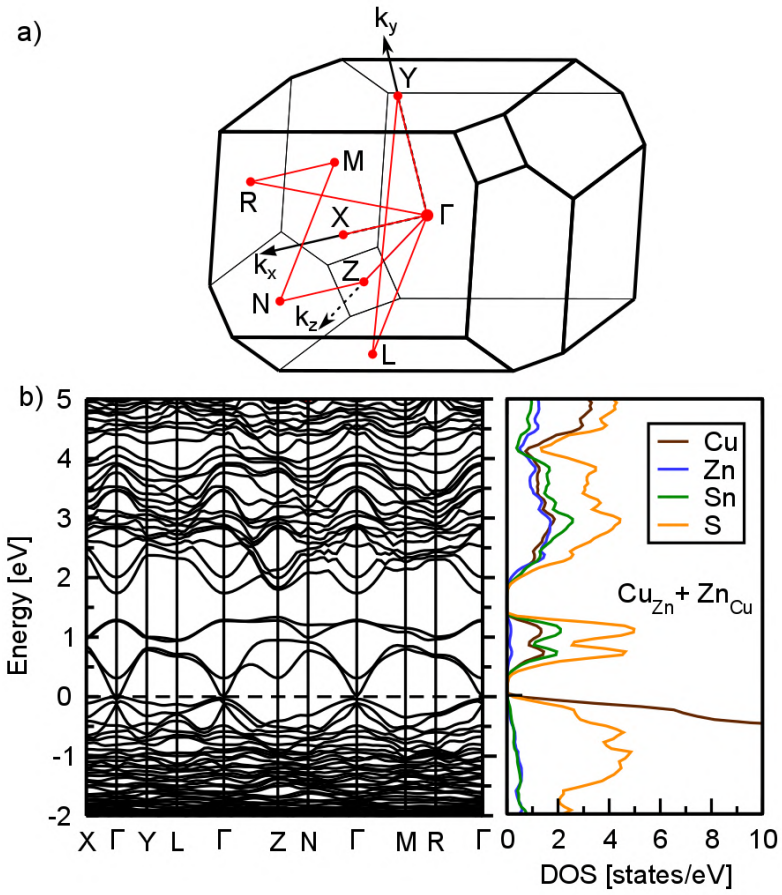

Figure 7.2.: a) Brilloiun zone (BZ) of CZTS with the defect complex Cu_{Zn}+Zn_{Cu} showing the location of high-symmetric points. b) Band structure and PDOS for the energy region between -2 and 5 eV.

The band structure and the PDOS calculated on the GGA-PBE level is shown in Fig. 7.2(b). The bands around the bandgap region are strongly dispersive. Cu_{Zn}+Zn_{Cu} exhibits a direct bandgap of 0.04 eV at the Γ point. In comparison with pristine CZTS (see Sec. 5.1), the bandgap is decreased by 0.09 eV. The PDOS of the pristine material and Cu_{Zn}+Zn_{Cu} are similar.

It is essential to look into the unoccupied region to understand the final states of the absorption spectra. In Fig. 7.3, the atomic-orbital characters projected on the conduction band region are shown. Overall, the atomic contributions to the conduction band region of the pristine CZTS (see Fig. 5.3) and Cu_{Zn}+Zn_{Cu} are very similar . Most contributions to low-lying conduction bands up to 1.5 eV are from Sn- 5*s* and S-3*p* states with minor contributions from Cu-3*d* states. The conduction bands in the energy range between 2.2 to 4 eV are dominated by contributions from Zn-4*s*, S-3*p*, and Sn-4*d* states. Also, there are notable contributions from Sn-4*p* states. At higher energies, one can see contributions from Cu-4*s* states.

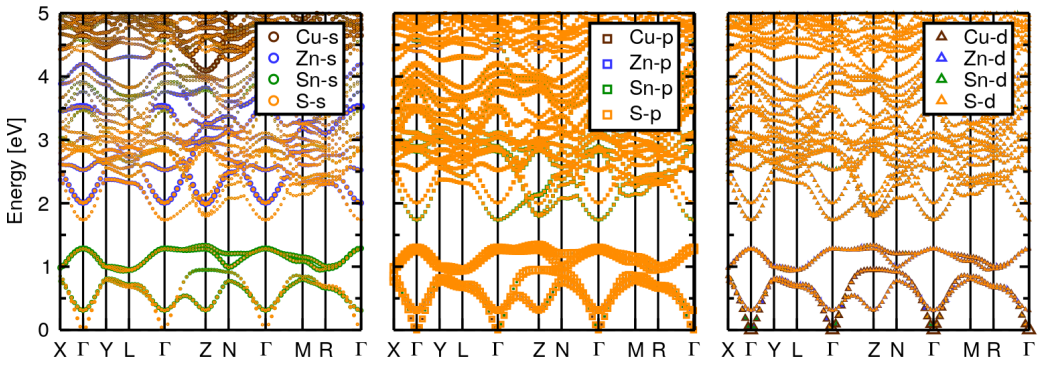

Figure 7.3.: Atomic-orbital *s* (left), *p* (middle), and *d* (right) characters projected on the band structure of Cu_{Zn} + Zn_{Cu} in the conduction band region. The color code indicates contributions from Cu (brown), Zn (blue), Sn (green), and S (orange). The size of the symbols quantifies the weight of *s*, *p*, and *d* character.

7.1.2. Sulfur K edge

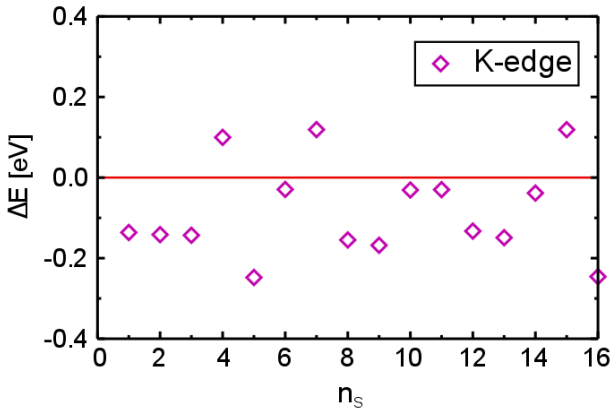

Figure 7.4.: Core-level shifts (ΔE) of the S 1*s* states for the inequivalent sulfur atoms, marked in Fig. 7.1 with respect to that of single phase CZTS. The shifts are calculated by taking the VBM as reference.

In this section, the absorption spectra of the sulfur K-edge of the defect complex Cu_{Zn}+Zn_{Cu} in CZTS are presented. They are calculated for the inequivalent sulfur atoms of Cu_{Zn}+Zn_{Cu} labeled in the supercell (Fig. 7.1). For this purpose, it is important to understand the relative core levels shift (ΔE) upon defect formation since they are sensitive to the chemical environment. The ΔE for the inequivalent sulfur atoms is shown in Fig. 7.4. The atomic species S4, S7, and S15 are close to the acceptor point defect Cu_{Zn}. Their energetic positions are up-shifted by +0.14 eV. The species S5 and S16 are close to the donor point defect Zn_{Cu}. Their energetic positions are down-shifted by -0.25 eV. The species S9 is shared by both the point defects Cu_{Zn} and Zn_{Cu}. Its energetic position is down-shifted by -0.15 eV.

Also, the energetic position of the first-neighboring species (S8 and S1) around the defect complex is down-shifted by -0.15 eV. While, the energetic position for the atoms S11, S10, S14, and S6, which are relatively far from the defect complex, is close to pristine CZTS.

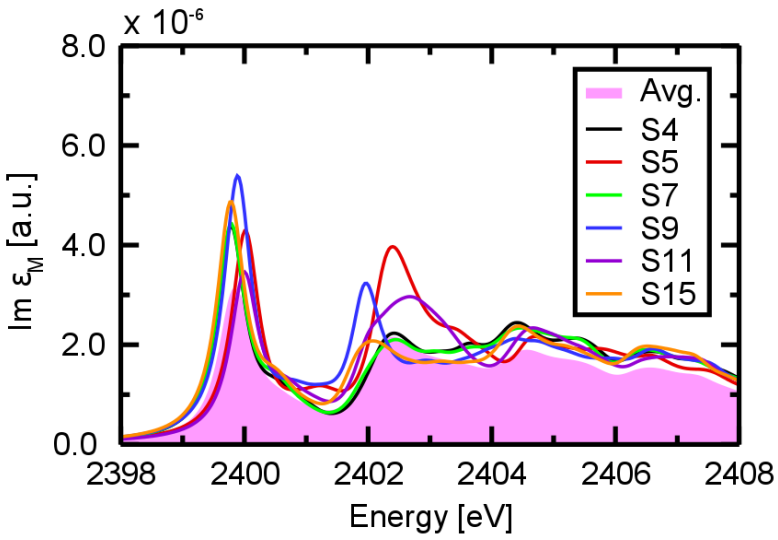

Figure 7.5.: Absorption spectra from the S K-edge of Cu_{Zn}+Zn_{Cu}. BSE results of selected inequivalent S atoms as the average over the diagonal Cartesian components of the imaginary part of the macroscopic dielectric tensor. The magenta line denotes the contributions from all inequivalent S atoms.

In the following, the absorption spectra are discussed for the atoms S4, S7, S15, S5, S9, and S11 and shown in Fig. 7.5. The total spectrum obtained as the average over all contributions (magenta shaded area) is characterized by a peak at 2399.85 eV followed by broad peaks at 2404.42, 2404.6, and 2406.52 eV. These features can be understood by looking into the contributions of individual S atoms to the average spectra. Overall, the absorption onsets of the inequivalent S atoms differ by about 0.24 eV. The BSE spectra from S4, S7, and S15 exhibit an onset peak at 2399.78 eV. This concerns the up-shifted core levels of S atoms close to Cu_{Zn}. The onset peak from S9 is at 2399.88 eV, and from S5 at 2400.03 eV. Though the core level of S11 is higher than S5, the onset peak of S11 is close to S5. Overall the shifts in the absorption onset of the individual spectra can be understood by the interplay between core-level shifts and exciton binding energies, which will be discussed in the following.

The excitonic nature of the spectral features can be examined by comparison with the IPA spectra. The BSE (solid red lines) and IPA (solid black lines) spectra from the selected inequivalent S atoms are shown in Fig. 7.6. The inclusion of *e-h* interaction red-shifts the absorption onset and redistributes the spectral weight with respect to IPA. Excitonic effects enhance the peak

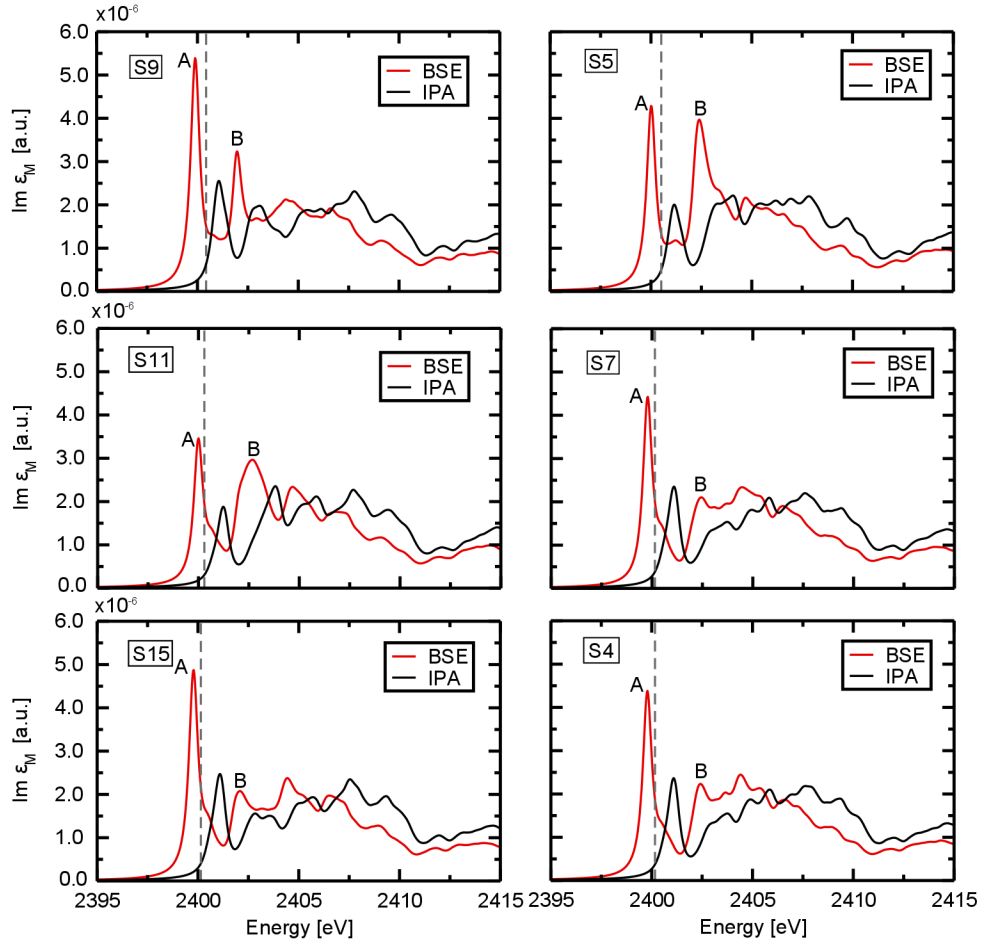

Figure 7.6.: Absorption spectra of the S K-edge from the inequivalent S atoms in Cu_{Zn}+Zn_{Cu}. Solutions from the BSE and IPA are shown by red and black solid lines. The vertical lines denote the IPA onset.

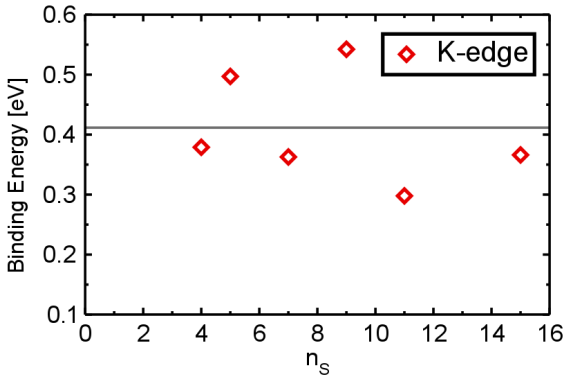

Figure 7.7.: Binding energies of the lowest-energy excitons of inequivalent S atoms in Cu_{Zn}+Zn_{Cu}. The horizontal gray line indicates the binding energy of the single-phase CZTS.

intensities marked as A and B. For all the S atoms, peak A is attributed to a bound *e-h* pair with intense oscillator strength. The corresponding binding energies are shown in Fig. 7.7 in comparison with the single-phase CZTS. It can be observed that the excitations from S4, S7, and S15 that have up-shifted core levels exhibit low binding energy of about ∼0.3 eV. It is evident from above that the absorption onset is lower for the transitions from the up-shifted core levels. The lower binding energy causes a blue-shift, and thus, there is a partial compensation. The excitations from down-shifted core levels S5 and S9 exhibit high binding energies of about 0.46 and 0.51 eV respectively. S11 has a low exciton binding energy, and thus, the onset is shifted to higher energy.

Between 2401.9 and 2403.35 eV (peak B in Fig. 7.6), the spectral features are red-shifted for all S atoms. These shifts can be explained in the same way as peak A. The excitonic character of peak B from the individual S atom is discussed further below. Above 2405 eV, the difference in peak positions becomes smaller. This is because the defects have more impact on the bands around the gap, and the *e-h* interactions do not play a major role at higher energies.

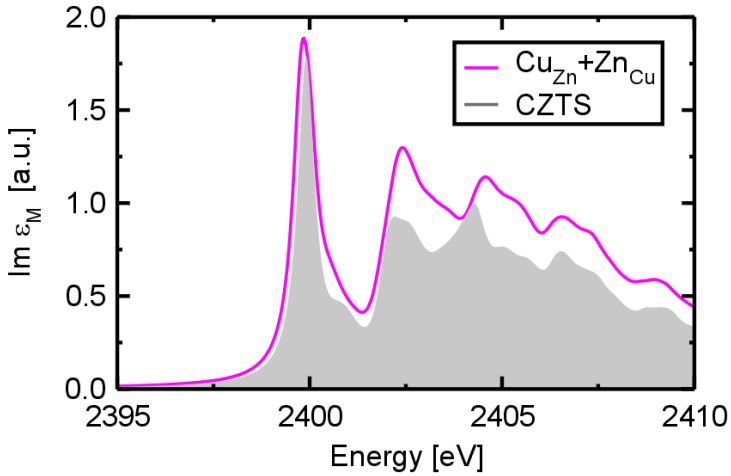

Figure 7.8.: The average spectra (solid magenta line) of Cu_{Zn}+Zn_{Cu} in comparison with BSE spectra of the single-phase CZTS (gray-shaded area).

In Fig. 7.8 the total spectrum (solid magenta line) of Cu_{Zn}+Zn_{Cu} in comparison with the single-phase CZTS (gray shaded area) are shown. As the bandgap is 0.09 eV smaller in Cu_{Zn}+Zn_{Cu}, a lower absorption onset can be expected in comparison with CZTS. However, this is not the case. The spectral features of Cu_{Zn}+Zn_{Cu} and CZTS are similar at the absorption onset. This can be explained by the partial compensation between the ΔE (Fig. 7.4) and exciton binding energy (Fig. 7.7), as discussed above. As mentioned before, the excitations from the up-shifted core levels (see Fig.

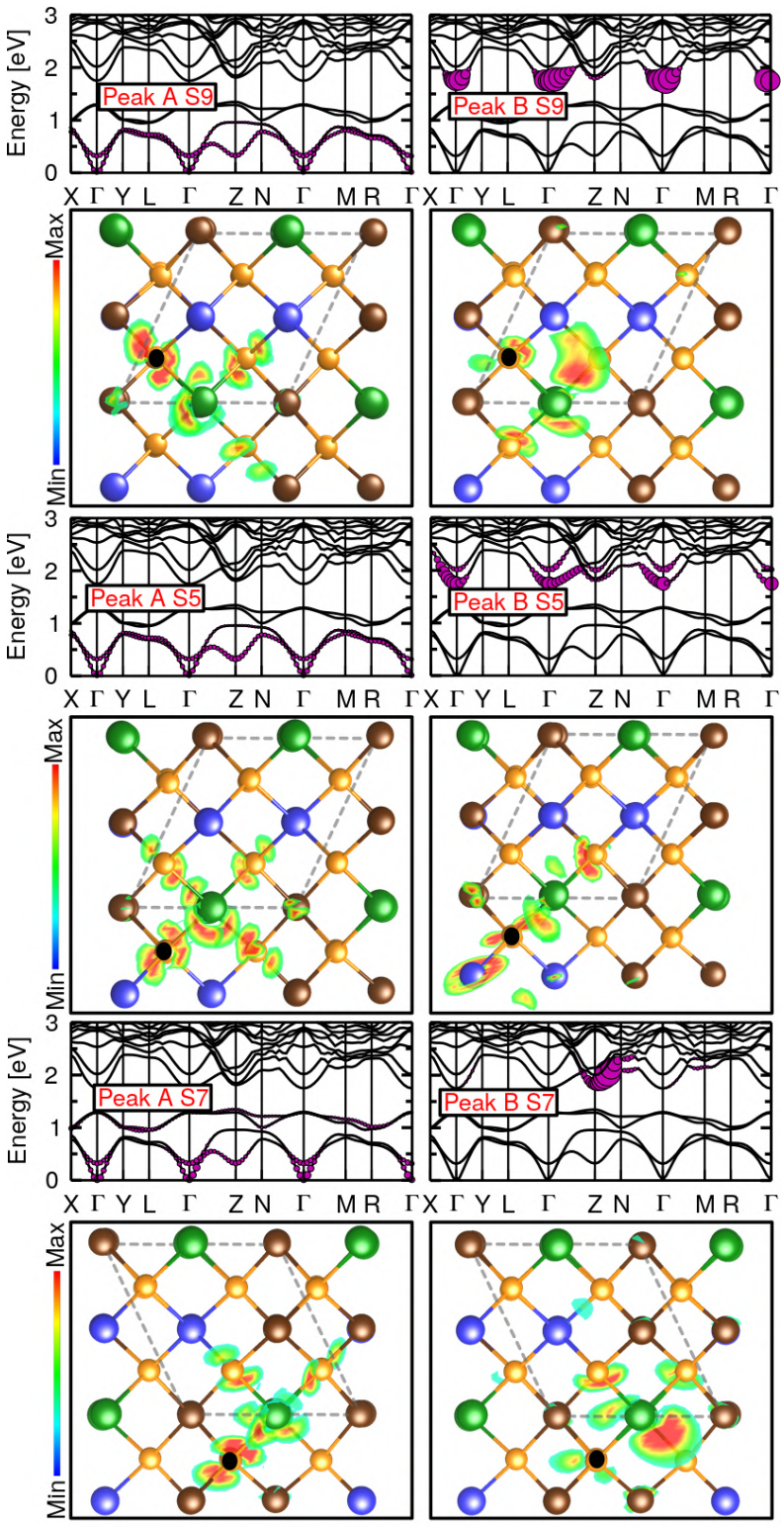

Figure 7.9.: Contributions of individual bands to the excitations of peaks A (left panels) and B (right panels) of S9, S5, and S7. The size of the magenta-colored circles quantifies the weight of the respective electronic state in the excitonic eigenstate. Their respective bottom-panel shows the real-space representation of the electron distribution. In all cases, the fixed hole position is marked by a black circle. Cu atoms are displayed in brown, Zn atoms in blue, Sn atoms in green, S atoms in orange.

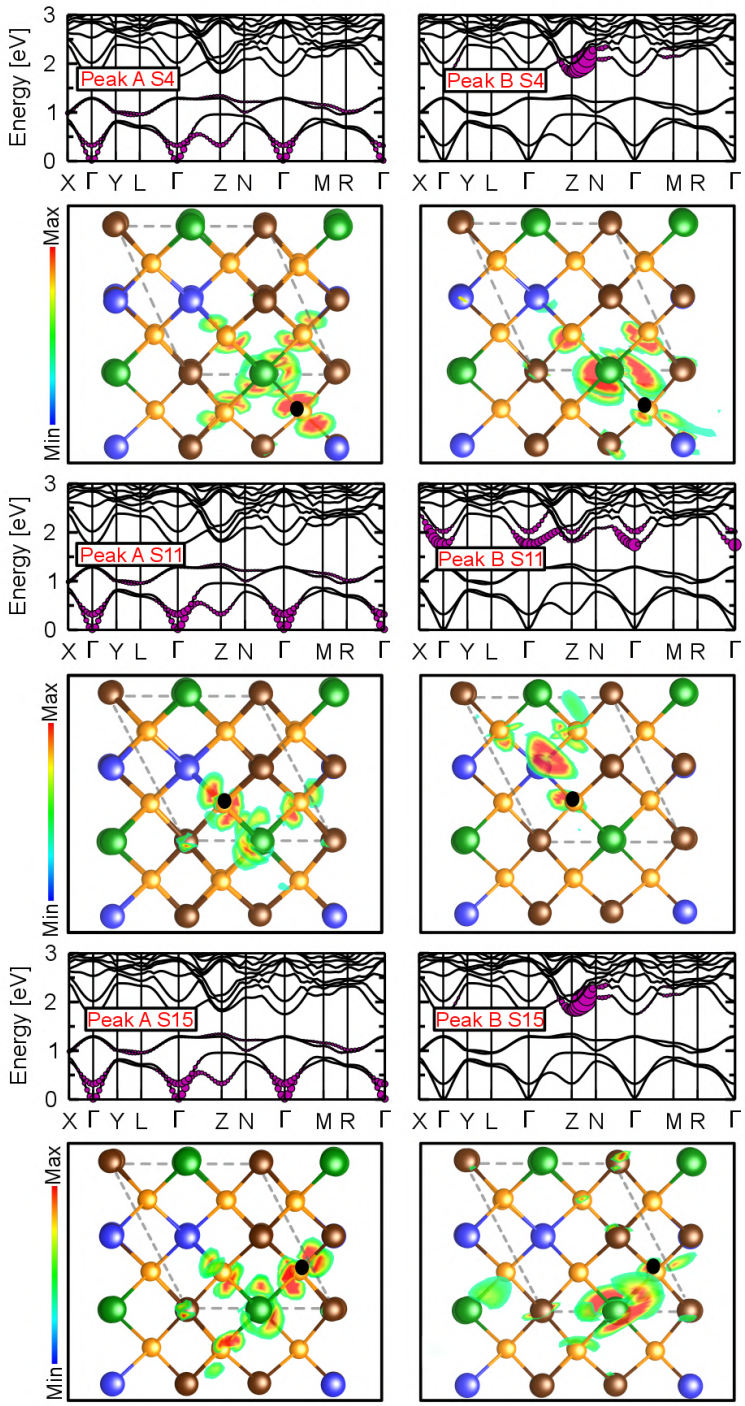

Figure 7.10.: Contributions of individual bands to the excitations of peaks A (left panels) and B (right panels) of S4, S11, and S15. The size of the magenta-colored circles quantifies the weight of the respective electronic state in the excitonic eigenstate. Their respective bottom-panel shows the real-space representation of the electron distribution. In all cases, the fixed hole position is marked by a black circle. Cu atoms are displayed in brown, Zn atoms in blue, Sn atoms in green, S atoms in orange.

7.4) exhibit lower binding energies (see Fig. 7.7). Likewise, the excitations from down-shifted core levels exhibit higher binding energies. For example, the excitation of S9, where the core level is down-shifted (-0.15 eV), exhibits higher binding energy (+0.13 eV). Thus, the partial compensation between bandgap, core level shift, and binding energy gives rise to slightly blue-shifted spectra that coincide with that of CZTS. Between 2402.0 and 2405.5 eV, the spectral features are shifted with respect to each other. These shifts can be explained in the same way as the onset. Above 2406.5 eV, the intensity of Cu_{Zn}+Zn_{Cu} is higher compared to CZTS while the features become more similar.

To analyze the excitonic character of peaks A and B of the S atoms marked in Fig. 7.6, the band contributions to these excitons are shown by projecting the excitonic weights onto the KS band structure in Figs. 7.9 and 7.10. Peak A from all the S atoms (left-panel) stems from excitations to the conduction bands up to 1.2 eV. The excitonic weights are distributed over the entire BZ. Peak B from S9, S5, and S11 (right panel) arise from excitations to the conduction bands up to 2.5 eV. Though the excitonic weights are distributed over the entire BZ, dominant contributions come from around the Γ point. In S7, S4, and S16 the dominant contribution to peak B is from the path Z-N. The energy bands taking part in these excitations are dominated by S *p* states (Fig. 7.3).

To complement this analysis, Figs. 7.9 and 7.10 display the distribution of the *e-h* wavefunction in real space. The exciton wavefunctions corresponding to peak A in all S atoms are similar to each other. The electron probability is not fully localized at the excited S atom but also extends to the first neighboring Sn atom and the S atoms surrounding it. Likewise, the exciton wavefunction corresponding to peak B in S5 and S9 are similar to each other. The electron probability is not localized at the S atom but also extends to the first neighboring Sn and Zn atoms. In the case of S11, the electron wavefunction is distributed between S and Zn atoms. In the case of S4, S7, and S15, the electron probability also extends to the first neighboring Sn and the S atoms surrounding it.

7.1.3. Sulfur $L_{2,3}$ edge

In this section, the absorption spectra of sulfur $L_{2,3}$-edge of the defect complex Cu_{Zn}+Zn_{Cu} in CZTS are presented. Here, for an accurate description of the spectra, it is important to include the spin-orbit splitting between the L_2 and L_3 edge. Because of the small splitting (1.2 eV), the transitions from S $2p_{3/2}$ (L_3 edge) and $2p_{1/2}$ (L_2 edge) initial states have to be considered

simultaneously. Like in K edge (Fig. 7.11), the absorption spectra are calculated for the inequivalent sulfur atoms labeled in the supercell (Fig. 7.1). First, it is important to understand the relative core levels shift (ΔE) upon the defect formation. The ΔE for the inequivalent sulfur atoms is shown in Fig. 7.11. Overall, the energetic position of the L_2 and L_3 edges are shifted by the same amount as observed in the K edge (Fig. 7.4). The energetic positions of the atomic species S4, S7, and S15 that are close to the acceptor point defect Cu_{Zn} are up-shifted by +0.14 eV. The energetic positions of the species S5 and S16 that are close to donor defect Zn_{Cu} down-shifted by -0.25 eV. The energetic position of the species S9, which is shared by both the point defects Cu_{Zn} and Zn_{Cu}, is down-shifted by -0.15 eV. Also, the energetic position of the first-neighboring species (S8 and S1) around the defect complex is down-shifted by -0.15 eV. While, the energetic position for the atoms S11, S10, S14, and S6, which are relatively far from the defect complex, is close to pristine CZTS. Like in K-edge, the absorption spectra are calculated for atoms S4, S7, S15, S5, S9, and S11.

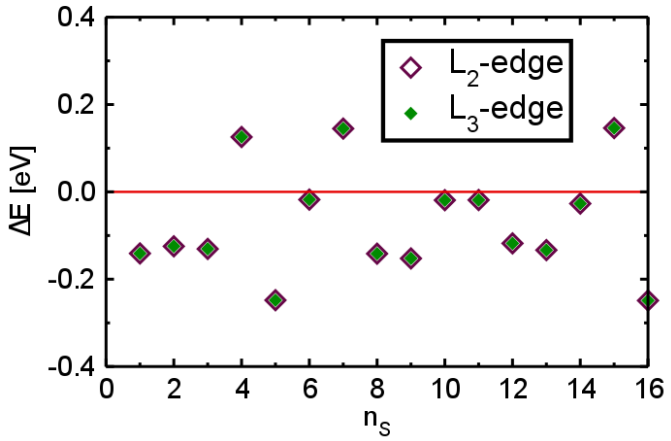

Figure 7.11.: Core-level shifts (ΔE) of the S $2p_{1/2}$ (maroon) and $2p_{3/2}$ (green) inequivalent sulfur atoms, marked in Fig. 7.1 with respect to that of single phase CZTS. The shifts are calculated by taking the VBM as reference.

The absorption spectra of the atoms S4, S5, S7, S9, S11, and S15 in Cu_{Zn}+Zn_{Cu} and their average spectrum is shown in Fig. 7.12. The total spectrum obtained as the average over all contributions (magenta shaded area) is characterized by a peak at 150.3 eV, followed by a shoulder at 151.5 eV and another pronounced peak at 152.5 eV. These features can be understood by looking into the contribution of individual S atoms to the total spectra. Similar to K-edge, the absorption onset of the inequivalent S atoms differs by 0.24 eV. The BSE spectra from S4, S7, and S15 have an onset peak at 150.25 eV. This concerns the up-shifted core levels of S atoms close to Cu_{Zn}. The onset peak from S9 is at 150.25 eV. The onset peak from S5 and S11 is at 150.5 eV. Though the core level of S11 is higher than S5, the onset peak

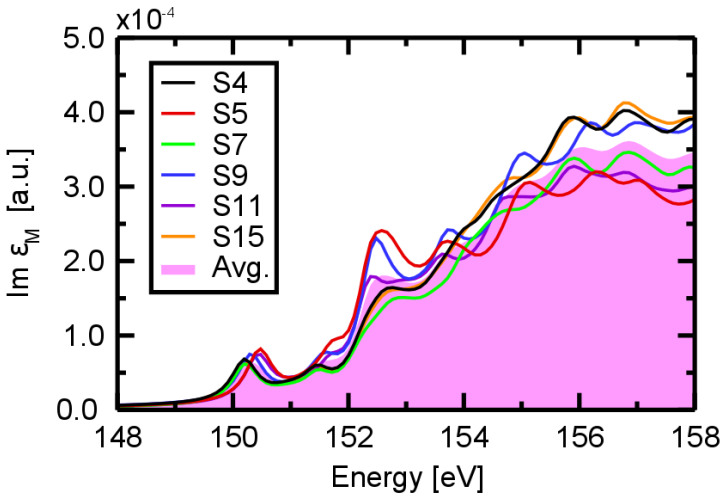

Figure 7.12.: Absorption spectra from the S $L_{2,3}$-edge of Cu_{Zn}+Zn_{Cu}. BSE results of the selected inequivalent S atoms as the average over the diagonal Cartesian components of the imaginary part of the macroscopic dielectric tensor. The magenta line denotes the average of all inequivalent S atoms.

of S11 is close to S5. As seen in the K edge, the shifts in the absorption onset of the individual spectra can be understood by the interplay between core-level shifts and exciton binding energies, which will be discussed in the following.

The excitonic nature of the spectral features can be examined by comparison with IPA spectra. The BSE (solid red lines) and IPA (solid black lines) spectra from the selected inequivalent S atoms are shown in Fig. 7.13. As observed in the previous case, the inclusion of *e-h* interaction red-shifts the absorption onset and redistributes the spectral weights with respect to IPA. Excitonic effects enhance the peak intensities marked as A, B, C, and D. For all the S atoms, peak A is attributed to a bound excitonic state. The corresponding binding energies are shown in Fig. 7.14 in comparison with the single-phase CZTS. As observed in K-edge, the excitations from S4, S7, and S15 that have up-shifted core levels exhibit lower binding energy of about ∼0.3 eV. It is evident from above that the absorption onset is lower for the transitions from the up-shifted core levels. The lower binding energy causes a blue-shift, and thus, there is a partial compensation. The excitations from down-shifted core levels S5 and S9 exhibit higher binding energies of about 0.46 and 0.51 eV, respectively. S11 has a lower binding energy of about 0.25 eV, and thus, the onset is shifted to higher energy.

The height of the red vertical bars shows the oscillator strength of the excitons contributing to the corresponding peaks. The spectral features can be separated depending on the transitions that originate from L_2 and L_3

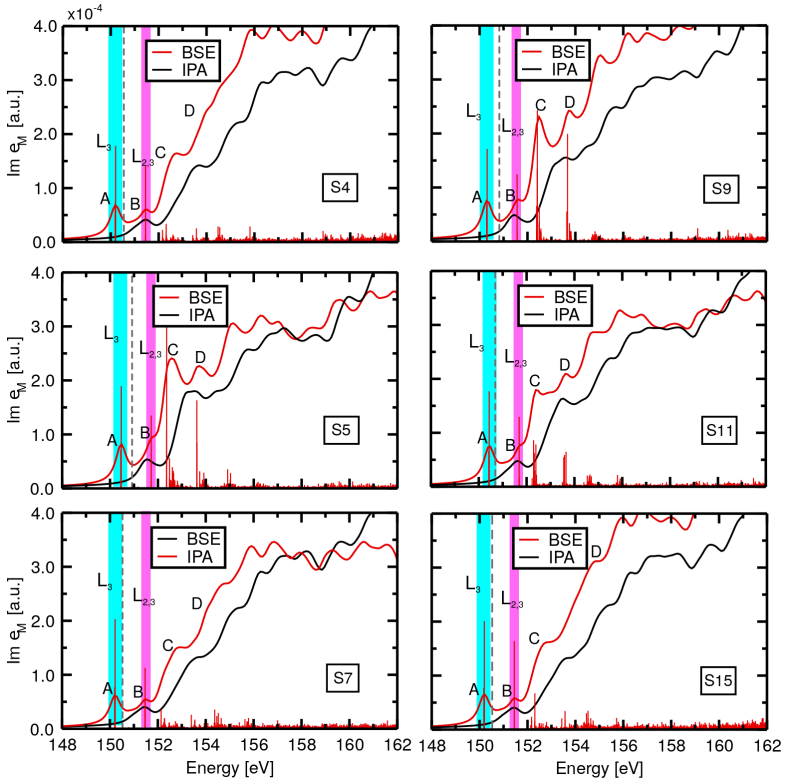

Figure 7.13.: Absorption spectra of S $L_{2,3}$-edge from the inequivalent S atoms of Cu_{Zn}+Zn_{Cu}. Solutions from the BSE and IPA are shown by solid red and black lines. The vertical line denotes the IPA onset. The oscillator strengths of the individual transitions are shown by the vertical bars, as obtained from the BSE calculations. The cyan vertical bars represent excitations from the L_3 edge, and the magenta vertical bars represent mixed transitions from the L_2 and L_3 channels.

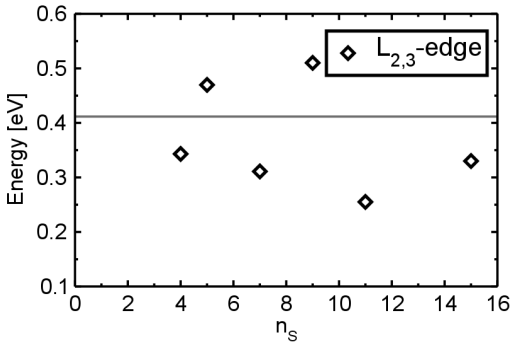

Figure 7.14.: Binding energies of the lowest-energy excitons of inequivalent S atoms in Cu_{Zn}+Zn_{Cu}. The horizontal gray line indicates the binding energy of the single-phase CZTS.

absorption edges, and by their mixing. Peak A in all the individual S atoms is formed by excitations from the $2p_{3/2}$ level (L_3 edge). Peak B is formed by mixed transitions from the L_2 and L_3 channels. Likewise, peak C originates

from excitations again from $2p_{3/2}$ core-state, and peak D is from the mixed transitions. Above 156 eV, a continuum of excitations with low intensity characterizes the spectrum. The excitonic character of peaks A and B are discussed further below.

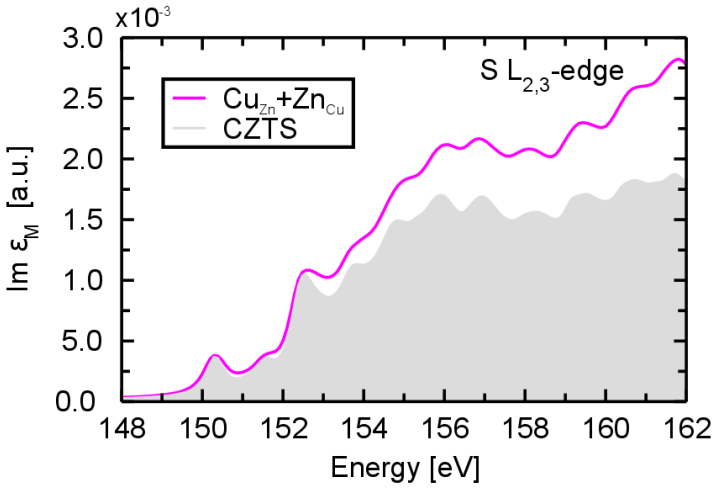

Figure 7.15.: The solid magenta line represents the total spectra of the inequivalent S atoms (see Fig. 7.12) in Cu_{Zn}+Zn_{Cu} in comparison with BSE spectra of the single-phase CZTS (gray-shaded area). For more details on CZTS see Sec. 5.3.

The total spectra (solid magenta line) of Cu_{Zn}+Zn_{Cu} in comparison with the single-phase CZTS (gray shaded area) are shown in Fig. 7.15. As observed in K-edge (see Section 7.1.2), the onset of the total spectra and CZTS are similar. As mentioned in Section 7.1.2, the similarities in the onset are assigned to the partial compensation between the core-level and exciton binding energies at the onset. The excitations from the up-shifted core levels (see Fig. 7.11) exhibit lower binding energies (see Fig. 7.14). Likewise, the excitations from down-shifted core levels exhibit higher binding energies. Thus, the partial compensation gives rise to slightly blue-shifted spectra that coincide with that of CZTS. Above 152.5, it can be observed that the total spectrum of Cu_{Zn}+Zn_{Cu} exhibits higher intensity than CZTS while the features become more similar.

To analyze the excitonic character of peaks A and B of the S atoms marked in Fig. 7.13, the band contributions to these excitons are shown by projecting the excitonic weights onto the KS band structure in Fig. 7.16 and 7.17. Peaks A and B from all the S atoms stems from excitations to the conduction band up to 1.2 eV. The exciton weights are distributed over the entire BZ for all the cases. However, the dominant contribution to peak B in S5 is at point R and in S15 is from the path Γ-N. To complement this analysis, Fig. 7.16 and 7.17 display the distribution of the *e-h* wavefunction in real-space. The

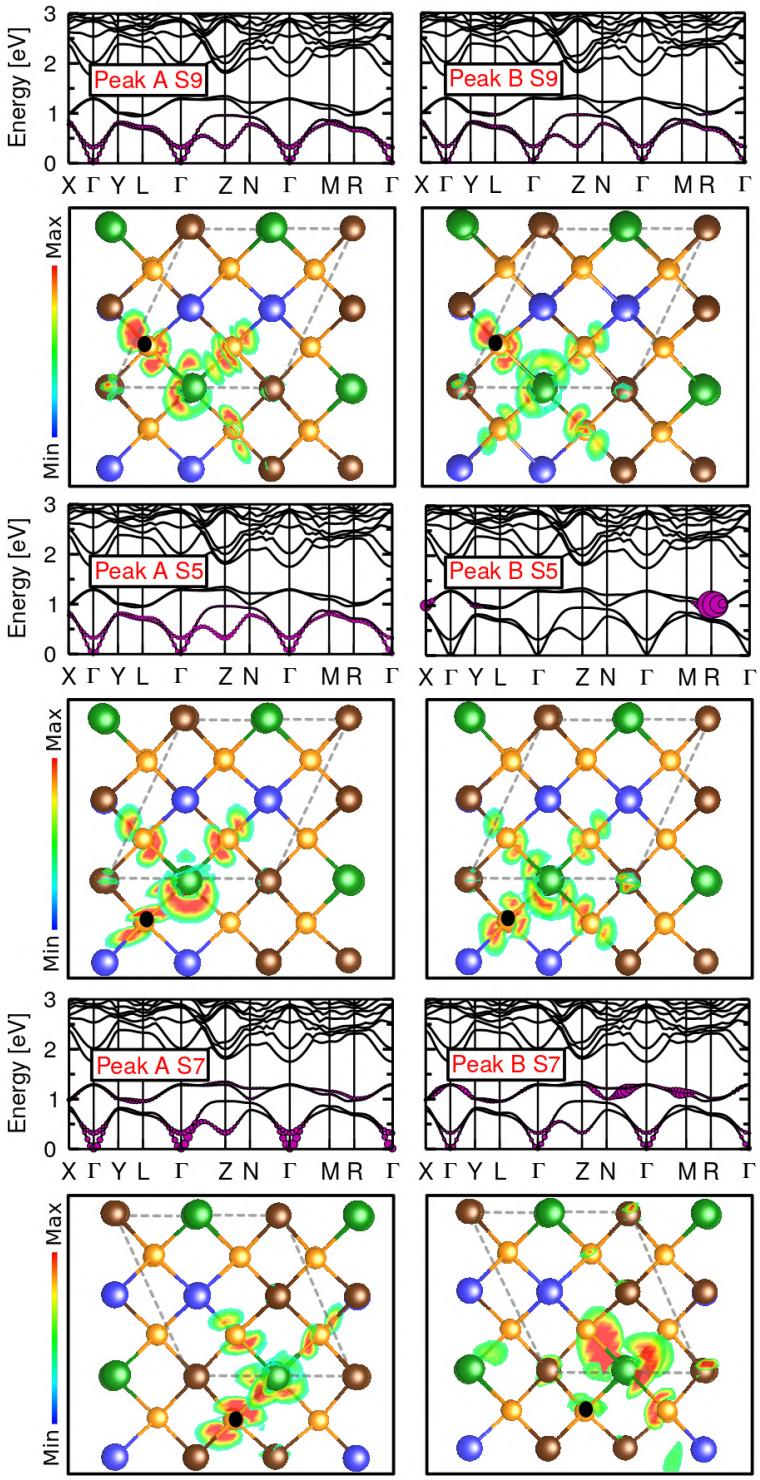

Figure 7.16.: Contributions of individual bands to the excitations of peak A and B in S9, S5, and S7 marked in Fig. 7.13. The size of the magenta-colored circles quantifies the weight of the respective electronic state in the excitonic eigenstate. Their respective bottom-panel shows the real-space representation of the electron distribution In all cases, the fixed hole position is marked by a black circle. Cu atoms are displayed in brown, Zn atoms in blue, Sn atoms in green, S atoms in orange.

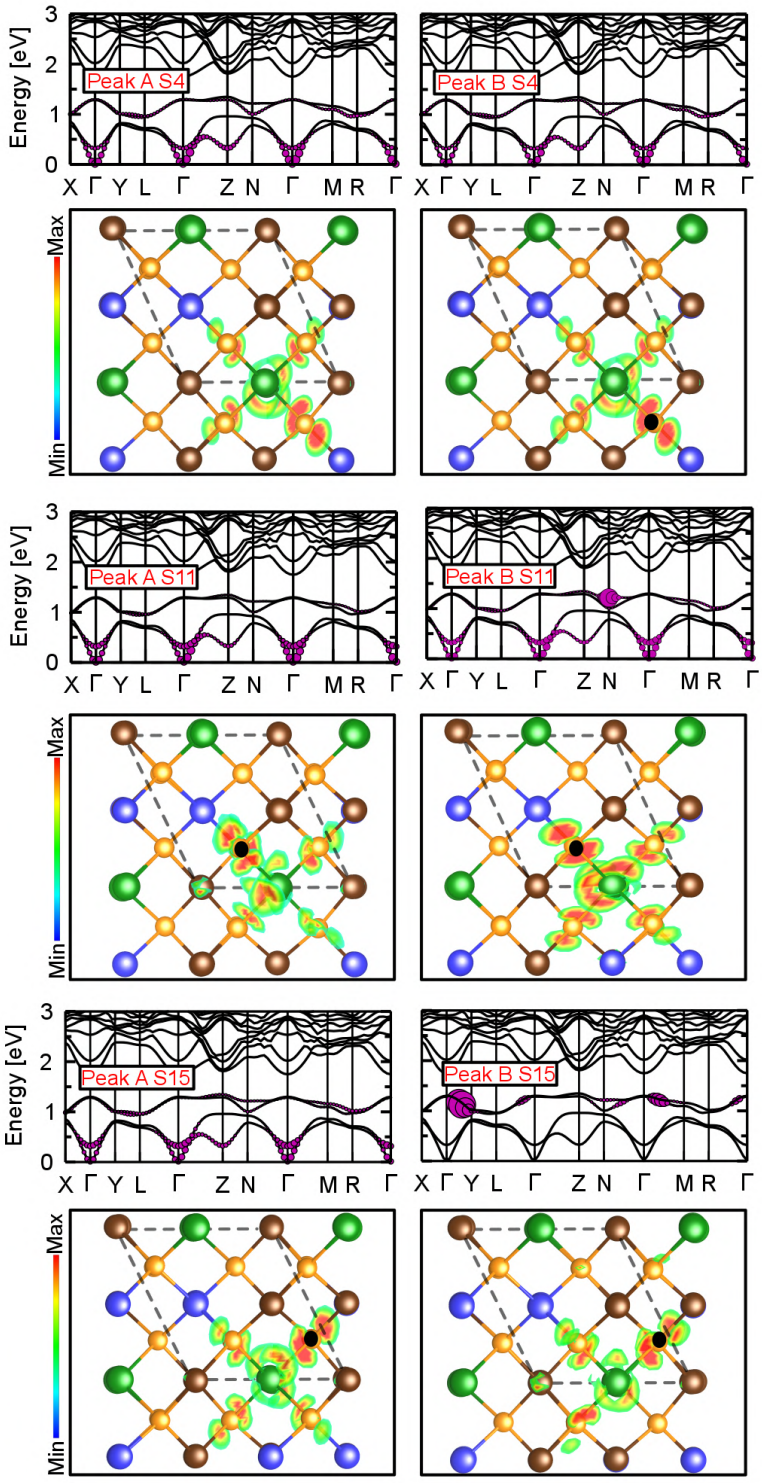

Figure 7.17.: Contributions of individual bands to the excitations of peak A and B in S4, S11, and S15 marked in Fig. 7.13. The size of the magenta-colored circles quantifies the weight of the respective electronic state in the excitonic eigenstate. Their respective bottom-panel shows the real-space representation of the electron distribution In all cases, the fixed hole position is marked by a black circle. Cu atoms are displayed in brown, Zn atoms in blue, Sn atoms in green, S atoms in orange.

exciton wavefunctions corresponding to peaks A and B in all the calculated S atoms are similar. The electron probability is not fully localized at the excited S atom but also extends to the first neighboring Sn atom and the S atoms surrounding it.

7.2. V_{Cu}+Zn_{Cu} in CZTS

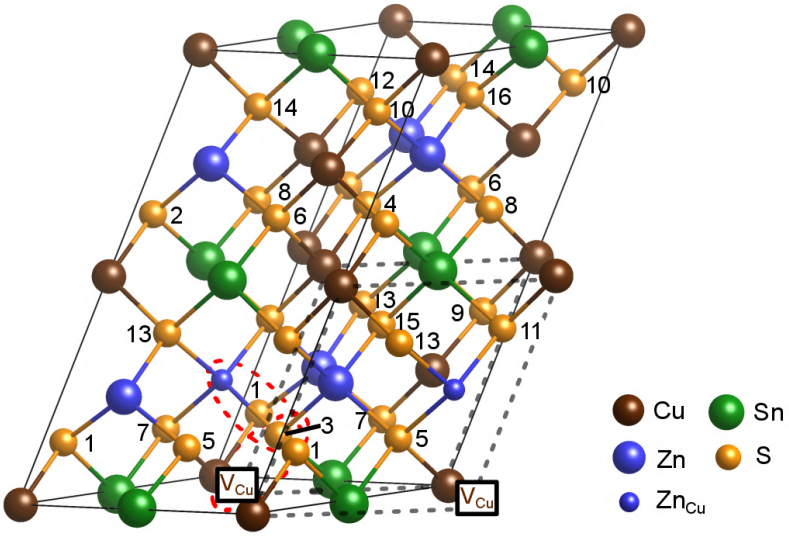

Figure 7.18.: Atomic configuration of the defect complex V_{Cu}+Zn_{Cu} in CZTS. The acceptor (V_{Cu}) and donor (Zn_{Cu}) defects are placed closely to each other to form a complex (red oval lines). The inequivalent sulfur sites are labeled wit their index n_S. The unit cell of the single-phase CZTS is highlighted with dashed line.

The atomic configuration of defect complex V_{Cu}+Zn_{Cu} in CZTS is shown in Fig. 7.18. The point defects V_{Cu} and Cu_{Zn} are placed close to each other to form a defect complex marked by a dashed red oval lines. The low symmetry makes the sulfur atoms inequivalent which is marked with their index n_S. Starting from the experimental lattice parameters [6] of pristine CZTS, the atomic coordinates are relaxed until residual forces per atom are smaller than 0.05 eV/Å. For ease of discussion, the acronym V_{Cu}+Zn_{Cu} is used to denote the material.

7.2.1. Electronic Structure

In Fig. 7.19(a) the BZ of the triclinic lattice structure and the location of the high-symmetry points used calculate the band structure are shown. The

band structure and the PDOS calculated on the GGA-PBE level is shown in Fig. 7.19(b). Like observed in Cu_{Zn}+Zn_{Cu}, the bands around the bandgap region are strongly dispersion. V_{Cu}+Zn_{Cu} exhibits a direct bandgap of 0.25 eV at the Γ point. In comparison with pristine CZTS the bandgap is increased by 0.10 eV. The PDOS of the pristine material and V_{Cu}+Zn_{Cu} are similar.

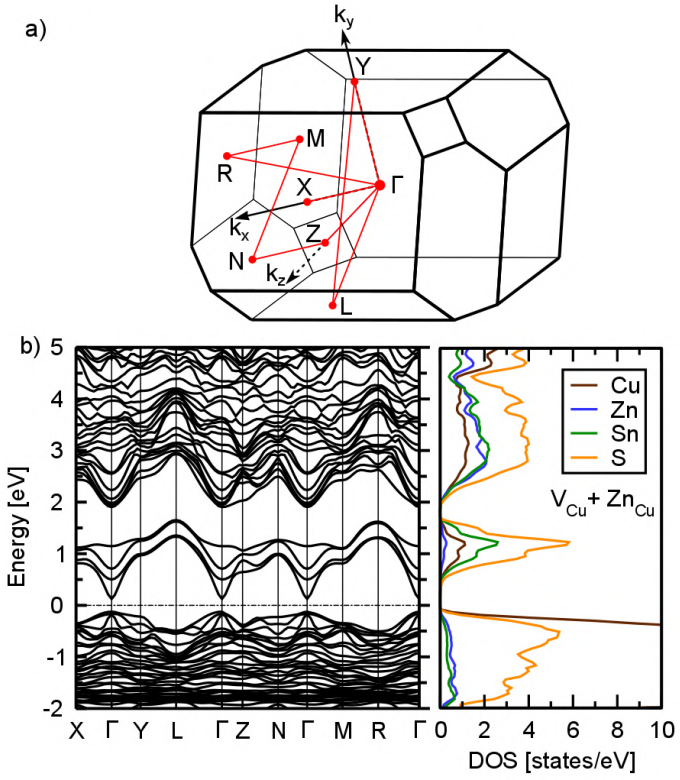

Figure 7.19.: a) Brilloiun zone (BZ) of CZTS with the defect complex V_{Cu}+Zn_{Cu} showing the location of high-symmetric points. b) Band structure and PDOS for the energy region between -2 and 5 eV.

The atomic-orbital characters projected on the conduction band region are shown in Fig. 7.20. Overall, the atomic contributions to the conduction band region of the pristine CZTS (see Fig. 5.3) and the V_{Cu}+Zn_{Cu} are very similar. The contribution to the low-lying conduction bands up to 1.5 eV are from Sn- 5*s* and S-3*p* states. The bands in the energy range between 2.2 to 4 eV have a major contribution from Zn-4*s*, S-3*p*, and Sn-4*d* states. There are contributions from Cu-4*s* states at higher energies.

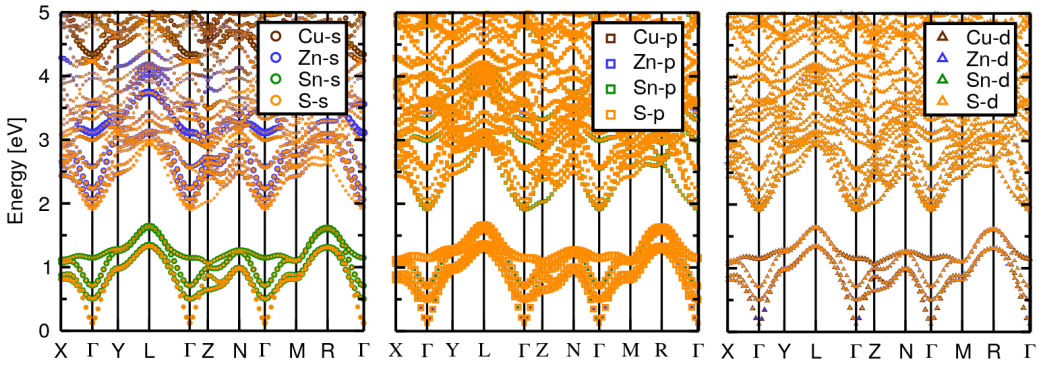

Figure 7.20.: Atomic-orbital *s* (left), *p* (middle), and *d* (right) characters projected on the band structure of V_{Cu}+Zn_{Cu} in the conduction band region. The color code indicates contributions from Cu (brown), Zn (blue), Sn (green), and S (orange). The size of the symbols quantifies the weight of *s*, *p*, and *d* character.

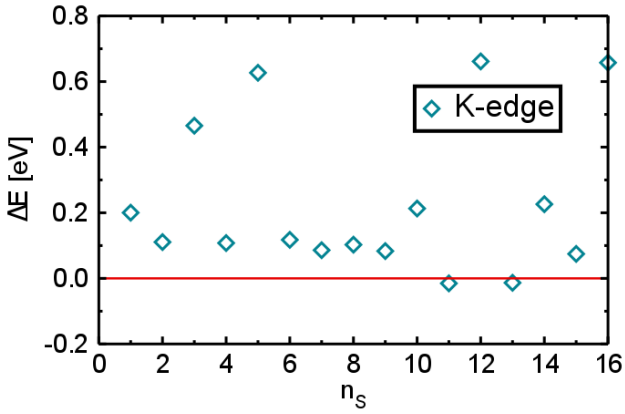

Figure 7.21.: Core-level shifts (ΔE) of the S 1*s* states for the inequivalent sulfur atoms, marked in Fig. 7.18 with respect to that of single phase CZTS. The shifts are calculated by taking the VBM as reference.

7.2.2. Sulfur K edge

In this section, the absorption spectra of sulfur K-edge of defect complex V_{Cu}+Zn_{Cu} in CZTS are presented. As in the previous case, the absorption spectra are calculated for the inequivalent sulfur atoms labeled in the super-cell (Fig. 7.18). First, it is important to understand the core level shifts (ΔE) upon defect formation since they are sensitive to the chemical environment. The ΔE for the inequivalent sulfur atoms is shown in Fig. 7.21. Overall, most of the core states experience positive shifts. The atomic species S5, S12, and S16 are close to the acceptor point defect V_{Cu}. Their energetic positions are up-shifted by 0.66 eV. The energetic position of the atoms S11 and S13, which are around the donor point defect Zn_{Cu} are close to pristine CZTS. The energetic position of the atom S7, which is around Zn_{Cu} and close to

V_{Cu} is up-shifted by 0.08 eV. The energetic position of atomic species S3, which is shared by both the point defects V_{Cu} and Zn_{Cu} is up-shifted by 0.47 eV. The energetic position for the first-neighboring atoms S1, S10, and S14 is up-shifted by 0.20 eV. The energetic position of the second-neighboring atoms S2, S4, S6, S8, S9, and S15 are $\sim$ 0.11 eV.

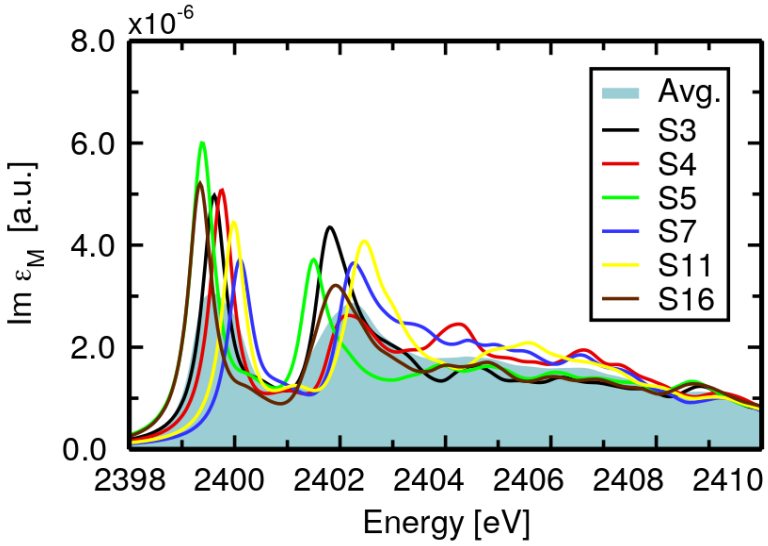

Figure 7.22.: Absorption spectra from the S K-edge of V_{Cu}+Zn_{Cu}. BSE results of selected inequivalent S atoms as the average over the diagonal Cartesian components of the imaginary part of the macroscopic dielectric tensor. The cyan-shaded area denotes the contributions from all inequivalent S atoms.

In the following, the absorption spectra are discussed for the atoms S3, S4, S5, S7, S11, and S16. The K-edge absorption spectra of the inequivalent sulfur atoms in V_{Cu}+Cu_{Zn}. The total spectrum obtained as the average over all contributions (cyan shaded area) is characterized by a peak at 2399.61 eV, followed by another peak at 2402.25 eV and a broad peak at 2404.45 eV. These features can be understood by looking into the contribution of individual S atoms to the total spectra. Overall, the absorption onsets of the inequivalent S atoms differ by about 0.67 eV. The BSE spectra from S5 and S16 exhibits an onset peak at 2399.37 eV. This concerns the up-shifted core levels of S atoms close to V_{Cu}. The onset peak from S11 is at 2400.11 eV, and from S3 is at 2399.64 eV. The core level of S7 and S4 is the same. However, they exhibit different onsets. The onset of S4 is at 2399.75 eV reflects the ΔE whereas, the onset peak of S7 appears at higher energy. As discussed before, the shifts in the absorption onset of the individual spectra can be understood by the interplay between core level shifts and exciton binding energies, which will be discussed in the following.

The excitonic nature of the spectral features can be examined by comparison with the IPA spectra. The BSE (solid red lines) and IPA (solid black lines)

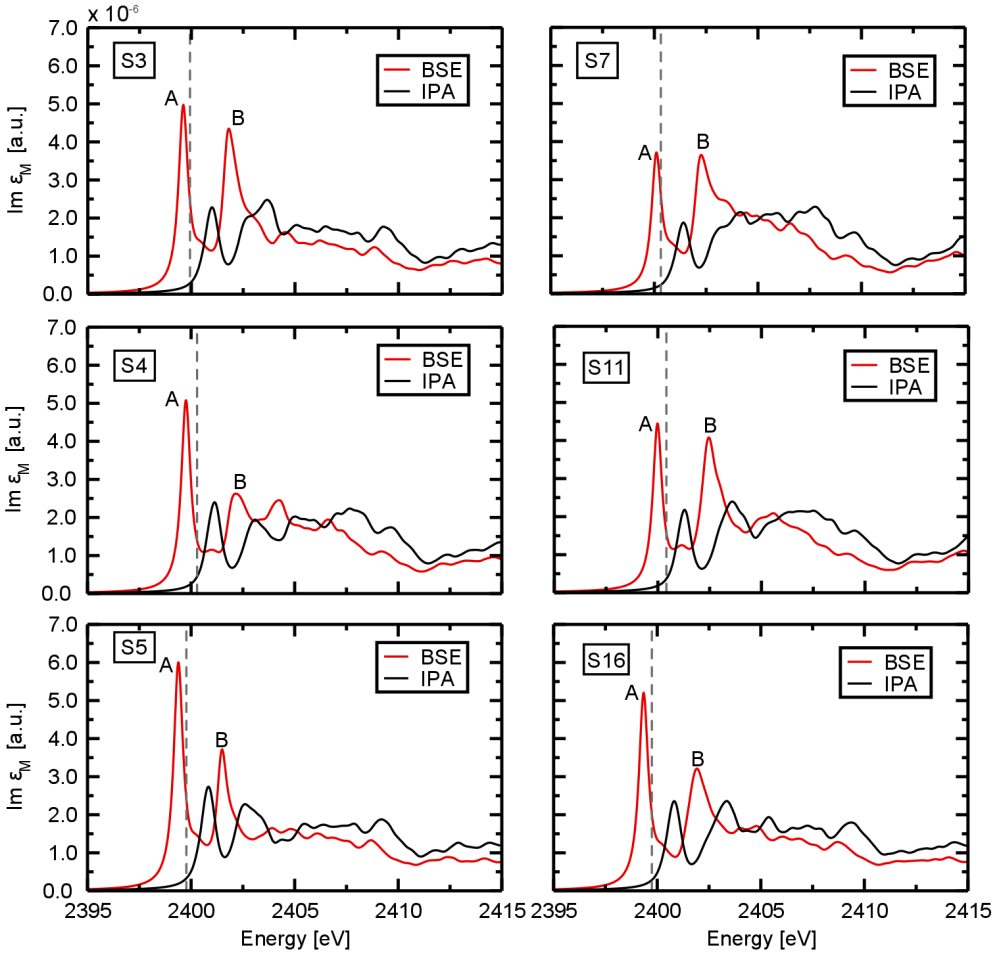

Figure 7.23.: Absorption spectra of the S K-edge from the inequivalent S atoms in V_{Cu}+Zn_{Cu} in CZTS. Solutions from the BSE and IPA are shown by red and black solid lines. The vertical line denotes the IPA onset.

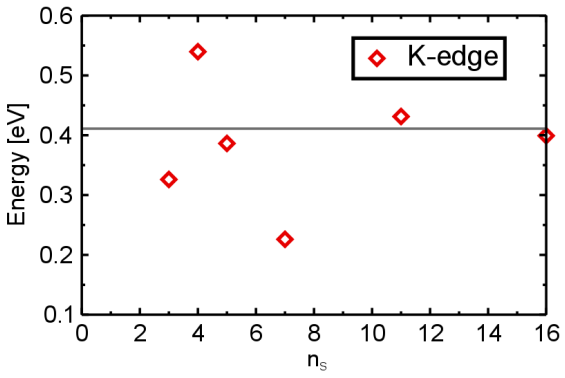

Figure 7.24.: Binding energies from the lowest-energy excitons of inequivalent S atoms in V_{Cu}+Zn_{Cu}. The horizontal gray line indicates the binding energy of the single-phase CZTS.

spectra from the selected inequivalent S atoms are shown in Fig. 7.23. As observed in previous cases, the inclusion of *e-h* interaction red-shifts the absorption onset and redistributes the spectral weight with respect to IPA. Excitonic effects enhance the peak intensities marked as A and B. For all the S atoms, peak A is attributed to a bound *e-h* pair with intense oscillator strength. The corresponding binding energies are shown in Fig. 7.24 in comparison with the single-phase CZTS. It can be observed that the excitations from S16, which has the highest up-shifted core-level, and the excitations from S11, the down-shifted core level (Fig. 7.21) exhibit binding energy of ∼0.4 eV, similar to single-phase CZTS. Although S4 and S7 have the same ΔE, the difference in the onset peak is related to the difference in binding energy. S4 exhibits higher binding energy of 0.54 eV and S7 exhibits weakly bound excitons with a binding energy of 0.22 eV. The high binding energy of S4 is attributed to the relatively larger distance to both the point defects. The low binding energy of S7 is because S7 is around Zn_{Cu} and also close to V_{Cu} (see Fig. 7.18).

The spectral feature marked peak B in Fig. 7.23 are also red-shifted for all the S atoms. These shifts can be explained in the same way as peak A. The excitonic character of peak B from the individual S atom is discussed further below. Above 2405 eV, the difference in peak positions becomes smaller as the *e-h* interactions do not play a major role in higher energies.

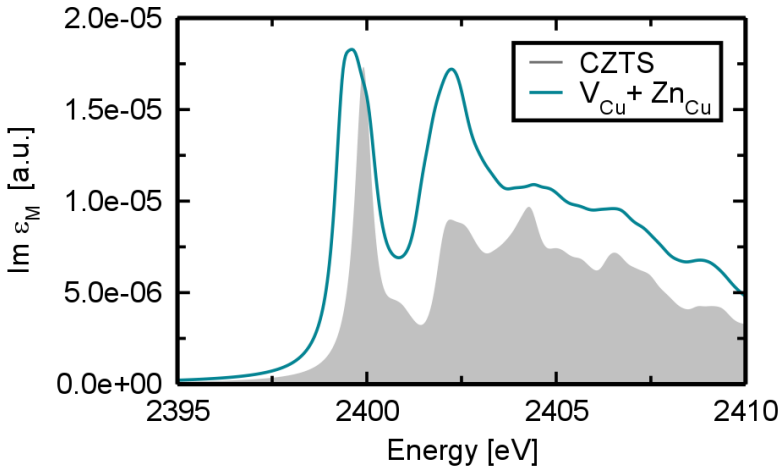

Figure 7.25.: The average spectra (solid cyan line) of V_{Cu}+Zn_{Cu} in comparison with BSE spectra of the single-phase CZTS (gray-shaded area).

In Fig. 7.25 the total spectrum (solid cyan line) of V_{Cu}+Zn_{Cu} in comparison with the single-phase CZTS (gray shaded area) is shown. As the bandgap is 0.10 eV larger in V_{Cu}+Zn_{Cu}, a higher absorption onset can be expected in comparison with CZTS. In contrast, the absorption onset is red-shifted by 0.4 eV in comparison with CZTS. This can be explained by the complex

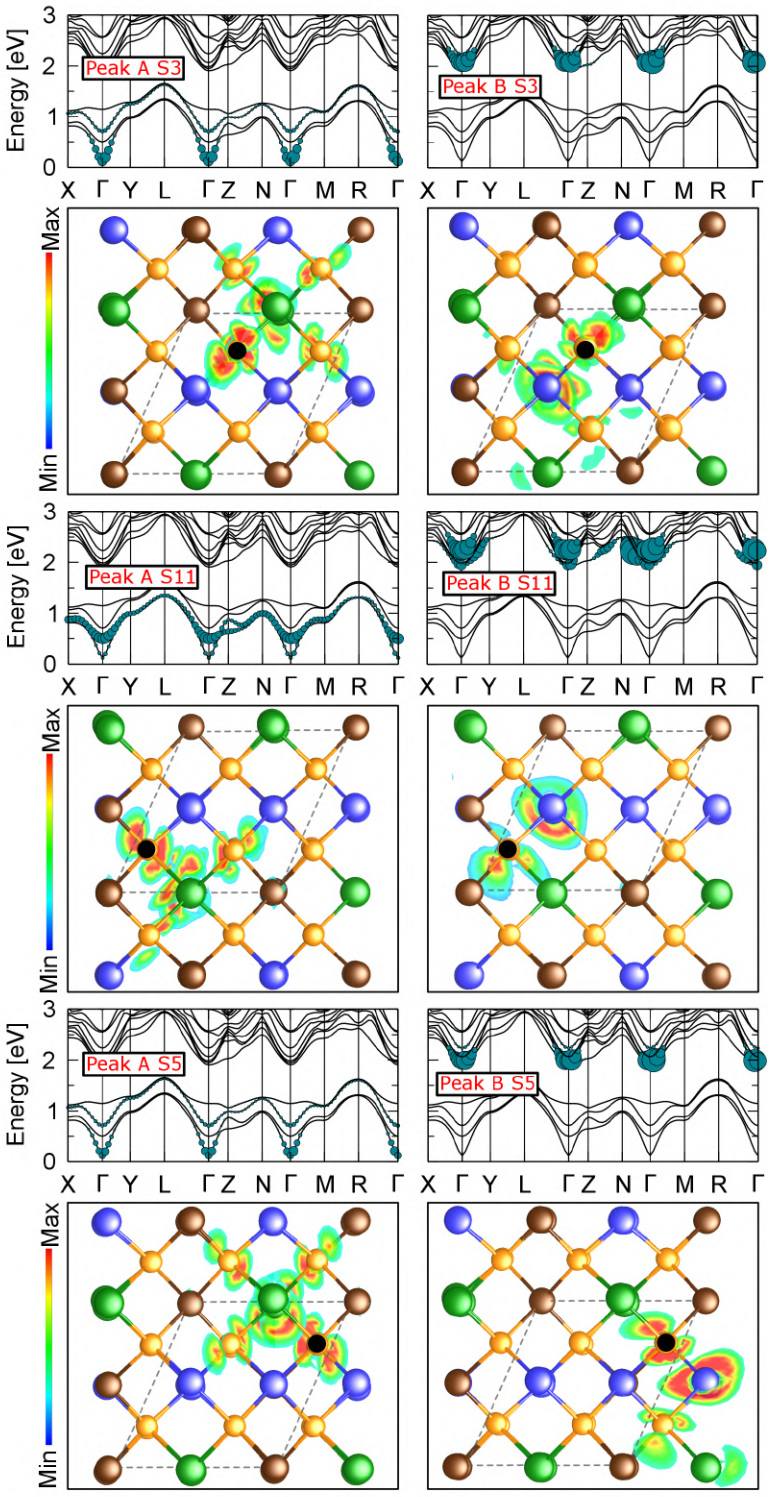

Figure 7.26.: Contributions of individual bands to the excitations of peaks A (left panels) and B (right panels) of S3, S11, and S5. The size of the cyan-colored circles quantifies the weight of the respective electronic state in the excitonic eigenstate. Their respective bottom-panel shows the real-space representation of the electron distribution. In all cases, the fixed hole position is marked by a black circle. Cu atoms are displayed in brown, Zn atoms in blue, Sn atoms in green, S atoms in orange.

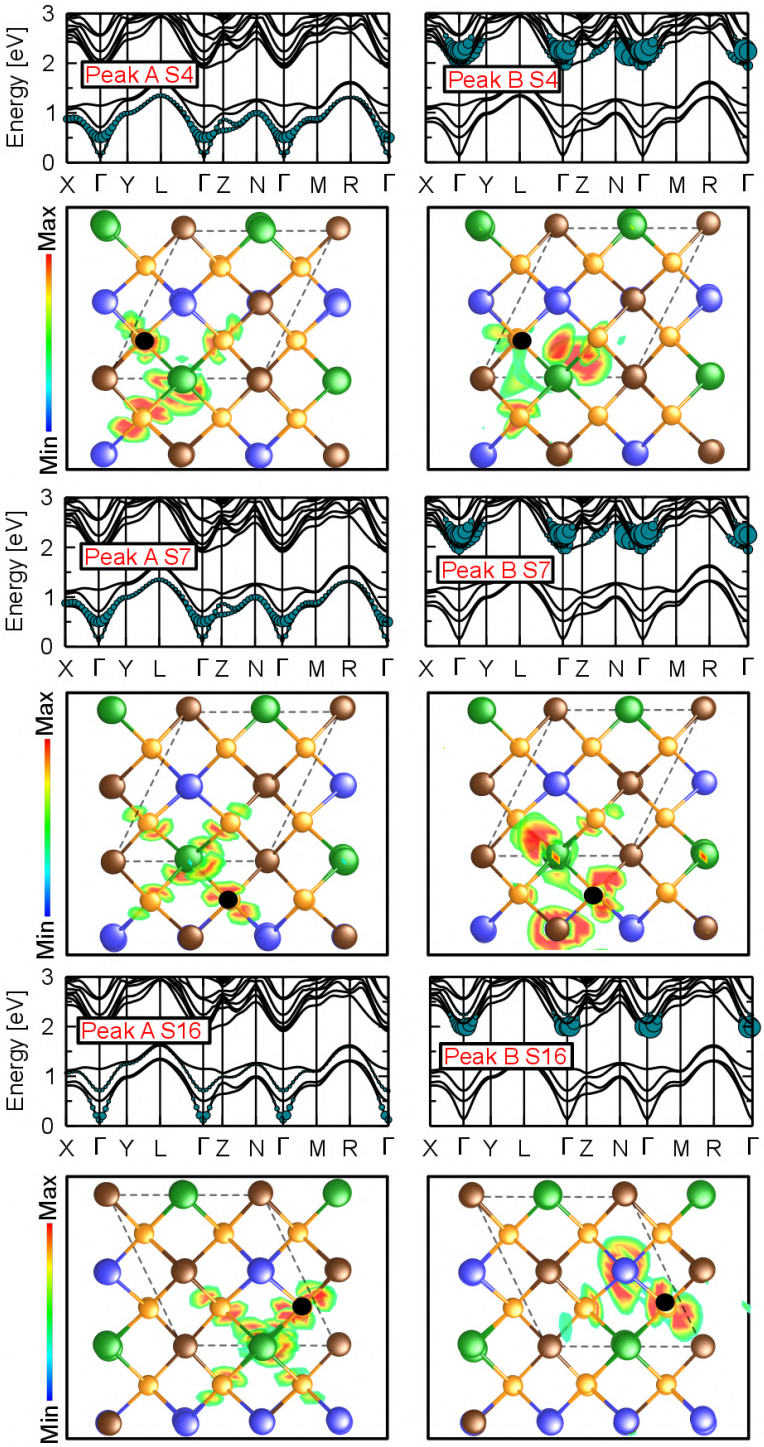

Figure 7.27.: Contributions of individual bands to the excitations of peaks A (left panels) and B (right panels) of S4, S7, and S16. The size of the cyan-colored circles quantifies the weight of the respective electronic state in the excitonic eigenstate. Their respective bottom-panel shows the real-space representation of the electron distribution. In all cases, the fixed hole position is marked by a black circle. Cu atoms are displayed in brown, Zn atoms in blue, Sn atoms in green, S atoms in orange.

interplay between the core level shift (Fig. 7.22) and exciton binding energies (7.24), and the local chemical environment, as discussed above. The excitations from the up-shifted core level (S16) and the down-shifted core level (S11) exhibits binding energies of ∼0.4 eV. In this case, the exciton binding energy and core level positions do not go hand in hand, as already mentioned. For example, S4 and S7 have the same core level position and exhibit different binding energies of 0.54 and 0.22 eV, respectively. This difference is because of the relatively large distance of S4 to both the point defects in comparison with S7. Consequently, S16 determines the onset of the total spectra that is comparable with single-phase CZTS. Between 2402.0 and 2405.5 eV, the spectral features are shifted with respect to each other. These shifts can be explained in the same way as the onset. Above 2406.5 eV, the intensity of V_{Cu}+Zn_{Cu} is higher compared to CZTS while the features become more similar.

To analyze the excitonic character corresponding to peaks A and B of the S atoms marked in Fig. 7.23, the band contributions to these excitons are shown by projecting the excitonic weights onto the KS band structure in Figs. 7.26 and 7.27. Peak A from all the S atoms (left panel) stems from excitations to the conduction bands up to 1.0 eV. Though the excitonic weights are distributed over the entire BZ, the majority of the contribution comes from the Γ point. Peak B (right panel) from all the S atoms arise from excitations to the conduction band up to 2.5 eV. The dominant contribution to peak B comes from the Γ point. The energy bands taking part in these excitations are dominated by S *p* states (see Sec. 7.2.1).

To complement this analysis, Figs. 7.26 and 7.27 display the distribution of the *e-h* wavefunction in real space. The exciton wavefunctions corresponding to peak A in all S atoms are similar to each other. The electron probability is not fully localized at the excited S atom but extends to the first neighboring Sn and the S atoms surrounding it. The electron wavefunctions corresponding to peak B in all S atoms are similar to each other. The electron probability is not localized at the S atom but also spreads out to the nearest Zn and S atoms. However, the electron wavefunctions corresponding to peak B from S4 and S7 are similar to the exciton character corresponding to peak A.

7.2.3. Sulfur $L_{2,3}$ edge

In this section, the absorption spectra of sulfur $L_{2,3}$-edge of the defect complex V_{Cu}+Zn_{Cu} in CZTS are presented. As mentioned in Section 7.1.3, the transitions from S $2p_{3/2}$ (L_3 edge) and $2p_{1/2}$ (L_2 edge) initial states are

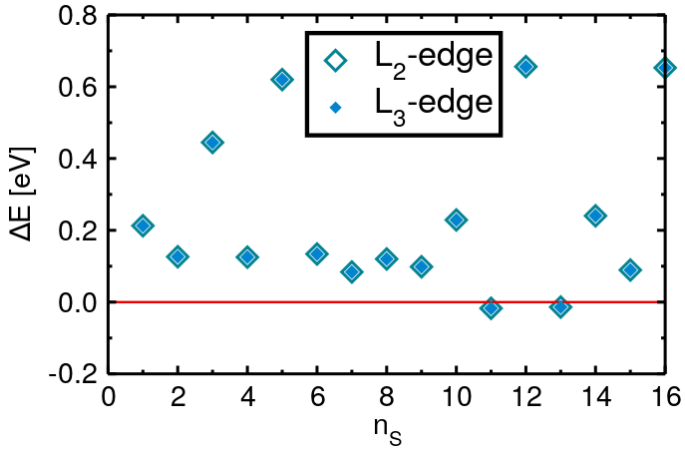

Figure 7.28.: Core-level shifts (ΔE) of the S $2p_{3/2}$ and $2p_{1/2}$ states for the inequivalent sulfur atoms, marked in Fig. 7.18 with respect to that of the single phase CZTS. The shifts are calculated by taking the VBM as reference.

considered simultaneously due to small (1.2 eV) spin-orbit splitting. The absorption spectra are calculated for the inequivalent sulfur atoms labeled in the supercell (Fig. 7.18). The core level shifts (ΔE) for the inequivalent sulfur atoms are shown in Fig. 7.28. Overall, the energetic position of the L_2 and L_3 edges are shifted by the same amount. As observed in K-edge (Fig. 7.21), most of the core states experience positive shifts. The atomic species S5, S12, and S16 are close to the acceptor point defect V_{Cu}. Their energetic positions are up-shifted by 0.66 eV. The energetic position of the atoms S11 and S13, which are around the donor point defect Zn_{Cu} are close to pristine CZTS. The energetic position of the atom S7, which is around Zn_{Cu} and close to V_{Cu} is up-shifted by 0.08 eV. The energetic position of atomic species S3, which is shared by both the point defects V_{Cu} and Zn_{Cu} is up-shifted by 0.47 eV. The energetic position for the first-neighboring atoms S1, S10, and S14 is up-shifted by 0.20 eV. The energetic position of the second-neighboring atoms S2, S4, S6, S8, S9, and S15 are $\sim$ 0.11 eV.

Like in K-edge, the absorption spectra are discussed for the atoms S3, S4, S5, S7, S11, and S16. The absorption spectra of the selected atoms in V_{Cu}+Zn_{Cu} and their average spectrum is shown in Fig. 7.29. The total spectrum obtained as the average over all contributions (cyan shaded area) is characterized by a peak at 149.8 eV, followed by a shoulder at 151.5 eV and another peak at 152.6 eV. These features can be understood by looking into the contribution of the individual S atoms to the total spectra. Similar to K-edge, the absorption onset of the inequivalent S atoms differs by 0.67 eV. The BSE spectra of S5 and S16 exhibits an onset peak at 149.8 eV. This concerns the up-shifted core levels of S atoms close to V_{Cu}. The onset peak from S11 is at 150.4 eV, and from S3 is at 150.07 eV. The core level of S4

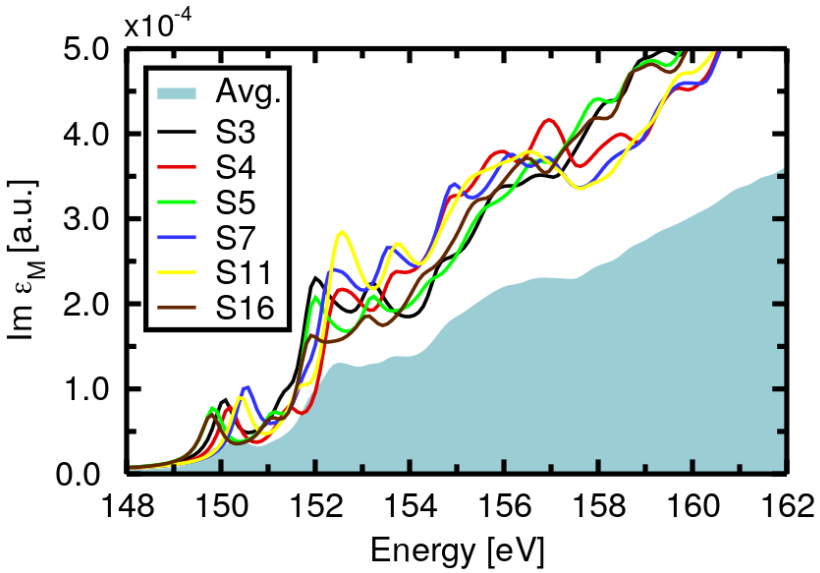

Figure 7.29.: Absorption spectra from the S $L_{2,3}$-edge of V_{Cu}+Zn_{Cu}. BSE results of the selected inequivalent S atoms as the average over the diagonal Cartesian components of the imaginary part of the macroscopic dielectric tensor. The cyan line denotes the average of all inequivalent S atoms.

and S7 is the same. However, they exhibit different onsets. The onset of S4 is at 150.18 eV reflects the ΔE whereas, the onset peak of S7 appears at higher energy. As discussed in K edge, the shifts in the absorption onset of the individual spectra can be understood by the interplay between core level shifts and exciton binding energies, which will be discussed in the following.

The excitonic nature of the spectral features can be examined by comparison with IPA spectra. The BSE (solid red lines) and IPA (solid black lines) spectra from the selected inequivalent S atoms are shown in Fig. 7.30. As observed in the previous cases, the inclusion of *e-h* interaction red-shifts the absorption onset and redistributes the spectral weights with respect to IPA. Excitonic effects enhance the peak intensities marked as A, B, C, and D. For all the S atoms, peak A is attributed to a bound exciton state. The corresponding binding energies are shown in Fig. 7.31 in comparison with single-phase CZTS (vertical gray line). As observed in K-edge, it can be observed that the excitations from the highest ΔE (S16) and the excitations from the lowest ΔE (S11) (see Fig. 7.21) exhibits binding energies close to that of single-phase CZTS. However, excitations from S4 and S7 have the same core-level shifts but exhibit different binding energies. Peak A from S4 is characterized by a high exciton binding energy of 0.50 eV, whereas S7 gives rise to weakly bound excitons with a binding energy of 0.20 eV. The high binding energy of S4 is attributed to the relatively large distance to

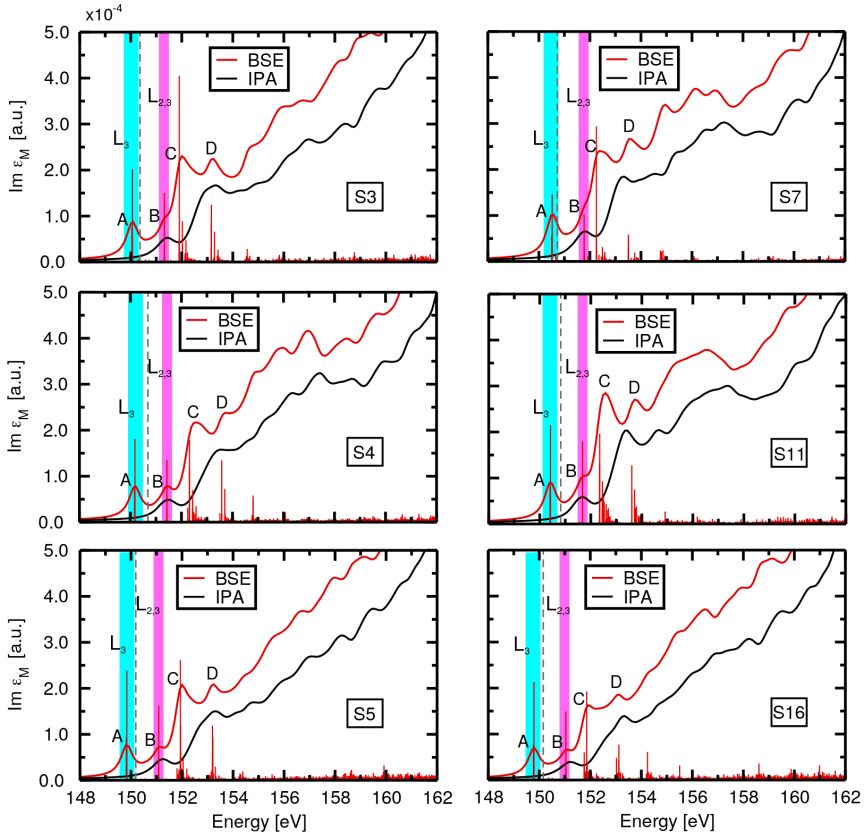

Figure 7.30.: Absorption spectra of S $L_{2,3}$-edge from the inequivalent S atoms of V_{Cu}+Zn_{Cu}. Solutions from the BSE and IPA are shown by solid red and black lines. The vertical line denotes the IPA onset. The oscillator strengths of the individual transitions are shown by the vertical bars, as obtained from the BSE calculations. The cyan vertical bars represent excitations from the L_3 edge, and the magenta vertical bar represent mixed transitions from the L_2 and L_3 channels.

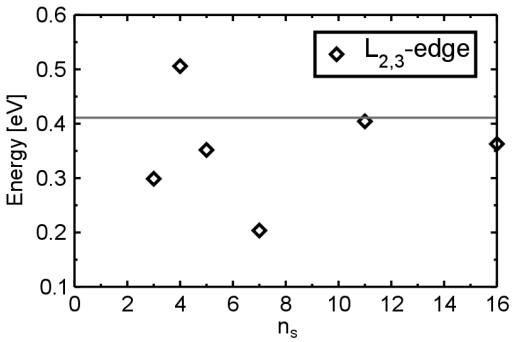

Figure 7.31.: Binding energy of the lowest-energy excitons of inequivalent S atoms in V_{Cu}+Zn_{Cu}. The horizontal gray line indicates the binding energy of the single-phase CZTS.

both the point defects whereas, the low binding energy of S7 is because S7 is around Zn_{Cu} and close to V_{Cu} (see Fig. 7.18). Thus, the onset of S4 is at

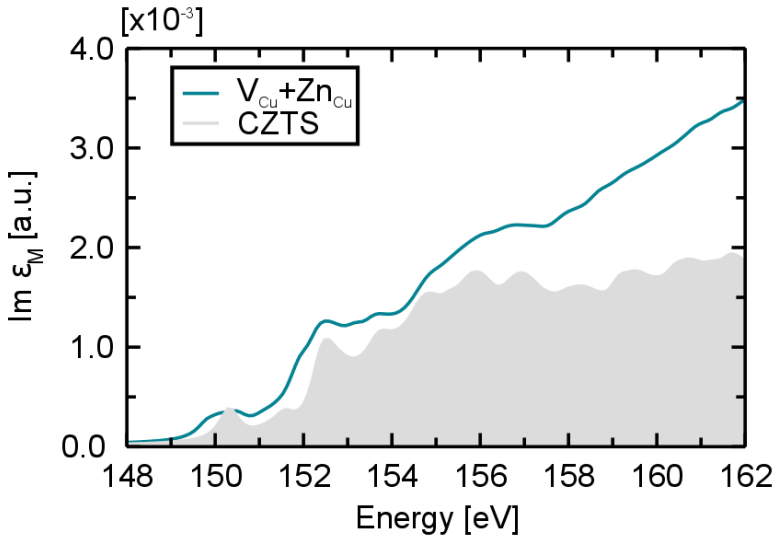

Figure 7.32.: The solid cyan line represents the total spectra of the inequivalent S atoms (see Fig. 7.22) in V_{Cu}+Zn_{Cu} in comparison the single-phase CZTS spectra (gray-shaded area). For more details on CZTS see Sec. 5.2.

lower energy, while the onset of S7 is at higher energy.

The height of the red vertical bars shows the oscillator strength of the excitons contributing to the corresponding peaks. The spectral features can be separated depending on the transitions originating either from L_2, L_3 absorption edges or by their mixing. Peak A in all the S atoms is formed by excitations from the $2p_{3/2}$ level (L_3 edge). Peak B is formed by mixed transitions from the L_2 and L_3 channels. Likewise, peak C originates from excitations again from $2p_{3/2}$ core-state, and peak D is from the mixed transitions. Above 156 eV, a continuum of excitations with low intensity characterizes the spectrum.

In Fig. 7.32 the total spectrum (solid cyan line) of V_{Cu}+Zn_{Cu} in comparison with the single-phase CZTS (gray shaded area) are shown. As observed in K edge (see Section 7.2.2), the absorption onset is red-shifted by 0.4 eV in comparison with CZTS. As mentioned previously, this can be explained by the complex interplay between the core level shift (Fig. 7.22) and exciton binding energies (7.24), and the local chemical environment. The excitations from the up-shifted core level (S16) and the down-shifted core level (S11) exhibits binding energies of ∼0.4 eV. In this case, the exciton binding energy and core level positions do not go hand in hand, as already mentioned. For example, S4 and S7 have the same core level position and exhibit different binding energies of 0.51 and 0.20 eV, respectively. This difference is because of the relatively large distance of S4 to both the point defects in comparison

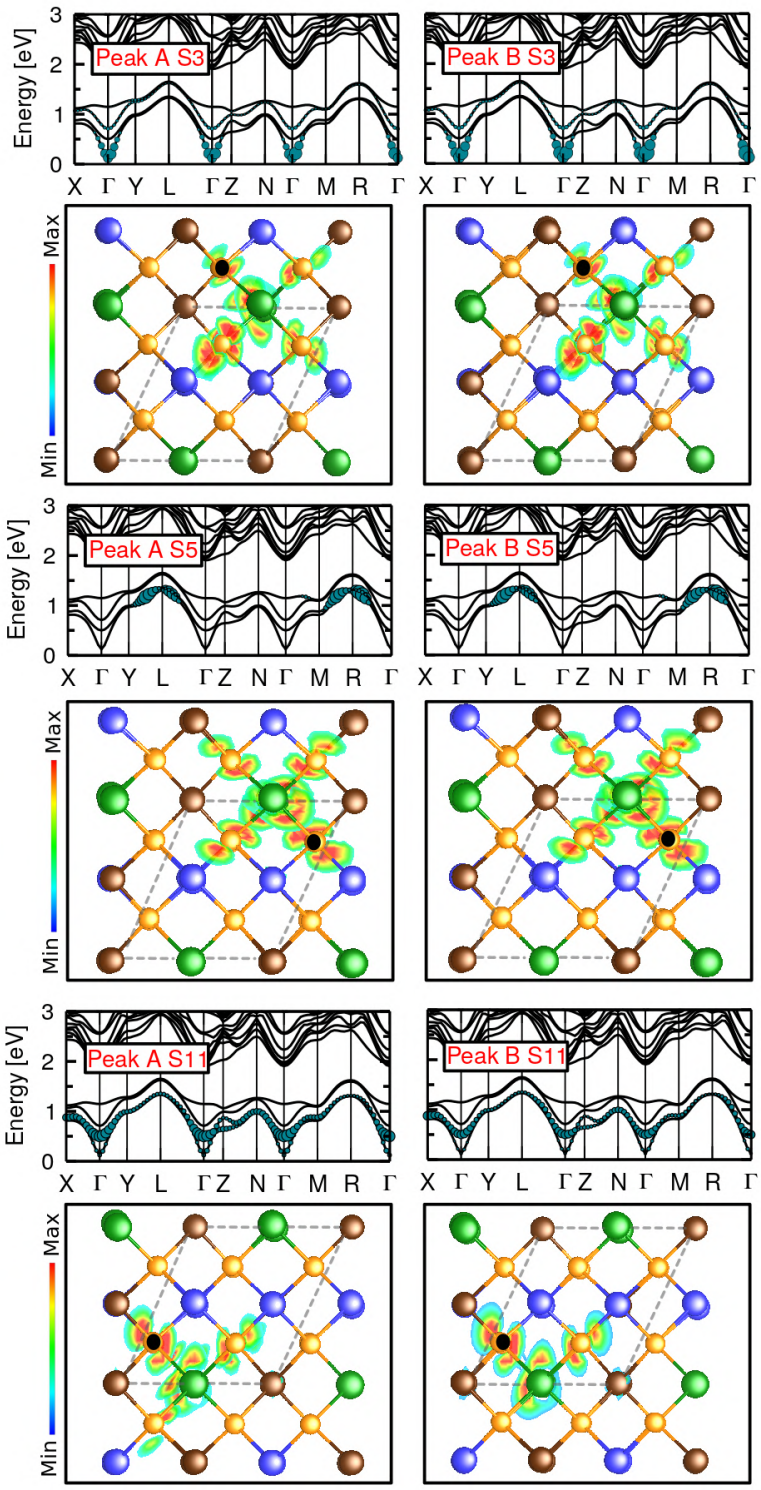

Figure 7.33.: Contributions of individual bands to the excitations of peaks A and B in S3, S11, and S5 marked in Fig. 7.30. The size of the cyan-colored circles quantifies the weight of the respective electronic state in the excitonic eigenstate. Their respective bottom-panel shows the real-space representation of the electron distribution. In all cases, the fixed hole position is marked by a black circle. Cu atoms are displayed in brown, Zn atoms in blue, Sn atoms in green, S atoms in orange.

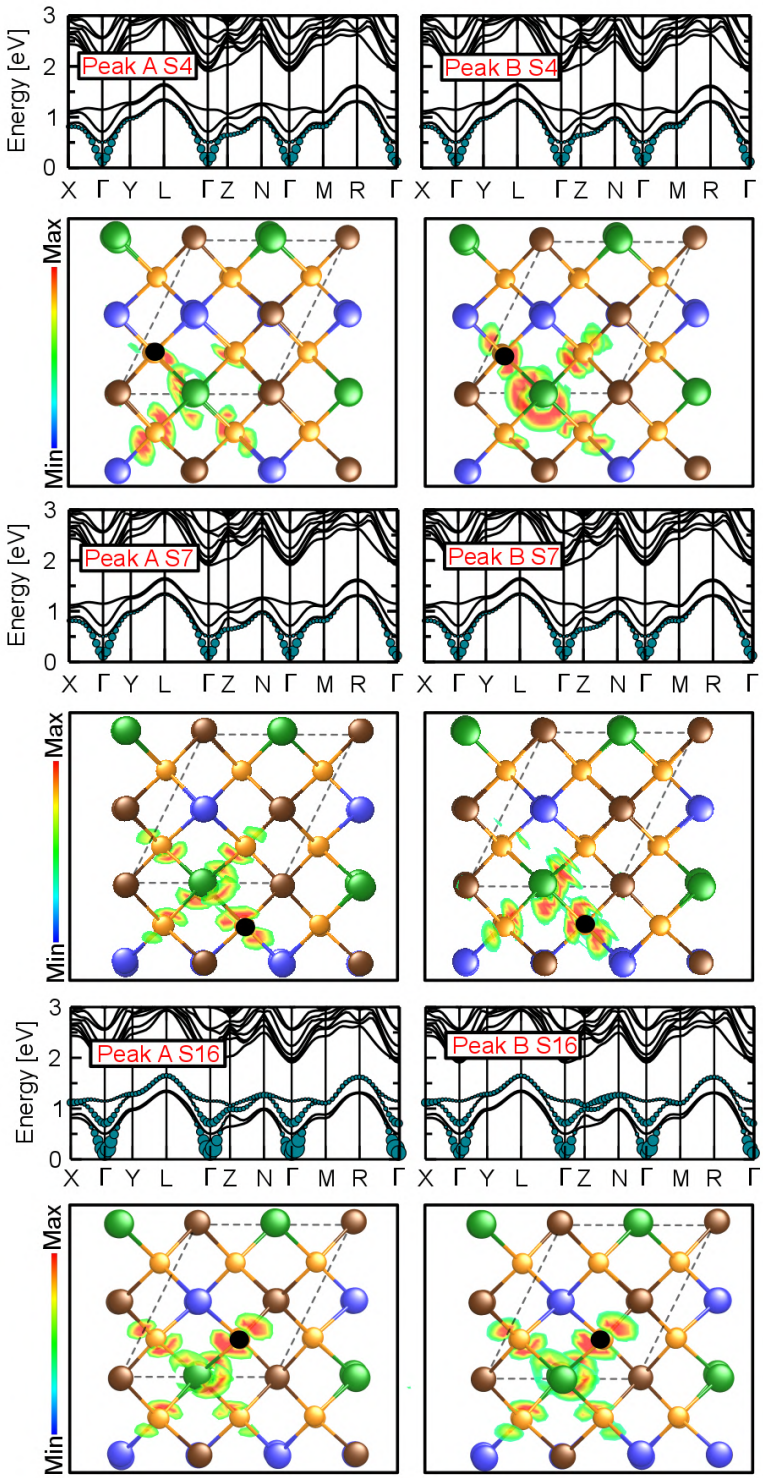

Figure 7.34.: Contributions of individual bands to the excitations of peaks A and b in S4, S7, and S16 marked in Fig. 7.30. The size of the cyan-colored circles quantifies the weight of the respective electronic state in the excitonic eigenstate. Their respective bottom-panel shows the real-space representation of the electron distribution. In all cases, the fixed hole position is marked by a black circle. Cu atoms are displayed in brown, Zn atoms in blue, Sn atoms in green, S atoms in orange.

with S7. Consequently, S16 determines the onset of the total spectra that is comparable with single-phase CZTS. At higher energies, the difference in the spectral features becomes smaller as the excitonic effects do not play a major role in this energy region.

To analyze the excitonic character of peaks A and B for the S atoms marked in Fig. 7.30, the band contributions to these excitons are shown by projecting the excitonic weights onto the KS bandstructure in Figs.7.33 and 7.34. Peaks A and B (Fig. 7.33) stem from transitions to the conduction bands up to 1.4 eV. The exciton weights are distributed over the entire BZ. The dominant contributions for peak A and B in S3, S4, S7, S11, and S16 is at Γ-point, whereas the major contribution in S5 is from the path L-R. To complement this analysis, in Figs. 7.33 and 7.34 also displays the distribution of the *e-h* wavefunction in real-space. The exciton wavefunctions corresponding to peaks A and B (Fig. 7.33) are similar. The exciton wavefunctions are not fully localized at the excited S atom but extend to the neighboring Sn and S atom but extend to the first neighboring Sn atom and the surrounding S atoms.

7.3. Comparison of single-phase CZTS and their defect complexes with Experiment

In this section, the differences between the calculated and measured spectra addressed in Chapter 5 are discussed. The core-level absorption spectra of the sulfur K- and $L_{2,3}$-edge of single-phase CZTS (gray shaded area) and their defect complexes together with the measured spectra of the different samples are shown in Fig. 7.35. The displayed BSE spectra of the defect complexes Cu_{Zn}+Zn_{Cu} (solid magenta line), and V_{Cu}+Zn_{Cu} (solid cyan line) is the average of the inequivalent S atoms in their respective system discussed in Section. 7.2.2 to 7.2.3. The solid blue line represents the average of V_{Cu}+Zn_{Cu} and Cu_{Zn}+Zn_{Cu} spectra. For comparison with the experiment, the calculated BSE of all the three cases are shifted by the same amount. The calculated spectra are shifted by 70.8 and 12.79 eV for K and $L_{2,3}$-edge.

First, it is important to understand the comparison between the calculated spectra of pristine CZTS and defect complexes. In case of K edge (left panel), the absorption onset of V_{Cu}+Zn_{Cu} is shifted to lower energy by 0.4 eV in comparison with single-phase CZTS, while Cu_{Zn}+Zn_{Cu} and CZTS are similar at the onset. Between 2472.0 and 2477.5 eV, the spectral features are also shifted with respect to each other, wherewith increasing energy, the

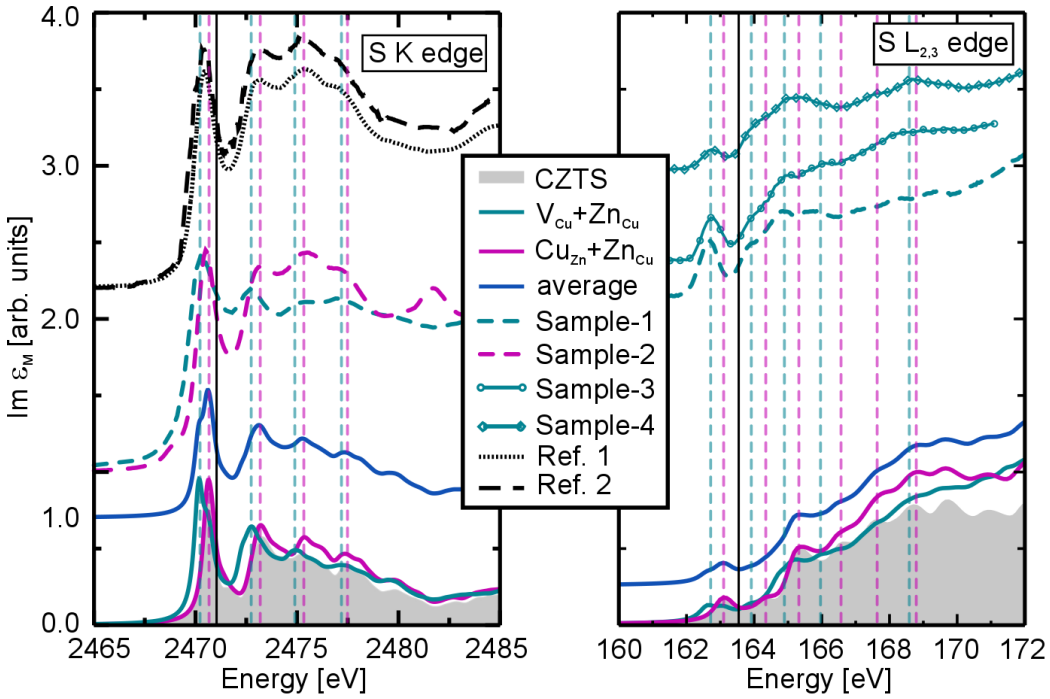

Figure 7.35.: Near-edge X-ray absorption spectra of the sulfur K (left panel) and $L_{2,3}$ edges (right panel) in CZTS. The gray shaded areas corresponds to the theoretical results computed by the Bethe-Salpeter equation for the defect-free CZTS crystal. The colored solid lines represent BSE results obtained by considering two defect complexes, V_{Cu}+Zn_{Cu} (magenta) and Cu_{Zn}+Zn_{Cu} (cyan). The solid blue line represents the average of V_{Cu}+Zn_{Cu} and Cu_{Zn}+Zn_{Cu} spectra. The black vertical line indicates the IPA onset of defect-free CZTS, the colored vertical lines highlight the positions of the main peaks. For comparison, the dashed lines show experimental results of 4 different samples. Only for Sample 1 [57], experiments have been performed for both edges. The spectra for Sample 2 are taken from Ref. [58]. The spectra Ref.1 is taken from Ref. [63] and Ref.2 [64].

peak positions differ less. Overall, the intensity for Cu_{Zn}+Zn_{Cu} is higher than for V_{Cu}+Zn_{Zn} and pristine CZTS. As mentioned in Sections 7.1.2 and 7.2.2, these differences can be attributed to the complex interplay between bandgap, core-level energies, and exciton binding energies. Above 2477.5 eV, the intensity of the defected structures stays higher compared to the perfect material while the features become more similar. For the interpretation of measured spectra, the average spectrum (solid blue line) of both the defect complexes is shown in Fig. 7.35. The average spectrum is characterized by a hump-like feature at 2470.20 eV and a peak at 2470.63eV, followed by three distinct peaks at 2473.20, 2475.28, and 2477.42 eV. Overall, the spectral features appear to be relatively broad at the onset in comparison with both the defective structures. From 2473.20 eV the spectral features resembles Cu_{Zn}+Zn_{Cu}.

In comparison with the measured spectra, the absorption onset of sample-1

is at 2470.2 eV and for sample-2 is at 2470.5 eV. The intensity of peaks at higher energies between 2472 and 2477.5 eV is more enhanced in sample 2. These differences match the differences observed in the calculated spectra. The spectral features of sample-1 is the agreement with the calculated V_{Cu}+Zn_{Cu} spectra, and sample-2 agree with the calculated Cu_{Zn}+Zn_{Cu} spectra. The other measured spectra (dotted and dashed black lines) from Ref. [63, 64] matches with sample-2 and are in agreement with the calculated Cu_{Zn}+Zn_{Cu} spectra.

To further testify, a similar analysis has been carried out on the S $L_{2,3}$ edge for all three cases. As mentioned before, K and $L_{2,3}$ edge are different as they probe different final states due to selection rules. In the case of K edge, the final states are *p*-like whereas in L edge the final states are *s*- and *d*-like. The results from the S $L_{2,3}$ edge are shown in the right panel of Fig. 7.35. The calculated spectra of the single-phase CZTS and defect complexes show similar differences, as observed in the K edge. Similarly, the spectral features of the average spectra appear to be relatively broad at the onset in comparison with both the defective structures. From 165.5 eV, the spectral features resemble Cu_{Zn}+Zn_{Cu}. For the consistent assessment of the calculations from both the edges, experiments were carried out to obtain S $L_{2,3}$ edge spectra on sample-1. In comparison with the calculated spectra, sample-1 shows an excellent agreement V_{Cu}+Zn_{Cu} calculated spectra, similar to K-edge confirming the spectral fingerprints go hand-in-hand with the sample quality. Here, all samples (1, 3, and 4) exhibit identical features, all in line with the computed V_{Cu}+Zn_{Cu} spectra. Despite the good agreement, Sample-1 needs further investigation as samples prepared using the same composition exhibits contaminants dominated by secondary phases related to Sn-S.

7.4. Summary

In this chapter, a detailed analysis of the electronic structure and excitations from the S K- and $L_{2,3}$-edge in the defect complexes Cu_{Zn}+Zn_{Cu} and V_{Cu}+Zn_{Cu} in CZTS has been presented in comparison with the single-phase CZTS. With the defect complex Cu_{Zn}+Zn_{Cu} the bandgap is decreased by 0.09 eV whereas with V_{Cu}+Zn_{Zn} the bandgap is increased by 0.10 eV. The absorption spectra are calculated for the selected sulfur atoms for both K and $L_{2,3}$ edges as the lower symmetry of both systems makes the sulfur atomic sites inequivalent. In both K and $L_{2,3}$ edges, the absorption onset of the total spectra from V_{Cu}+Zn_{Cu} is shifted to lower energy by 0.4 eV, whereas the onset of Cu_{Zn}+Zn_{Cu} similar to CZTS in both the edges. This

is attributed to the interplay between the bandgap, core level shift, and binding energy. Above 2 eV from onset the spectral features of Cu_{Zn}+Zn_{Cu} exhibits high intensity than V_{Cu}+Zn_{Cu} and pristine CZTS. The differences that are discussed in Chapter. 5 between the calculated and measured spectra have been addressed in comparison with the defect complex V_{Cu}+Zn_{Cu} and Cu_{Zn}+Zn_{Cu}. The comparison between calculated and measured spectra provides insight to distinguish between the different nature of defect complexes that are present in the experiment probes.

Appendices

This appendix supplements Chapter. 5 and 6 where the absorption spectra of K- and $L_{2,3}$ edge in CZTS and the binary phases SnS_2 and ZnS are discussed. Due to computational cost the convergence test was performed using 8-atom unit cell. The BSE spectra for 32 atom supercell was obtained by utilizing the available computational resources and compared with the converged spectra obtained with 8 atom unit cell. This is depicted in Fig. A.1. The convergence of the binary phases SnS_2 and ZnS are shown in Fig. A.2-A.3.

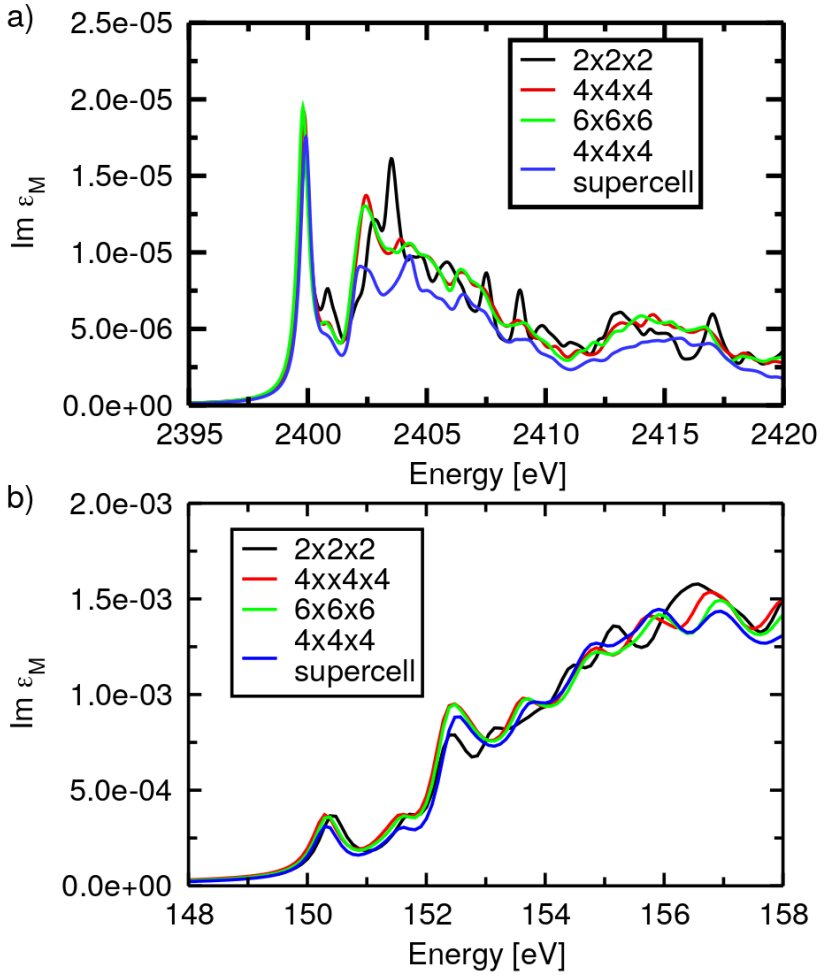

Figure A.1.: Convergence of the sulfur a) K-edge and b) $L_{2,3}$-edge spectra for Cu_2ZnSnS_4. The *xx* component of the dielectric tensor is shown.

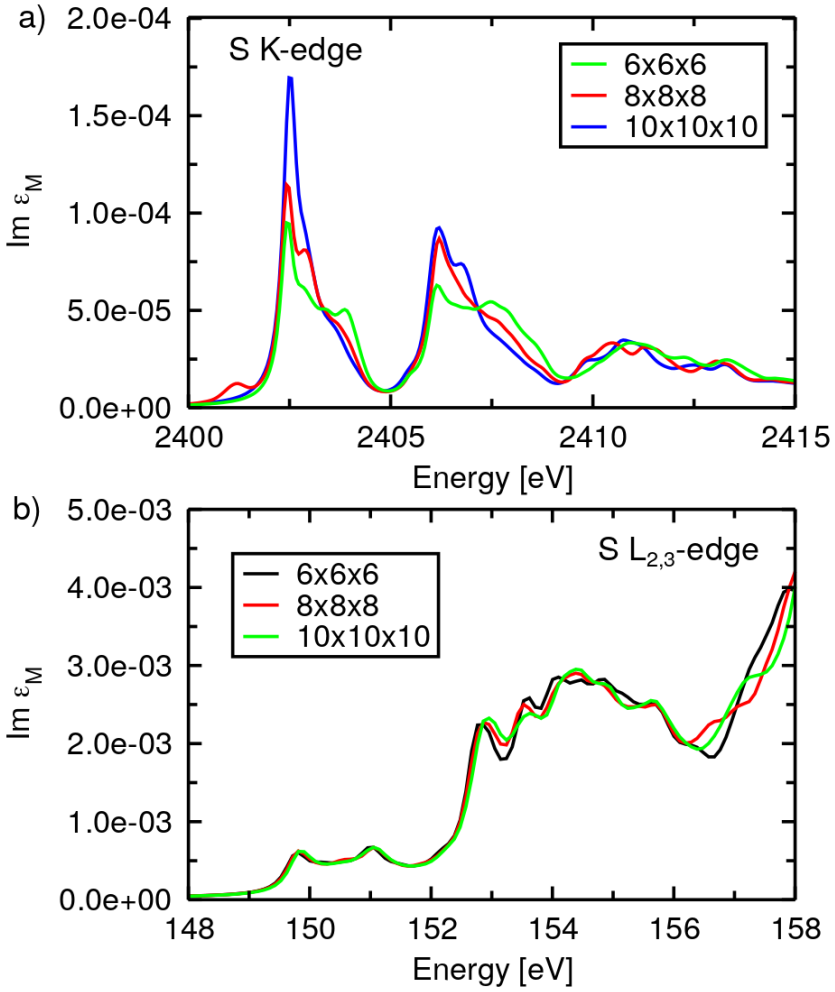

Figure A.2.: Convergence of the sulfur a) K-edge and b) $L_{2,3}$-edge spectra for SnS_2. The *xx* component of the dielectric tensor is shown.

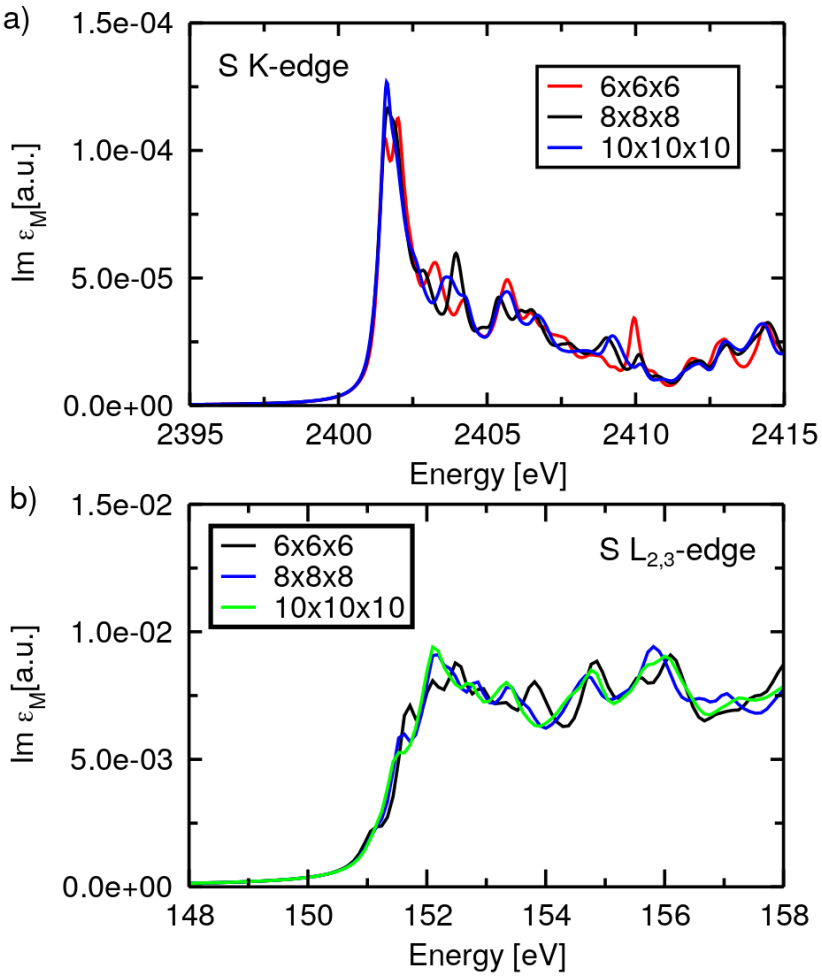

Figure A.3.: Convergence of the sulfur a) K-edge and b) $L_{2,3}$-edge spectra for ZnS. The *xx* component of the dielectric tensor is shown.

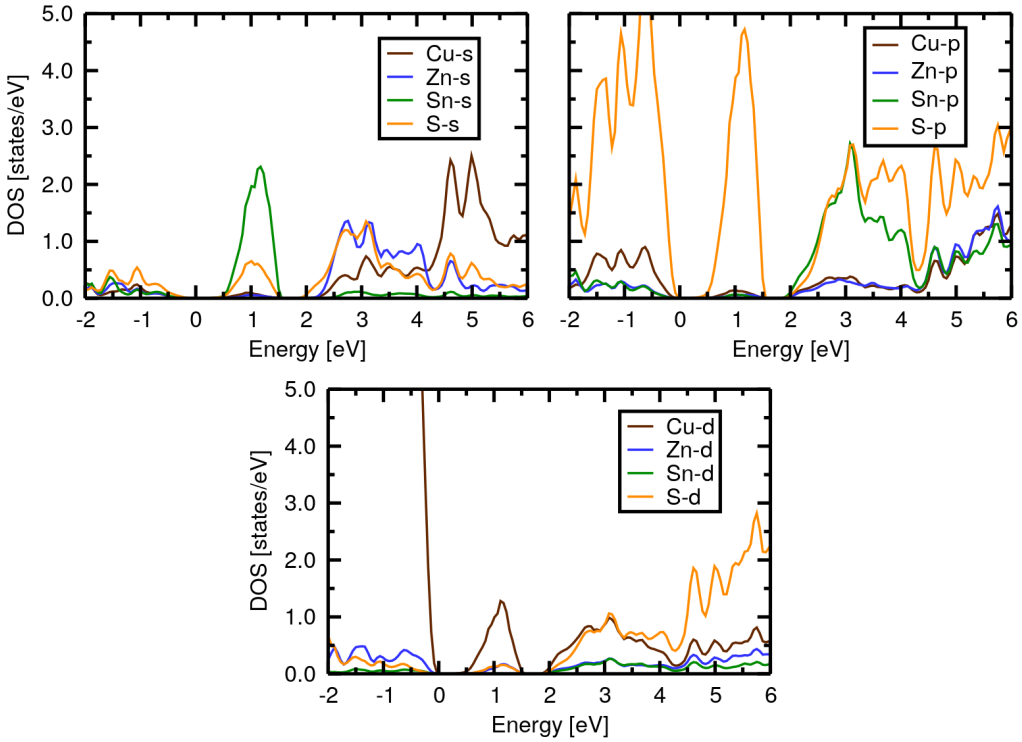

Figure A.4.: Projected density of states for copper, zinc, tin and sulfur atoms in Cu_2ZnSnS_4.

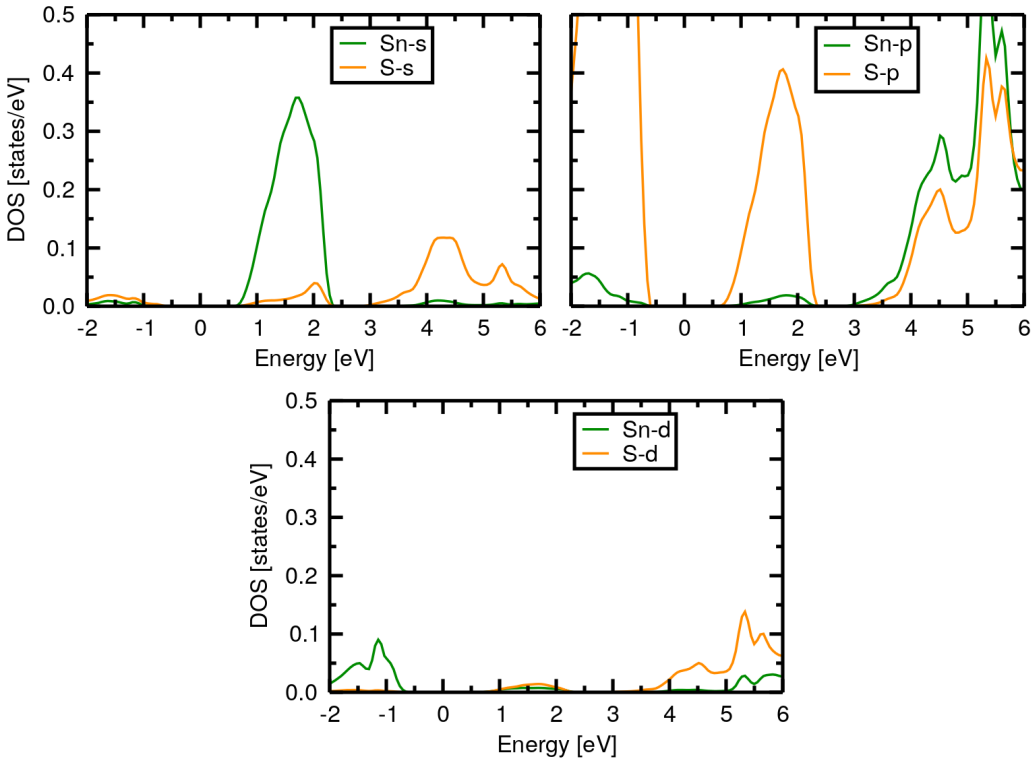

Figure A.5.: Projected density of states for tin and sulfur atoms in SnS_2.

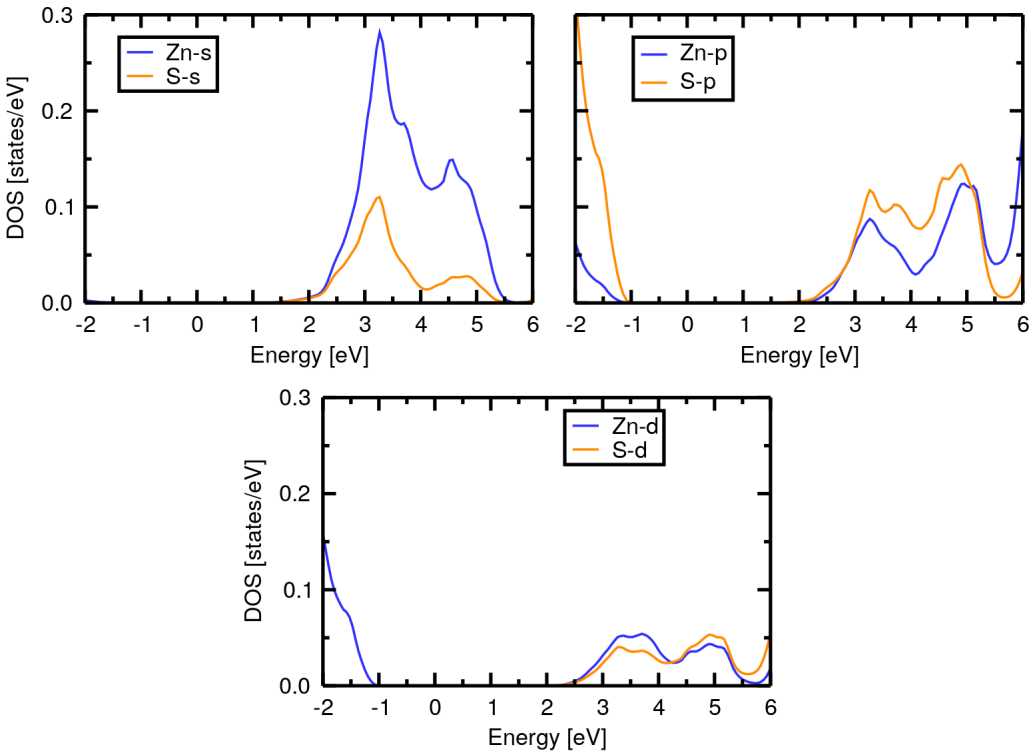

Figure A.6.: Projected density of states for zinc and sulfur atoms in ZnS.

Acronyms

e-h	elecron-hole
APW	agumented planewave
BSE	Bethe-Salpeter equation
BZ	Brilloiun zone
CBM	conduction band minimum
CIGS	$CuIn_xGa_{(1-x)}Se_2$
CZTS	Cu_2ZnSnS_4
CZTSe	$Cu_2ZnSnSe_4$
CZTSSe	$Cu_2ZnSn(S_xSe_{1-x})_4$
DFT	density-functional theory
DOS	density of states
EXAFS	extended x-ray absorption fine structure
GGA	generalized gradient approximation
IPA	independant particle approximation
KS	Kohn-Sham
LAPW	linearized augmented planewaves
LDA	local-density approximation
MBPT	Many-body pertubation theory
PDOS	partial density of states
RPA	random-phase approximation
TDA	Tamm-Dancoff approximation
VBM	valence band maximum
XAFS	X-ray absorption fine structure
XANES	X-ray absorption near edge structure

ZORA zero-order regular approximation

[1] L. C. Andreani, A. Bozzola, P. Kowalczewski, M. Liscidini, and L. Redorici, "Silicon solar cells: toward the efficiency limits," *Advances in Physics: X*, vol. 4, no. 1, p. 1548305, 2019.

[2] M. A. Green, Y. Hishikawa, E. D. Dunlop, D. H. Levi, J. Hohl-Ebinger, M. Yoshita, and A. W. Y. Ho-Baillie, "Solar cell efficiency tables (Version 53)," *Progress in Photovoltaics: Research and Applications*, vol. 27, no. 1, pp. 3–12, 2019.

[3] F. Zhang and K. Zhu, "Additive engineering for efficient and stable perovskite solar cells," *Advanced Energy Materials*, vol. 10, no. 13, p. 1902579, 2020.

[4] R. Wang, M. Mujahid, Y. Duan, Z.-K. Wang, J. Xue, and Y. Yang, "A review of perovskites solar cell stability," *Advanced Functional Materials*, vol. 29, no. 47, p. 1808843, 2019.

[5] S. Ahmed, K. B. Reuter, O. Gunawan, L. Guo, L. T. Romankiw, and H. Deligianni, "A High Efficiency Electrodeposited Cu2ZnSnS4 Solar Cell," *Advanced Energy Materials*, vol. 2, no. 2, pp. 253–259, 2012.

[6] S. Siebentritt and S. Schorr, "Kesterites—a challenging material for solar cells," *Progress in Photovoltaics: Research and Applications*, vol. 20, no. 5, pp. 512–519, 2012.

[7] D. B. Mitzi, O. Gunawan, T. K. Todorov, K. Wang, and S. Guha, "The path towards a high-performance solution-processed kesterite solar cell," *Solar Energy Materials and Solar Cells*, vol. 95, no. 6, pp. 1421–1436, 2011.

[8] C. Yan, K. Sun, J. Huang, S. Johnston, F. Liu, B. P. Veettil, K. Sun, A. Pu, F. Zhou, J. A. Stride, M. A. Green, and X. Hao, "Beyond 11% Efficient Sulfide Kesterite Cu2ZnxCd1–xSnS4 Solar Cell: Effects of Cadmium Alloying," *ACS Energy Letters*, vol. 2, no. 4, pp. 930–936, 2017.

[9] G. Onida, L. Reining, and A. Rubio, "Electronic excitations: density-functional versus many-body Green's-function approaches," *Rev. Mod. Phys.*, vol. 74, pp. 601–659, jun 2002.

[10] L. Hedin, "New Method for Calculating the One-Particle Green's Func-

tion with Application to the Electron-Gas Problem," *Phys. Rev.*, vol. 139, pp. A796—-A823, aug 1965.

[11] W. Hanke and L. J. Sham, "Many-particle effects in the optical spectrum of a semiconductor," *Phys. Rev. B*, vol. 21, pp. 4656–4673, may 1980.

[12] G. Strinati, "Application of the Green's functions method to the study of the optical properties of semiconductors," *Nuovo Cimento Rivista Serie*, vol. 11, pp. 1–86, dec 1988.

[13] W. Olovsson, I. Tanaka, T. Mizoguchi, P. Puschnig, and C. Ambrosch-Draxl, "All-electron Bethe-Salpeter calculations for shallow-core x-ray absorption near-edge structures," *Phys. Rev. B*, vol. 79, p. 41102, jan 2009.

[14] R. Laskowski and P. Blaha, "Understanding the ${L}_{2,3}$ x-ray absorption spectra of early $3d$ transition elements," *Phys. Rev. B*, vol. 82, p. 205104, nov 2010.

[15] J. Vinson and J. J. Rehr, "Ab initio Bethe-Salpeter calculations of the x-ray absorption spectra of transition metals at the L-shell edges," *Phys. Rev. B*, vol. 86, p. 195135, nov 2012.

[16] J. Vinson, J. J. Rehr, J. J. Kas, and E. L. Shirley, "Bethe-Salpeter equation calculations of core excitation spectra," *Phys. Rev. B*, vol. 83, p. 115106, mar 2011.

[17] W. Olovsson, I. Tanaka, T. Mizoguchi, G. Radtke, P. Puschnig, and C. Ambrosch-Draxl, "Al ${L}_{2,3}$ edge x-ray absorption spectra in III-V semiconductors: Many-body perturbation theory in comparison with experiment," *Phys. Rev. B*, vol. 83, p. 195206, may 2011.

[18] C. Vorwerk, C. Cocchi, and C. Draxl, "Addressing electron-hole correlation in core excitations of solids: An all-electron many-body approach from first principles," *Phys. Rev. B*, vol. 95, p. 155121, apr 2017.

[19] A. Gulans, S. Kontur, C. Meisenbichler, D. Nabok, P. Pavone, S. Rigamonti, S. Sagmeister, U. Werner, and C. Draxl, "exciting: a full-potential all-electron package implementing density-functional theory and many-body perturbation theory," *Journal of Physics: Condensed Matter*, vol. 26, no. 36, p. 363202, 2014.

[20] H. C. Vorwerk, "All-Electron Many-Body Approach to X-Ray Absorption Spectroscopy," no. April, 2016.

[21] R. Nitsche, D. F. Sargent, and P. Wild, "Crystal growth of quaternary 122464 chalcogenides by iodine vapor transport," *Journal of Crystal Growth*, vol. 1, no. 1, pp. 52–53, 1967.

[22] K. Ito and T. Nakazawa, "Electrical and Optical Properties of Stannite-Type Quaternary Semiconductor Thin Films," *Japanese Journal of Applied Physics*, vol. 27, pp. 2094–2097, nov 1988.

[23] H. Katagiri, K. Jimbo, W. S. Maw, K. Oishi, M. Yamazaki, H. Araki, and A. Takeuchi, "Development of CZTS-based thin film solar cells," *Thin Solid Films*, vol. 517, no. 7, pp. 2455–2460, 2009.

[24] C. Yan, J. Huang, K. Sun, S. Johnston, Y. Zhang, H. Sun, A. Pu, M. He, F. Liu, K. Eder, L. Yang, J. M. Cairney, N. J. Ekins-Daukes, Z. Hameiri, J. A. Stride, S. Chen, M. A. Green, and X. Hao, "Cu2ZnSnS4 solar cells with over 10% power conversion efficiency enabled by heterojunction heat treatment," *Nature Energy*, vol. 3, no. 9, pp. 764–772, 2018.

[25] T. K. Todorov, K. B. Reuter, and D. B. Mitzi, "High-Efficiency Solar Cell with Earth-Abundant Liquid-Processed Absorber," *Advanced Materials*, vol. 22, no. 20, pp. E156—-E159, 2010.

[26] W. Wang, M. T. Winkler, O. Gunawan, T. Gokmen, T. K. Todorov, Y. Zhu, and D. B. Mitzi, "Device characteristics of cztsse thin-film solar cells with 12.6% efficiency," *Advanced Energy Materials*, vol. 4, no. 7, p. 1301465, 2014.

[27] S. Schorr, H.-J. Hoebler, and M. Tovar, "A neutron diffraction study of the stannite-kesterite solid solution series," *European Journal of Mineralogy*, vol. 19, no. 1, pp. 65–73, 2007.

[28] Delbos, S., "Këwhile thin films for photovoltaics : a review," *EPJ Photovolt.*, vol. 3, p. 35004, 2012.

[29] W. Shockley and H. J. Queisser, "Detailed balance limit of efficiency of p-n junction solar cells," *Journal of Applied Physics*, vol. 32, no. 3, pp. 510–519, 1961.

[30] M. A. Green, E. D. Dunlop, J. Hohl-Ebinger, M. Yoshita, N. Kopidakis, and A. W. Ho-Baillie, "Solar cell efficiency tables (version 55)," *Progress in Photovoltaics: Research and Applications*, vol. 28, no. 1, pp. 3–15, 2020.

[31] S. Chen, J.-H. Yang, X. G. Gong, A. Walsh, and S.-H. Wei, "Intrinsic

point defects and complexes in the quaternary kesterite semiconductor Cu$ _2$ZnSnS$ _4$," *Phys. Rev. B*, vol. 81, p. 245204, jun 2010.

[32] I. D. Olekseyuk, I. V. Dudchak, and L. V. Piskach, "Phase equilibria in the Cu2S–ZnS–SnS2 system," *Journal of Alloys and Compounds*, vol. 368, no. 1, pp. 135–143, 2004.

[33] S. Chen, X. G. Gong, A. Walsh, and S.-H. Wei, "Crystal and electronic band structure of Cu2ZnSnX4 (X=S and Se) photovoltaic absorbers: First-principles insights," *Applied Physics Letters*, vol. 94, no. 4, p. 41903, 2009.

[34] J. J. S. Scragg, J. K. Larsen, M. Kumar, C. Persson, J. Sendler, S. Siebentritt, and C. Platzer Björkman, "Cu-zn disorder and band gap fluctuations in $cu_2znsn(s,se)_4$: Theoretical and experimental investigations," *physica status solidi (b)*, vol. 253, no. 2, pp. 247–254, 2016.

[35] J. J. Rehr and R. C. Albers, "Theoretical approaches to x-ray absorption fine structure," *Rev. Mod. Phys.*, vol. 72, pp. 621–654, Jul 2000.

[36] E. K. G. Reiner M. Dreizler, "Density functional theory," p. 304, 04 1990.

[37] K. Burke, "The abc of dft," p. 92697, 04 2007.

[38] P. Hohenberg and W. Kohn, "Inhomogeneous electron gas," *Phys. Rev.*, vol. 136, pp. B864–B871, Nov 1964.

[39] J. P. Perdew, K. Schmidt, V. Van Doren, C. Van Alsenoy, and P. Geerlings, "Jacobś ladder of density functional approximations for the exchange-correlation energy," *AIP Conference Proceedings*, vol. 577, no. 1, pp. 1–20, 2001.

[40] D. Fritsch and S. Schorr, "Climbing jacob's ladder: A density functional theory case study for ag2znsnse4 and cu2znsnse4," 2020.

[41] J. P. Perdew and Y. Wang, "Accurate and simple analytic representation of the electron-gas correlation energy," *Phys. Rev. B*, vol. 45, pp. 13244–13249, Jun 1992.

[42] J. P. Perdew, K. Burke, and M. Ernzerhof, "Generalized gradient approximation made simple," *Phys. Rev. Lett.*, vol. 77, pp. 3865–3868, Oct 1996.

[43] O. K. Andersen, "Linear methods in band theory," *Phys. Rev. B*, vol. 12, pp. 3060–3083, Oct 1975.

[44] G. Onida, L. Reining, and A. Rubio, "Electronic excitations: density-functional versus many-body green's-function approaches," *Rev. Mod. Phys.*, vol. 74, pp. 601–659, Jun 2002.

[45] S. Sagmeister and C. Ambrosch-Draxl, "Time-dependent density functional theory versus bethae salpeter equation: an all-electron study," *Phys. Chem. Chem. Phys.*, vol. 11, pp. 4451–4457, 2009.

[46] M. Rohlfing and S. G. Louie, "Electron-hole excitations and optical spectra from first principles," *Phys. Rev. B*, vol. 62, pp. 4927–4944, Aug 2000.

[47] P. Puschnig, *Excitonic Effects in Organic Semi-Conductors - An Ab-initio Study within the LAPW Method*. PhD thesis, 01 2002.

[48] P. Puschnig, C. Meisenbichler, and C. Draxl, "Excited state properties of organic semiconductors: Breakdown of the tamm-dancoff approximation," 06 2013.

[49] G. Kresse and J. Hafner, "Ab initio molecular dynamics for liquid metals," *Phys. Rev. B*, vol. 47, pp. 558–561, Jan 1993.

[50] J. Paier, R. Asahi, A. Nagoya, and G. Kresse, "cu_2znsns_4 as a potential photovoltaic material: A hybrid hartree-fock density functional theory study," *Phys. Rev. B*, vol. 79, p. 115126, Mar 2009.

[51] G. Gurieva, M. Dimitrievska, S. Zander, A. Pérez-Rodríguez, V. Izquierdo-Roca, and S. Schorr, "Structural characterisation of Cu2.04Zn0.91Sn1.05S2.08Se1.92," *physica status solidi c*, vol. 12, no. 6, pp. 588–591, 2015.

[52] L. E. V. Rios, K. Neldner, G. Gurieva, and S. Schorr, "Existence of off-stoichiometric single phase kesterite," *Journal of Alloys and Compounds*, vol. 657, pp. 408–413, 2016.

[53] S. R. Hall, J. T. Szymanski, and J. M. Stewart, "Kesterite, Cu_2 (Zn,Fe)SnS_4 , and stannite, Cu_2 (Fe,Zn)SnS_4 , structurally similar but distinct minerals," *The Canadian Mineralogist*, vol. 16, no. 2, pp. 131–137, 1978.

[54] J. Paier, R. Asahi, A. Nagoya, and G. Kresse, "cu_2znsns_4 as a potential

photovoltaic material: A hybrid hartree-fock density functional theory study," *Phys. Rev. B*, vol. 79, p. 115126, Mar 2009.

[55] C. Persson, "Electronic and optical properties of Cu2ZnSnS4 and Cu2ZnSnSe4," *Journal of Applied Physics*, vol. 107, no. 5, p. 53710, 2010.

[56] S. Botti, D. Kammerlander, and M. A. L. Marques, "Band structures of cu2znsns4 and cu2znsnse4 from many-body methods," *Applied Physics Letters*, vol. 98, no. 24, p. 241915, 2011.

[57] "Sample-1: Experimental data from prof. andrivo rusydi, national university of singapore."

[58] J. Just, D. Lützenkirchen-Hecht, R. Frahm, S. Schorr, and T. Unold, "Determination of secondary phases in kesterite cu2znsns4 thin films by x-ray absorption near edge structure analysis," *Applied Physics Letters*, vol. 99, no. 26, p. 262105, 2011.

[59] "Sample-3: Experimental data from prof. marcus bär, helmholtz-zentrum berlin."

[60] Y. Javed, M. A. Rafiq, and N. Ahmed, "Pressure-induced changes in the electronic structure and enhancement of the thermoelectric performance of sns2: a first principles study," *RSC Adv.*, vol. 7, pp. 38834–38843, 2017.

[61] L. Sun, W. Zhou, Y. Liu, D. Yu, Y. Liang, and P. Wu, "Electronic structure and optical properties of fe-doped sns2 from first-principle calculations," *RSC Adv.*, vol. 6, pp. 3480–3486, 2016.

[62] J. E. Bernard and A. Zunger, "Electronic structure of zns, znse, znte, and their pseudobinary alloys," *Phys. Rev. B*, vol. 36, pp. 3199–3228, Aug 1987.

[63] A. Ritscher, *Synthesis and structural characterization of semiconductors based on kesterites*. Doctoral thesis, Technische Universität Berlin, Berlin, 2016.

[64] S. C. Siah, R. Jaramillo, R. Chakraborty, P. T. Erslev, C.-J. Sun, T.-C. Weng, M. F. Toney, G. Teeter, and T. Buonassisi, "X-ray absorption spectroscopy study of structure and stability of disordered (cu $_2$sns$_3$) $_{1-x}$(zns)$_x$ alloys," *IEEE Journal of Photovoltaics*, vol. 5, no. 1, pp. 372–377, 2015.

Acknowledgements

First and foremost, I would like to express my sincere gratitude to my supervisor Prof. Dr. Claudia Draxl for her help and support during my thesis. This thesis would not have been possible without the opportunities that she provided for me over the years. She allowed me to follow my research ideas and gave me enough freedom, while she steadily guided my independent work when necessary.

I am grateful to Prof. Dr. Clas Persson for his help to understand the defect complexes. Our discussion about defects in kesterites helped me to efficiently address the difference between the theory and experiment. I especially want to thank his group members for their hospitality during my visits to the University of Oslo.

I want to thank all the group members of the solid-state theory group at the Humboldt Universität Zu Berlin and all scientists that I had the honor to work with in the last years. I want to thank my roommates Maria Troppenz for our numerous coffee breaks.

I thank Saeideh Edalati-Boostan and Wahib Aggoune for their support during the Corona pandemic. Last but not least, I thank my family for their unconditional support and understanding during the last years.